Simão Bolota de Couto Sá

Bachelor of Science in Biomedical Engineering

Diffusion Microscopic Anisotropy Estimation in the brain

Dissertation submitted in partial fulfillment of the requirements

for the degree of Master of Science in

Biomedical Engineering

Advisor: Doctor Rafael Neto Henriques,

Post-doctoral researcher at the Champalimaud Research,

Champalimaud Centre of the Unknown, Lisboa

Co-advisor: Prof. Doctor Ricardo Vigário

Associate professor at Universidade Nova de Lisboa

Faculdade de Ciências e Tecnologia

Physics Department

November 2020

FACULDADE DE CIÊNCIAS E TECNOLOGIA
UNIVERSIDADE NOVA DE LISBOA

Diffusion Microscopic Anisotropy Estimation in the brain

To my dad,

Acknowledgments

First and foremost, I would like to acknowledge the institution that provided my academical and personal progress, the Faculdade de Ciências e Tecnologias of Universidade Nova de Lisboa. In particular to the Physics Department for all the attention given to the improvement of the Biomedical Engineering course.

I want to thank my advisor Doctor Rafael Neto Henriques for all the help given throughout this project, for all the time made available and for all the life advice given that will certainly be carried with me to the future. Doctor Rafael Neto Henriques will always be on my memory for being one of the most hard working and motivated people I had the pleasure to meet. Many thanks to my co-advisor Prof. Doctor Ricardo Vigário for the opportunity to work on this project.

To professors with great impact in my academical growth, I would like to thank Professor Ruy Araújo da Costa, for all the support given during the less greater times in life, and Professor Elsa Feio for showing me my true potential.

I would like to thank my family and friends. To my mother and sister, the people I want to be the proudest of me, for being the strongest people I know, to my aunt Anabela for striving to see me happy, to my aunt Alzira for always checking in on my progress and to my grandparents for always believing in me. Thanks to all my friends and colleagues, especially Carolina Marquês for being like a second family and for all the moments we have spent over these last five years.

Latterly I would like to give a big thanks to Checa, hopefully my future wife, for everything she's done for me, for being my soulmate, for being the only person that really gets me, for growing up with me and making me see life with a different purpose, I love you.

Abstract

Diffusion MRI (dMRI) is a non-invasive technique sensitive to microstructural changes that cannot be resolved by other conventional imaging techniques. Diffusion anisotropy measures from conventional dMRI techniques, such as Diffusion Tensor Imaging, do not only depend on tissue microstructural properties but are also confounded by tissue orientational dispersion. As an attempt to suppress this confounding effect, more advanced dMRI imaging techniques based on non-conventional diffusion MRI had been recently developed to quantify the microscopic diffusion fractional anisotropy (μFA) without any prior assumptions of the underlying tissue. Measuring μFA allows the assessment of microstructural alterations related to tissue maturation, degeneration, and pathology independently of changes in tissue organization. However, non-conventional dMRI sequences are not easily accessible on current clinical MRI scanners. Therefore, more recent studies had suggested the use of microstructural models to quantify μFA from data acquired from conventional dMRI sequences. In this dissertation, the first reference open-source implementations of different microstructural models to estimate μFA are provided, in which by computing the spherical mean of the signal acquired, the orientation's influence from the dMRI data is withdrawn. These models included the one and two-compartmental spherical mean techniques (SMT1 and SMT2) and a novel adaption of the fiber ball imaging model for μFA estimation. The implementation of these models is evaluated based on numerical simulations, tested on open-source in vivo data of a healthy human brain, and finally compared to the gold standard reference estimated from non-conventional dMRI sequences in a pre-clinical setting. Results show that though their parameter estimates are independent to tissue orientation effect, the SMT1 and SMT2 models provide over and underestimated values of μFA, which were shown to be a consequence of their imposed assumptions. Although the adapted version of the FBI model did not show to provide robust μFA estimates, its' axonal water fraction estimates showed a high correlation to the gold standard μFA estimates. This finding supports that axonal water fraction is

a determinant factor of μFA in heathy neural tissues. Therefore, in future studies, the further development of alternative techniques to estimate μFA based on the information captured by FBI's axonal water estimates could be of interest.

Keywords: diffusion MRI, single diffusion encoding, double diffusion encoding, microscopic fractional anisotropy, spherical mean technique, fiber ball imaging

Resumo

A ressonância magnética por difusão (dMRI, do inglês *diffusion magnetic resonance imaging*) é uma técnica não invasiva, sensível a alterações microestruturais que podem não ser resolvidas por outras técnicas de imagem estruturais convencionais. As medidas de anisotropia, a partir de técnicas convencionais de dMRI, não dependem apenas das propriedades microestruturais do tecido, mas também da dispersão na orientação do tecido. Na tentativa de suprimir esse efeito, foram recentemente desenvolvidas técnicas mais avançadas de imagem de ressonância magnética por difusão baseadas em sequências de difusão não convencionais de forma a quantificar a anisotropia microscópica fracionária de difusão (μFA, do inglês *microscopic fractional anisotropy*) sem qualquer suposição prévia sobre o tecido subjacente. A medição da anisotropia microscópica de difusão permite a avaliação das alterações microestruturais relacionadas à maturação, degeneração e patologia de um tecido, independentemente das alterações na organização do mesmo. No entanto, as sequências de dMRI não convencionais não são facilmente acessíveis nos aparelhos de ressonância magnética atuais. Posto isto, estudos mais recentes sugeriram o uso de modelos microestruturais para quantificar μFA a partir de dados adquiridos através de sequências de dMRI convencionais. No decorrer desta dissertação, são fornecidas as primeiras implementações de diferentes modelos microestruturais de referência em open-source para estimar μFA. Modelos estes que através do cálculo da média esférica de um sinal adquirido, retiram a influência da orientação nos dados de dMRI. Esses modelos incluem as técnicas baseadas em médias esféricas de um sinal dMRI (SMT, do inglês *Spherical Mean Techniques*), de um e dois compartimentos, (SMT1 e SMT2) e uma nova adaptação do modelo da imagem por fibras em bola (FBI, do inglês *Fiber Ball Imaging*) para estimar o μFA. A implementação dos modelos é avaliada tendo como base simulações numéricas, testadas em dados de cérebros humanos saudáveis, adquiridos *in vivo*. Finalmente, o μFA é então comparado

com a referência padrão estimada a partir de sequências dMRI não convencionais, num ambiente pré-clínico. Os resultados mostram que, embora as estimativas dos parâmetros sejam independentes do efeito da orientação do tecido, os modelos SMT1 e SMT2 fornecem valores de μFA acima e abaixo da referência, o que se mostra ser uma consequência das suposições impostas. Embora a versão adaptada do modelo FBI não tenha resultado em estimativas robustas de μFA, as suas estimativas da fração de água axonal (*AWF*, do inglês *axonal water fraction*) evidenciaram uma alta correlação com as estimativas padrão de μFA. Assim, estes resultados demonstram que a *AWF* é, efetivamente, um fator determinante de μFA em tecidos neuronais saudáveis. No que concerne a estudos futuros, pode revelar-se interessante analisar o desenvolvimento de técnicas alternativas para estimar μFA com base em informações obtidas pelas estimativas de *AWF* do modelo FBI.

Palavras-chave: MRI de difusão, *single diffusion encoding*, *double diffusion encoding*, anisotropia microscópica fracionária de difusão, técnica das médias esféricas, modelo da imagem por fibras em bola

Contents

Figure List

Table List

Nomenclature

MRI	Magnetic Resonance Imaging
dMRI	Diffusion-weighted Magnetic Resonance Imaging
Dipy	Diffusion Imaging in Python
DWI	Diffusion weighted image
RF	Radio-frequency
FID	Free Induction Decay
SDE	Single diffusion encoding
DDE	Double diffusion encoding
SMT	Spherical mean technique
SMT1	One compartment spherical mean technique
SMT2	Two compartments spherical mean technique
FBI	Fiber ball imaging
μFA	Microscopic fractional anisotropy
D	Diffusivity
S	Diffusion weighted signal
S_0	Signal in the absence of diffusion

b	b-value
DTI	Diffusion Tensor imaging
DKI	Diffusion Kurtosis Imaging
FA	Fractional anisotropy
3D	Three dimensional
NDI	Neurite Density imaging
NODDI	Neurite Orientation Dispersion and Density Imaging
CSF	Cerebrospinal fluid
ODF	Orientation distribution function
AWF	Axonal water fraction
f	Water volume fraction
f_e	Extracellular water volume fraction
$\lambda_{\parallel}$	Axial diffusivity
$\lambda_{\parallel}^{e}$	Extracellular axial diffusivity
$\lambda_{\parallel}^{i}$	Intracellular axial diffusivity
$\lambda_{\perp}$	Radial diffusivity
$\lambda_{\perp}^{e}$	Extracellular radial diffusivity
$\lambda_{\perp}^{i}$	Intracellular radial diffusivity
D_i	Diffusion tensor

D_i^{int}	Intracellular diffusion tensor
D_i^{ext}	Extracellular diffusion tensor
$\bar{E}_{SM}$	Spherical mean signal
$\bar{E}_{SMT1}$	SMT1 spherical mean signal
$\bar{E}_{SMT2}$	SMT2 spherical mean signal
SNR	Signal-to-noise ratio
erf	Error function
MD_i	Mean diffusivity of compartment i

1

Context

1.1 Diffusion-weighted Magnetic Resonance Imaging

Magnetic Resonance Imaging (MRI) is a non-invasive imaging method capable of mapping the structure and function of entire tissues or organs (Tang et al., 1996). For instance, MRI is the primary method used by neuroscientists interested in understanding how the architecture of the brain differs in states of health and disease and how it can affect mental health.

In contrast to other imaging methodology, MRI is a multimodal technique in which different specialized sequences can be used to capture distinct structural and functional information of tissue. For instance, Diffusion-weighted Magnetic Resonance Imaging employs sequences sensitive to the diffusion of water in biological tissues (dMRI; Le Bihan et al., 1986). This information can be used to provide an indirect assessment of microstructural properties of tissue (Basser et al., 1994). In the context of brain tissue, conventional dMRI techniques can be used to characterize the anisotropy of water diffusion (Basser & Pierpaoli et. al, 1996) which can provide an indirect assessment of the integrity of white matter tissues

as well as the direction of white matter neuronal pathways (Basser et al., 2000; Basser & pierpaoli, 1996).

Diffusion anisotropy measures of conventional dMRI techniques, however, do not depend only on tissue microstructural properties. These are also confounded by the organization of tissue compartments. Indeed, on complex organised structures, as brain regions of crossing white matter fibers or gray matter, diffusion anisotropy is not only dependent to the shape anisotropy of microstructural compartments but also on their direction organization (i.e., crossing, fanning or dispersion of microstructural compartments) (Wheeler-Kingshott et al., 2009; De Santis et al., 2014).

As an attempt to suppress this confounding effect, more advanced dMRI imaging techniques had been recently developed to quantify the diffusion microscopic anisotropy - a quantity that reflects the mean anisotropy of different compartments rather than a directional distribution of microstructural compartments (Kaden et al., 2016a; Jensen et al., 2016). These studies suggest that measuring diffusion microscopic anisotropy is advantageous since this will allow the assessment of microstructural alteration related to tissue maturation, degeneration, and pathology independently to changes on tissue organization.

Preliminary dMRI strategies to measure microscopic anisotropy were based on advanced diffusion-weighted sequences (Shemesh et al., 2015; Henriques et al., 2019). Using advanced sequences, microscopic anisotropy can be estimated without any prior assumptions of the underlying tissue, however, advanced dMRI sequences are not easily accessible on current clinical MRI scanners. More recently, Kaden et al. (2016) suggested the estimation of diffusion microscopic anisotropy but applying advanced microstructural models to conventional dMRI sequences. In this dissertation, microscopic anisotropy estimation from different microstructural models will be explored.

1.2 Diffusion Imaging in Python

DMRI is a large and complex field of study, hence the need of a reference software to facilitate its exploration. To that end, the Diffusion Imaging in Python (Dipy) project was created – a collective effort project with the main goal of creating an open-source library of dMRI techniques (Garyfallidis et al., 2014).

Python is an object-oriented programming language designed with an emphasis on code readability, allowing scientists and researchers, not trained as computing engineers, to understand the computational methods taken and to easily be able to expand the software.

By being an open-source project, it brings many advantages to the technological advancement of dMRI image analysis such as:

- Increasing the transparency of the implementation of novel technological solutions, easing their understanding, validation and further development by independent researchers;
- Rising prosperous communities, linked by a common effort to support and improve a beneficial solution for the scientific development;
- Providing reference and secure technological implementations. Having reference open-source software is beneficial for research reproducibility by avoiding research studies based on multiple in-house software implementations that may have different estimation robustness. Open-source software code promotes also the security of implementation due to its thorough reviews.

At the moment, many tools and techniques for image analysis are already incorporated in the Dipy library, including pre-processing methods, conventional techniques used for diffusion anisotropy estimation, and algorithms for the virtual construction of white matter tracts (tractography). On the other hand, as dMRI is a field of study still under development, many advanced techniques have not yet been incorporated in the Dipy project. These include techniques for estimating tissue's microscopic anisotropy.

2

Objectives and Contribution

2.1 Project Aim

To differentiate the microscopic properties of the tissues, microstructural models can be applied to datasets acquired by dMRI. Alternatively, advanced sequences in dMRI can be used to acquire estimates of tissue's microscopic anisotropy.

The aim of the master project was to provide the first reference implementations for the estimation of microscopic anisotropy quantities. Since advanced dMRI sequences are currently not available on clinical acquisitions, this project first focuses on the implementation of microscopic diffusion anisotropy quantities based on two recently proposed microstructural models: 1) the 1-compartment spherical mean technique (SMT1) model (Kaden et al., 2016a); 2) the 2-compartments spherical mean technique (SMT2) model (Kaden et al., 2016a). Additionally, a novel expansion of the fiber ball imaging (FBI) model to estimate microscopic anisotropy was implemented and tested for the first time (Jensen et al., 2016). The implementations of all these microstructural models are tested using numerical simulations. Finally, to validate the different model based microscopic diffusion anisotropy estimates, these are compared to the estimates obtained

from advanced dMRI sequences which will be treated as gold standard estimates, since these do not depend on tissue models and their assumptions.

In order to ensure the replicability of the work and promote a wider use of microscopic anisotropy estimates in future research (focusing on possible future development or applications), all implementations carried out in this project are performed according to the documentation and code style adopted by the Diffusion Imaging in python (Dipy) open-source project.

2.2 Project Outline

Table 1 shows the project work plan on which the dissertation was based. It involved different steps from understanding the workflow required for Dipy code development to the implementation of the microstructural models that allow the estimation of brain microscopic anisotropy. Particularly, the first task of the project (which started in February) consisted in getting familiarized with the structure of Diffusion-MRI datasets and how to perform basic processing steps using previous developed tools in Dipy's software. This was followed by learning how to contribute for a large-scale open-source project by implementing the SMT1 and SMT2 models in the structure required by the Dipy project (from march to June). The tests to check the proper implementation of the SMT1 and SMT2 models and to study the robustness of their parameter estimates are reported in Chapter 5. These implementations are then expanded (from June to August) by testing for the first time an expansion of the FBI model for microscopic anisotropy. Results from the adapted FBI model implementation are shown in chapter 6. Afterwards (in September and October), the anisotropy measures obtained from the three different models (SMT1, SMT2, and FBI) were compared to the gold standard estimates obtained from advanced dMRI se-

quences in a pre-clinical environment. This validation study is reported in chapter 7 of the current thesis. The last two months of the project (October and November) were reserved to wrap up the project and conclude the thesis writing.

Table 1 – Project plan for the master thesis project

Tasks	feb	mar	apr	may	jun	jul	aug	sep	oct	nov
Get familiarized with the structure of Diffusion-MRI datasets and how to perform basic processing steps using previous developed tools in DIPY's software.	X	X								
Implementation of SMT1 in the format required by Dipy : implementation , testing, exploring acquisition requirements and testing models when assumptions are not met		X	X	X						
Implementation of SMT2 in the format required by Dipy : implementations, testing, exploring acquisition requirements and testing models when assumptions are not met			X	X	X					
Implement previous AWF estimates of FBI and expand the model to estimate diffusivities of compartments and its uFA estimates					X	X	X			
Validate SMT1, SMT2 & FBI estimates in pre-clinical data and using the reference uFA estimates from advanced double diffusion encodings.								X	X	
Time reserved to wrap up the project and write up the thesis									X	X

3

Theoretical Concepts

3.1 Diffusion principles

Diffusion is a physical process of matter transportation (atoms, molecules or particles) in liquids or gases due to its thermal energy. This process describes, for example, the movement of particles from a highly concentrated area to a less concentrated one in a medium, until an equilibrium is reached. Nonetheless, this movement prevails even when there is a stable and uniform particles concentration (absence of concentration gradient (Heitjans & Kärger, 2005). Despite being in equilibrium, due to kinetic energy, each particle suggests constant displacements and collisions with the environment, and consequently shows a random trajectory, as illustrated in Figure 1. This random movement of particles is labelled as Brownian Motion (Brown, 1827).

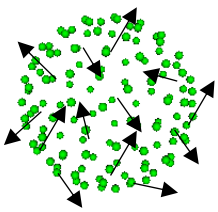

Figure 1 – Brownian motion representation.

3.2 Diffusion Coefficient

The Diffusion Coefficient or Diffusivity describes how fast the particles diffuse in a medium (in $\mu m^2/ms$). According to the Stokes-Einstein equation for Brownian diffusion, the diffusion coefficient depends on intrinsic properties of the medium as stated in (Freedman, 1983):

$$D = \frac{kT}{6\pi\eta a} \tag{3.1}$$

where k is the Boltzmann constant given by 1.30864×10^{-23} J/K, T is the mean temperature, a is the particle radius and lastly η represents the medium viscosity.

3.3 Gaussian Distribution

Although the total flow of particles from more concentrated to less concentrated areas can be described by Fick's laws of diffusion, the Brownian motion was only mathematically described in 1905, by Albert Einstein (Einstein, 1956).

According to Einstein (Einstein, 1956), the probability that a particle will shift in a free diffusion time period is described by a Gaussian distribution function (Figure 2):

$$P(\Delta r, t) = \frac{1}{\sqrt{(4\pi \mathrm{Dt})^3}} \mathrm{e}^{-\frac{r^2}{4Dt}} \tag{3.2}$$

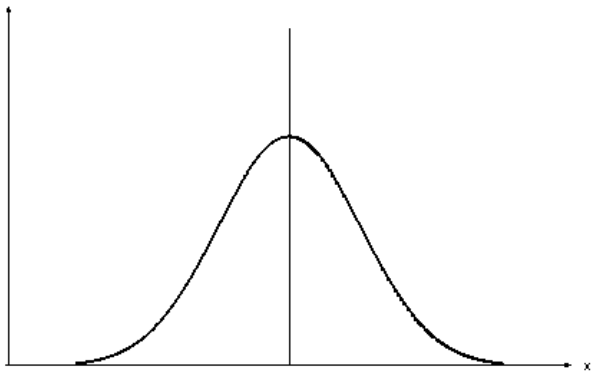

Figure 2 - Representation of a Gaussian distribution, which describes the probability density function of a particle's displacement pointed in equation 3.2.

As molecules displacements tend to increase after large periods of time and particles shift more rapidly for higher diffusivity values, the particle displacement gaussian distribution is wider for higher diffusion times and higher values of diffusivity (Figure 3).

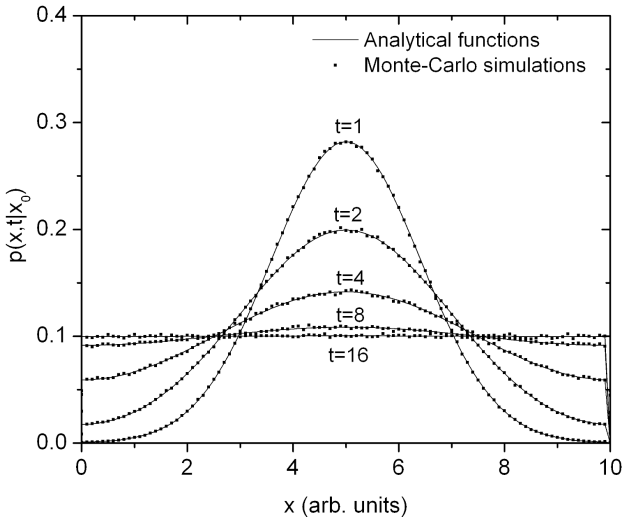

Figure 3 - Simulation of the particle's displacement distribution against increasing displacements, for several time values. Image taken from Plante, I., & A., F. (2013). Monte-Carlo Simulation of Particle Diffusion in Various Geometries and Application to Chemistry and Biology. In Theory and Applications of Monte Carlo Simulations. https://doi.org/10.5772/53203

3.4 Anisotropic and Non-Gaussian Diffusion in biological tissues

For most fluids the diffusion is equivalent in all directions. These substances are called isotropic and are characterized by a single diffusion coefficient, such as water that has a diffusion coefficient value of 3 $\mu m^2/ms$ at 37 ºC (Le Bihan & Lima, 2015). On the other hand, diffusing particles in biological tissues are hampered by many aligned obstacles such as cell membranes, organelles, macromolecules (Turner et al.,1990). In this case diffusion is anisotropic since it varies according to its measured direction (Beaulieu, 2002). For instance, in brain white matter, diffusion has a high degree of anisotropy due to 1) the elongated microscopic shape of its cells and 2) the high directional coherence of its nerve fibers. In this brain tissue, diffusion is higher in the direction parallel to these fibers (Moseley et al.,1990). Since the diffusion anisotropy depends on two factors (i.e., compartment shape anisotropy and compartments directional coherence), it is useful to define microscopic diffusion anisotropy as the sources of anisotropy risen from the microscopic shape of tissue compartments rather than their mesoscopic directional coherence (Szczepankiewicz et. al, 2015, Ianuş et al., 2018).

Besides anisotropy, water diffusion in biological tissues poses properties that deviate from the Gaussian distribution. While the formality proposed by Einstein was derived for the case of free diffusion of molecules, the molecular displacement distribution of water particles in a biological tissue can diverge from a gaussian distribution due to the presence of cell membranes, organelles, macromolecules (Turner et al.,1990).

3.5 Magnetic Resonance Imaging

Magnetic Resonance Imaging is based on the emission and absorption of energy in the radio waves frequency of the electromagnetic spectrum and the principles of nuclear magnetic resonance. By means of the production of images through spatial variations in phase and frequency of the energy absorbed and emitted by the object, MRI images of objects smaller than their wavelength are obtained. In order to be able to create a magnetic resonance image, Helmholtz coils are used to standardize the B_0 magnetic field to be applied to the protons.

3.5.1 Nuclear Magnetic Resonance phenomenon

Since resonance is defined as the interaction of a system at its own frequency, nuclear magnetic resonance is observed in any type of isotope that has a total spin greater than zero. The hydrogen is the most used isotope for MRI, due to being the most sensitive and abundant in human tissues (Weast, 1972).

From the classical point of view, due to protons' positive charge and the angular momentum that is intrinsic to it, it presents a magnetic dipole moment. From a quantum point of view, there are quantized energy transitions and for the proton to shift from one energy level to another it has to absorb $\Delta E = \gamma\hbar|B_0|$ (Carrington & McLachlan, 1967), with its own frequency:

$$\omega_0 = \gamma|B_0| \tag{3.3}$$

given by the Larmor equation with B_0 as the incident magnetic field, γ as the gyromagnetic constant and $\hbar$ the Planck's constant.

3.5.2 Magnetic Resonance Imaging principles

According to the Heisenberg's uncertainty principle it is not possible to know the exact direction of the magnetic moment of a particular proton (Heisenberg, 1927). Nonetheless, the spins of an atom align themselves depending on the presence or absence of an incident magnetic field. When the proton is immersed in an external magnetic field, there is an alignment of the nuclear spin vectors and the angular momentum changes direction causing the proton to precess around the direction of the applied magnetic field (Harris, 1983). Due to the presence of magnetic moment in the protons, this magnetic moment also aligns with the applied magnetic field and it is possible to discourse total magnetization (sum of the proton's magnetic moments) (Brown & Semelka, 2005). This total magnetization is divided into two components: longitudinal and transverse; and it is null in the absence of a magnetic field.

In the well-known scientifical experiments, Bloch, Purcell and colleagues created a continuous wave technique through the use of a radio-frequency (RF) field with fixed frequency (B_1). When a group of spins is placed under a B_0 magnetic field, each spin aligns in one of two possible orientations: parallel or anti-parallel, with the spins oriented in parallel at a lower energy level than the anti-parallel spins (Brown & Semelka, 2005). This energy difference is proportional to the Larmor frequency and corresponds to the energy needed for electronic transitions to occur between the two levels. Recalling the Zeeman Effect (Zeeman, 1897), when a radio frequency pulse, B_1, is applied, the protons absorb energy and the number of spins oriented in anti-parallel increase and consequently there is a decrease in the longitudinal component of the total magnetization. This decrease in the longitudinal component of the magnetization leads to an increase in the transverse component of the total magnetization (transverse magnetization), which corresponds to the magnetization detected by coils positioned perpendicularly to the magnetic field B_0.

When the radiofrequency pulses are turned off, the spins return to their initial state and when shifting to lower energy levels, they emit energy to the environment and to the surrounding spins (Brown & Semelka, 2005). The energy

transferred to the environment causes an increase in the intensity of the longitudinal component of the resulting magnetization while the energy transferred to the surrounding spins induces a faster decrease in the transversal component of the magnetization - these effects are described in more detail below.

3.5.3 Transverse and Longitudinal Relaxation

During relaxation electromagnetic energy is emitted, this RF emitted energy is the nuclear magnetic resonance signal. Relaxation combines two different mechanisms: transverse and longitudinal relaxation, the transverse being the faster mechanism.

The phenomenon of Longitudinal Relaxation is due to the energy exchanges between the spins and the environment and is also known as spin-lattice relaxation. As the spins shift from a higher energy level back to a lower energy level, RF energy is released into the environment's medium (or also referred to as lattice).

This magnetization recovery follows an exponential curve and is characterized by the time constant T_1, which is defined as the time required for longitudinal magnetization to recover 63% of its intensity. The T_1 time constant is specific to each tissue and depends on the intensity of the magnetic field (the larger the field, the larger the T_1; Bottomley et al., 1984).

The transverse relaxation is due to the dephasing of the spins. As the spins move, their magnetic fields will interact, changing the precession rhythm, a phenomenon known as spin-spin relaxation. Although these interactions are random and temporary, spin-spin relaxation causes an accumulated phase loss that consequently causes the transverse magnetizations' decay. This decay follows an exponential curve and is characterized by the time constant T_2 defined as the time at which the transverse magnetization loses 63% of its initial intensity. Like T_1

time, T_2 time is specific to each tissue and depends on the magnetic field's intensity.

After the systems' stimulation with the application of a magnetic pulse at 90º, B_1, a resulting magnetization is induced in the xy plane, which previously did not exist. When the application of the magnetic pulse ceases, there is a dephasing of spins and loss of intensity of the electromagnetic signal. This decay of magnetization is called Free Induction Decay (FID) (Farrar, 1987).

3.5.4 Spin-Echo Sequence

Even though the application of a single RF pulse at 90º is capable of producing a signal, the measured signal is not described by the pure decay of the relaxation time T_2. The reason for this is the loss of phase coherence of the spins caused by field inhomogeneities (McRobbie et al., 2006). For these effects to be eliminated, the spin-echo sequence (Hahn, 1950) is used, which is characterized by the spin's excitation through the application of two radio frequency pulses and represented in Figure 4. Firstly, a 90º RF pulse responsible for the rotation of the magnetization vector to the xy plane is applied (Figure 4B). After applying this RF 90º pulse, there is a spin dephasing due to the field inhomogeneities (Figure 4C – D) - note that, for Figure simplification, the dephasing spins due to spin-lattice and spin-spin interactions are not represented. A 180º pulse is then applied (Figure 4C - E, Farrar & Becker, 1971), causing magnetization vectors to partially return to phase (Figure 4F) and causes the magnetization to rotate around the x axis, creating an echo in which the dephasing spins induced by field inhomogeneities are eliminated (after time TE has passed since the signal acquisition).

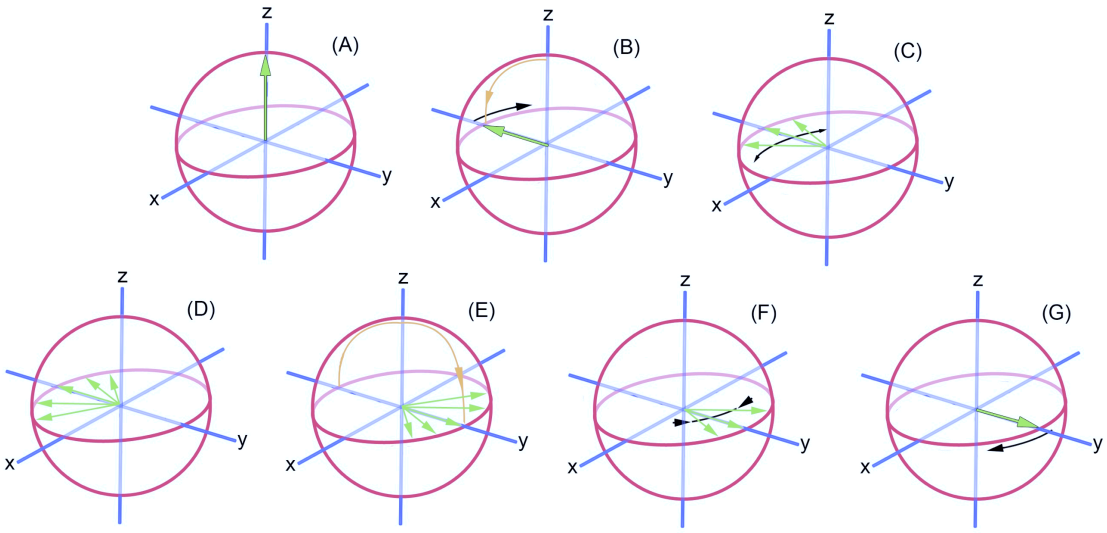

Figure 4 – Spin-Echo sequence diagram. Image retrieved from MRI online course (Magnetic Resonance Imaging). (n.d.). Retrieved December 19, 2019, from https://www.imaios.com/en/e-Courses/e-MRI/

3.5.5 Spatial Encoding

Each image voxel can be encoded using specific planes isolation, in each of the three directions of the Cartesian coordinate system, through a set of pulsed magnetic field gradients: slice selection gradient (in the z axis), phase encoding gradient (in the y axis) and the frequency encoding gradient (in the x axis) (McRobbie et al., 2006).

Initially every proton precess (gyroscopic effect based on the change in the rotational axis) with the same frequency. A slice selection gradient (SSG) is vertically applied, which causes a variable resonance frequency proportional to the field intensity. By applying a RF pulse, with a specific frequency, only the protons in the plane with that same frequency will respond given that only the hydrogen nuclei of this plane are excited and emit energy.

The second step in spatial encoding is the application of a phase encoding gradient (PEG). This field gradient modifies the spin's resonance frequency and

induces the spins to diphase, which prevails when the gradient application is interrupted. Thusly each line of voxels is encoded by the spin's phase, with each line of spins having a different phase.

Lastly, a frequency encoding gradient (rereferred to as FEG in Figure 5) is applied. This gradient modifies the Larmor frequencies horizontally during the time it is applied. Columns are then created, each with an identical Larmor frequency.

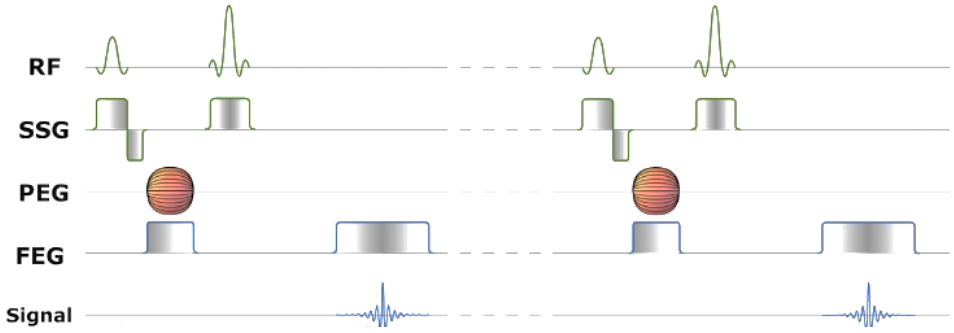

Figure 5 - Spatial encoding diagram. Image retrieved from MRI online course (Magnetic Resonance Imaging). (n.d.). Retrieved December 19, 2019, from https://www.imaios.com/en/e-Courses/e-MRI/

The information collected when applying the magnetic field gradients, represented in Figure 5, is acquired in the space frequency domain, the K space (Likes, 1979).

3.5.6 K-space and Image Reconstruction

The K space is a matrix that contains information regarding the frequencies and phases of the acquired signals. Each time an echo is created, the signal is acquired and a line in the k space is filled, although each point does not correspond to a point in the final image. By rearranging the frequencies in this space so that the lowest frequencies are in the center, the center will contain information about the image contrast, while the peripheral lines of this space will contain information about the resolution of the image.

For the image reconstruction, an inverse of the Fourier Transform is applied to the signal. Herewith the signal is converted from the frequency domain to the spatial domain where the image is observed.

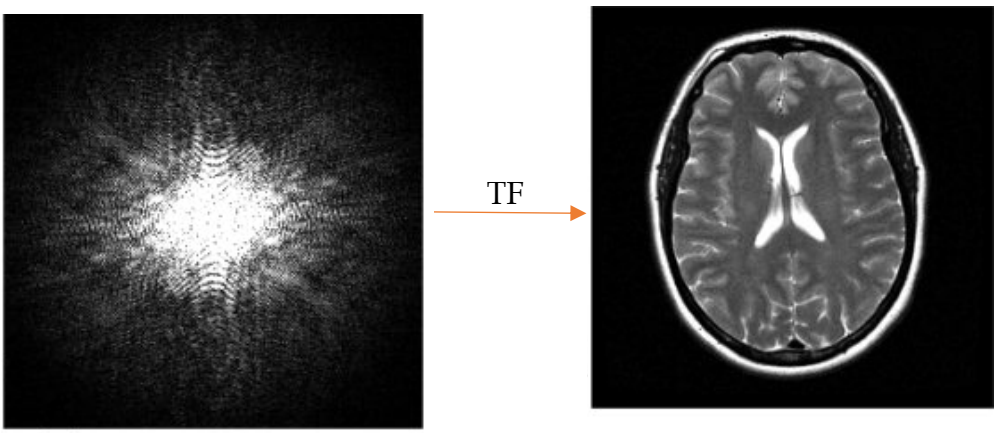

Figure 6 - K space transformation in an image, through the Fourier Transform. Images adapted from MRI online course (Magnetic Resonance Imaging). (n.d.). Retrieved January 10, 2020, from https://www.imaios.com/en/e-Courses/e-MRI/

3.6 Diffusion-weighted Magnetic Resonance Imaging

Diffusion magnetic resonance imaging allows the production of images weighted by water diffusion properties of biological tissues (Stejskal & Tanner, 1965; Le Bihan et al., 1986). For the MRI contrast to be influenced by water diffusion, additional diffusion gradients are applied during the preparatory phase of the image acquisition. For example, the conventional sequence for acquiring diffusion-weighted images can be implemented by adding an additional set of magnetic field gradients to the spin-echo sequence (Figure 7).

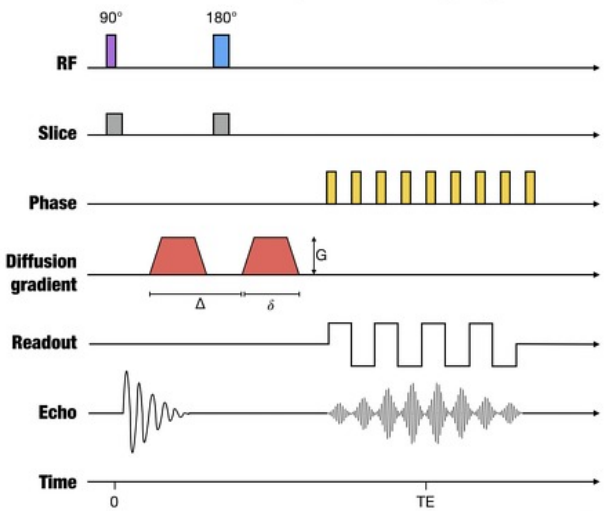

Figure 7 – Echo planar diffusion-weighted imaging pulse sequences. Image taken from Diffusion weighted imaging | Radiology Reference Article | Radiopaedia.org. (n.d.). Retrieved January 24, 2020, from https://radiopaedia.org/articles/diffusion-weighted-imaging-1

The purpose of this additional set of gradients is to cause an additional dephasing in the spin's magnetization that moved to a new location within a given time interval due to the diffusion process. In addition to decreasing its intensity, this additional dephasing makes the signal dependent on the diffusion coefficient. For free water, the diffusion weighted signal is expressed by:

$$S = S_0 \exp(-Db) \tag{3.4}$$

where S represents the measured signal, S_0 represents the signal in the absence of diffusion gradients and b is a coefficient called the b-value, which depends only on the diffusion weighted MRI sequence parameters (Le Bihan et al., 1986) and measures the degree of diffusion applied. The longer the time and the intensity of the magnetic field, the more attenuated the signal is.

A diffusion weighted image (DWI) is an image obtained by dMRI (Figure 8B). Besides the information regarding the water diffusion in biological tissues, this image also contains information on T_1 and T_2 weighting. However, the influences of relaxation times on the image can be removed using an S_0 image acquired without applied diffusion gradients (Figure 8A). It is also important to note that diffusion-weighted images contain information about the anisotropic and non-Gaussian properties of water diffusion in biological tissues. These properties can be estimated by acquiring images for different parameters (different diffusion gradient directions and/or different b-values) or types of diffusion gradients and using different reconstruction techniques. These reconstruction techniques will be described in chapter 4: "State of the Art".

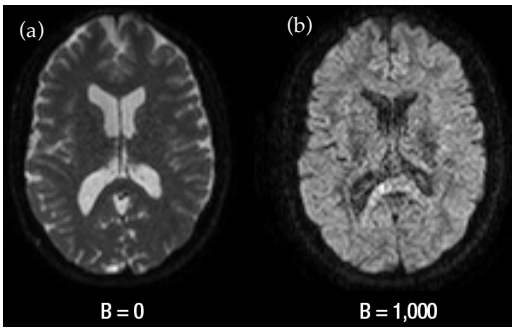

Figure 8 – Image acquired with diffusion MRI. In the left image, panel (a), diffusion is not taken into account (B=0) while the right image, panel (b), is a diffusion weighted image (B=1000). Image taken from Diffusion Tensor Imaging (DTI) - Fiber Tracking - Imagilys. (n.d.). Retrieved January 24, 2020, from https://www.imagilys.com/diffusion-tensor-imaging-dti/

4

State of Art

Diffusion MRI is an MRI modality that provides quantitative images with information about structures smaller than the size of a voxel. Therefore, this technology has been widely used to infer structural changes at microscopic levels in both healthy and injured tissues. Several dMRI methods have been proposed to summarize the multi-dimensional information captured by the diffusion-weighted images and to quantify specific properties of the diffusion process in biological tissues (e.g., the diffusion micro-anisotropy estimation). Below, the state-of-the-art of different dMRI methods employed to characterize diffusion in biological tissues from 1) conventional dMRI sequences and 2) and advanced dMRI sequences are reviewed.

4.1 Techniques based on Conventional Sequences

As explained in chapter 3, the conventional sequences for diffusion-weighted imaging consist of applying a pair of magnetic field gradients separated by a diffusion time (Stejskal & Tanner, 1965), Figure 7. This sequence is referred to as single diffusion encoding (SDE) since it measures diffusion along individual directions and different diffusion weights (Shemesh et al., 2016). The different techniques to summarize the information captured by different diffusion gradient directions and weightings can be classified as two types: 1) signal representation models, and 2) microstructural models (Novikov et al., 2018).

4.1.1 Signal Representation Models

Signal Representation models were developed to characterize physical properties of diffusion (e.g., diffusion anisotropy or non-Gaussian degree of diffusion) without taking into consideration their biological relationship. The most used signal representation models are diffusion tensor imaging (DTI) and diffusion kurtosis imaging (DKI).

4.1.1.1 Diffusion Tensor Imaging

Diffusion Tensor Imaging (DTI) is a technique proposed to model the anisotropy of diffusion in the brain and obtain diffusion measurements that do not depend on the orientation of the applied magnetic field gradients (Basser et al., 1994).

With the application of magnetic field gradients in several directions, it is possible to create a diffusion tensor:

$$D = \begin{bmatrix} D_{xx} & D_{xy} & D_{xz} \\ D_{xy} & D_{yy} & D_{yz} \\ D_{xz} & D_{yz} & D_{zz} \end{bmatrix} \quad (4.1)$$

where the diagonal elements of the matrix represent the diffusion values along the x, y and z axes, and the other elements of the matrix correspond to the diffusion correlations between these 3 directions. Although the diffusion tensor reflects architectural features of the brain in tissues with organized microstructures, the diffusion tensor for a heterogeneous fiber architecture like crossing fibers only represents an average from individual compartments (Assaf et al., 2004).

The diffusion tensor can be geometrically represented by an ellipsoid (Figure 9). The main axes of the ellipsoid are related to the diffusion tensor through the eigenvectors (ε) while the values of diffusivity along the main axes of the ellipsoid are given by the eigenvalues (λ).

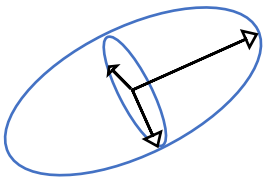

Figure 9 – Geometrical representation of an ellipsoid.

The latter can be used to estimate diffusion anisotropy. The most widely used anisotropy measure is Fractional Anisotropy (FA), which quantifies the fraction of diffusion that is anisotropic, defined as (Basser & Pierpaoli, 1996):

$$FA = \sqrt{\frac{(\lambda_1 - \lambda_2)^2 + (\lambda_2 - \lambda_3)^2 + (\lambda_1 - \lambda_3)^2}{2(\lambda_1^2 + \lambda_2^2 + \lambda_3^2)}} \qquad (4.2)$$

with FA ranging between 0 (perfect isotropic diffusion, i.e., perfect sphere) and 1 (elongated ellipsoid approaching a stick object).

The maximum diffusion direction measured by the diffusion tensor can give a proxy of the main direction of white matter fibers in a given voxel. Therefore, by comparing the diffusion tensor main direction across image voxels, DTI can be used to virtual construct white matter tracts (Figure 10). This 3D white matter reconstructions are typically referred to as Tractography (Basser et al., 2000). Although tractography may be useful for many applications (Le Bihan & Johansen-Berg & Behrens, 2014), this dissertation focuses on dMRI's scalar maps that aim to summarize tissue microstructure properties (e.g., FA maps).

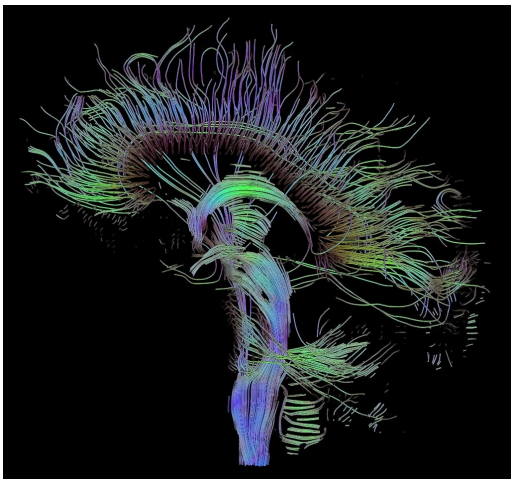

Figure 10 – Representation of an image by Tractography.

Even though fractional anisotropy is sensitive to the shape of microstructural compartments of well-aligned structures, it is also highly modulated by their orientation dispersion contained within each of the imaging voxels. For brain regions with complex microstructures (e.g. crossing white matter fibers and grey matter), this strong dependance rises a major limitation to the use of FA as a biomarker sensitive to microstructural properties (Szczepankiewicz et. al, 2015).

4.1.1.2 Diffusion Kurtosis Imaging

Due to the presence of barriers and obstacles on the intracellular and extracellular mediums, diffusion in biological tissues is non-Gaussian.

Diffusion Kurtosis Imaging (DKI) is an expansion of Diffusion Tensor Imaging that quantifies the non-Gaussian behavior of diffusion in biological tissues (Jensen et al., 2005) in addition to the diffusion tensor.

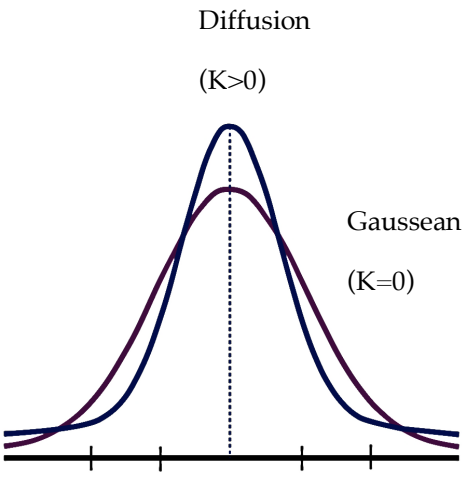

Figure 11 - Probability distributions of water molecules displacements; K=0 is a gaussian distribution and represents displacements in free diffusion while tissue's diffusion is characterized by a non-Gaussian distribution with K>0.

Previous studies have shown that measures of non-Gaussian diffusion from DKI can provide a better characterization of microstructural properties (Henriques et al., 2015; Henriques, 2018), since kurtosis averaged metrics are less dependent to mesoscopic tissue dispersion effects than the anisotropy measures provided from the diffusion tensor. However, since it does not provide a direct mathematical description of tissue, kurtosis measures are limited for not being able to distinguish different microscopic properties, such as the shape and variance of tissue properties (Henriques et al., 2020).

4.1.2 Microstructural Models

These techniques consist of applying a microstructure model of biological tissues directly to signals acquired by dMRI sequences, allowing it to infer the correlation between property changes in diffusion and the properties of tissues (Nilsson et al., 2013). Although the microstructural models were not initially designed to estimate the degree of microscopic anisotropy, its extracted compartmental diffusivities and volume fractions can be used to estimate the microscopic anisotropic indexes as later pointed by Henriques et al. (2019). The disadvantage of these techniques is that they depend on approximations that may not be correct and must be validated (Novikov et al., 2018; Henriques et al., 2019).

4.1.2.1 CHARMED model

To characterize anisotropic water diffusion in the brain, a combined hindered and restricted model of water diffusion was created, designated as CHARMED (Assaf et. al, 2004). This model explains the Gaussian and non-Gaussian signal attenuation caused by a sum of a finite number of hindered and restricted compartments, enabling the estimation of intra cellular and extra cellular diffusivities for different fiber populations.

The use of the CHARMED model is, however, limited for providing estimates with low precision since it involves the estimation of a large number of parameters. Moreover, the CHARMED model prevents it from recovering the effects of axonal orientation dispersion since it represents tissues by a discrete number of tissue elements (Huber et. al, 2019).

4.1.2.2 NDI model

The neurite density imaging (NDI) model was proposed to non-invasively estimate the density and the orientation distribution function of dendritic compartments (Jespersen et. al, 2007). As CHARMED, NDI models tissue as consisting in two types of components. Them being the extracellular space, modeled as isotropic mono-exponential diffusion decay, and the axons and dendrites represented as long cylinders modeled with two diffusion coefficients, parallel and perpendicular to its axes (Jespersen et. al, 2007). However, rather than modeling the tissues' orientation distribution function as a discrete sum of elements, NDI models the distribution of intra-cellular compartments through a spherical harmonics representation.

Although, compared to the CHARMED model, NDI is able to better represent both tissue dispersion and crossing, it still produces estimates with low precision due to the large number of parameters estimated, including the intra and extra cellular diffusivities, volume fractions, and the coefficients of the ODF's spherical harmonics representation.

4.1.2.3 NODDI model

Another popular modeling approach for estimating biologically specific properties of diffusion is the Neurite Orientation Dispersion and Density Imaging model (NODDI), which has been used to disentangle changes related to neurite density and orientation dispersion, major factors contributing to fractional anisotropy (Huber et. al, 2019).

NODDI trades the complex orientation distribution of the NDI model that uses spherical harmonics to represent distribution of intra-cellular compartments, to a fixed Watson distribution function (a function that is analogous to a Gaussian distribution in spherical coordinates, Zhang et al., 2012). Additionally, this model adopts three types of microstructural compartments, them being the intracellular, extracellular and cerebrospinal fluid. To capture the restricted diffusion perpendicular to neurites and unhindered diffusion along the neurites,

the intracellular compartment is modeled as sticks, while an effective anisotropic Gaussian diffusion (i.e., a single diffusion tensor) is used to model the diffusion in the extracellular compartment. Diffusion in the CSF compartment is modeled by the expected scalar diffusivity of free water at 37^{o} (Zhang et al., 2012). With these assumptions, NODDI focuses on the estimation of a reduced number of parameters that can be reliably estimated with practical acquisition protocols, enabling its clinical application.

However, although NODDI involves the estimation of a much smaller number of parameters when compared to the previous CHARMED and NDI models, it is based on model assumptions and constraints that may not be true for all biological environments. For instance, the Watson distribution for the orientation distribution function can only describe tissue dispersion along a single fiber direction, failing to represent tissue regions of crossing white matter bundles. Moreover, the NODDI model focuses only on the estimation of the volume fraction of the three compartments while fixing all their diffusivities for given priors (particularly, the intra axonal diffusivity is fixed to 1.7$\mu m^2/ms$, while the extra-cellular diffusivities are reconstructed based on the other model parameters).

For this model to be improved, strategies to release some of its assumptions needs to be taken into consideration.

4.1.2.4 Spherical Mean Technique Models and Fiber ball Imaging model

Table 2 shows a summary of the assumptions, limitations and potentials of the models described above. In short, the more general CHARMED and NDI models provide limited precision due to the large number of parameters to be estimated, while NODDI accuracy may be compromised by the strong constraints imposed on the ODF representation and compartmental diffusivities.

Table 2 – Microstructural models' comparison based on assumptions, limitations and potentials of the models.

	CHARMED	NDI	NODDI
Assumptions	Two type compartments: extra and intra cellular compartments (restricted or hindered) for 1 or more fiber populations	Two type compartments: extra (isotropic mono exponential diffusion) and intra (long cylinders) cellular compartments	Three type compartments: extra (anisotropic diffusion) and intra (sticks) cellular compartments and CSF compartment (isotropic diffusion)
Limitations	Large number of parameters Doesn´t model dispersion (just sharp single populations)	Large number of parameters Isotropic extra-cellular space	Assumes Watson distribution Constraints on all diffusivities
Potentials	Estimates intra-extra celular diffusivities for different fiber populations	Estimates intra-extra cellular diffusivities and the full ODF that can be used to estimate dispersion of fibers Tractography	Clinical applications Requires some non-weighted diffusion data

To provide models compatible in clinics and without relying on strong assumption on the orientation distribution functions, the models based on spherical means were created. These include the Spherical Mean Techniques (Kaden et al., 2016a) and the Fiber Ball Imaging technique (Jensen et al., 2016).

The advantage of these latter techniques is that they bypass the need of modelling or estimating the parameters of the orientation distribution function, because these models are fitted on spherical signal means (i.e., signals that are averaged across different directions) which are known to be independent to the shape of the orientation distribution function. Thus, since the models are fitted to mean signals, their parameters are intrinsically independent to tissue dispersion and crossing. Moreover, withdrawing the orientations' influence from the dMRI data and avoiding the need of estimating ODF parameters, allows the release of constraints imposed to the diffusivities of different compartments potentially promoting the robustness of microstructural models.

4.2 Techniques based on Advanced Sequences

Most of the dMRI techniques were developed for an acquisition carried out through Single Diffusion Encoding (SDE). However recently, there is a growing interest in exploring different acquisition protocols with different dMRI sequences, since these were shown to provide unique information about tissue microstructure (Shemesh et al., 2015) without requiring the extensive data acquisition protocols for fitting more general SDE microstructural models nor the on biological approximations.

Double diffusion encoding (DDE) is an example of an advanced diffusion MRI sequence (Shemesh et al., 2015). DDE consists of the signal acquisition after the application of two diffusion gradients that can have different directions and intensities. Without introducing any model on the microstructure, DDE measurements can be used to measure microscopic anisotropy from the angular dependence between the two diffusion gradient directions applied. Particularly, microscopic diffusion anisotropy can be directly measured using the DDE from the difference between the mean signals acquired from parallel and perpendicular gradient directions (Henriques et al., 2019; Henriques et al., 2020).

5

Spherical Mean Technique Implementation

5.1 Introduction

The main objective of the spherical mean technique (SMT) is to map microstructural parameters (e.g., and the per axon diffusivities (Kaden et al., 2016a), axonal density (Kaden et al., 2016b), microscopic anisotropy (Kaden et al., 2016, Henriques et al., 2019)) independently to the orientational distribution of tissue from conventional dMRI sequences. To accomplish that, SMT models are fitted to the spherical mean of a signal acquired from different diffusion gradient directions (also known as powder averaged signals) which was mathematically proved to be independent to the orientation distribution of the tissue compartments (Kaden et al., 2016a).

In the original spherical mean technique paper (Kaden et al., 2016a), a simple model has been proposed to estimate microscopic diffusion anisotropy, assuming that neural tissue can be represented by arbitrary oriented compartments with equal per axon axial and radial diffusivities. This one-compartment type model will be here referred to as the one-compartment spherical mean technique (SMT1) model.

As the description of mean signals are constrained to one-component type and it is assumed that any voxel can be fully described by one axial diffusivity $\lambda_{\parallel}$ (magnitude of diffusion parallel to fiber tracts) and one radial diffusivity $\lambda_{\perp}$ (magnitude of diffusion perpendicular to fiber tracts), the SMT1 models the spherical mean signal $\bar{E}_{SMT1}$ by

$$\bar{E}_{SMT1} = S_0 e^{-b\lambda_{\perp}} \frac{\sqrt{\pi}\,\mathrm{erf}\left(\sqrt{b(\lambda_{\parallel}-\lambda_{\perp})}\right)}{2\sqrt{b(\lambda_{\parallel}-\lambda_{\perp})}} \tag{5.1}$$

where S_0 is the signal magnitude without the diffusion gradient influence, *erf* is the error function and b is the b-value. Note that the SMT1 model does not present any variables related to the tissue orientation distribution function since these were removed by signal spherical averaging. For SMT1's $\lambda_{\parallel}$ and $\lambda_{\perp}$ estimation, equation 5.1 has to be fitted to dMRI data acquired with at least two non-zero b-values. These estimates can then be used to calculate indexes of the microscopic diffusion anisotropy. For instance, the microscopic fractional anisotropy μFA quantifies microscopic diffusion anisotropy in a normalized range from 0 (spherical compartments $\lambda_{\parallel} = \lambda_{\perp}$) to 1 (stick compartments $\lambda_{\parallel} \gg \lambda_{\perp}$) through

$$\mu FA_{\,SMT1} = \sqrt{\frac{(\lambda_{\parallel}-\lambda_{\perp})^2}{\left(\lambda_{\parallel}^{\,2}+2\lambda_{\perp}^{\,2}\right)}} \tag{5.2}$$

The spherical mean technique was later expanded into a two-compartment model to consider diffusivity differences between intracellular and extracellular compartments (Kaden et al., 2016b) - this will be referred to as two-compartmental spherical mean technique (SMT2) model. Since the mean signal decay with b-value does not provide enough information to robustly estimate the axial

and radial diffusivities for both compartments, the following relationships between the model parameters were imposed (Kaden et al., 2016b):

- the extracellular radial diffusivity $\lambda_{\perp}^{e}$ is described as a function of the extracellular axial diffusivity $\lambda_{\parallel}^{e}$ and the axonal volume fraction f assuming the first order tortuosity approximation of the microscopic diffusion process around the neurites: $\lambda_{\perp}^{e} = (1-f)\lambda_{\parallel}^{e}$;
- the intra-cellular axial diffusivity is equal to the extra-cellular axial diffusivity: $\lambda_{\parallel}^{i} = \lambda_{\parallel}^{e} = \lambda_{\parallel}$;
- the radial intrinsic diffusivity $\lambda_{\perp}^{i}$ is zero, assuming that the diffusion-weighting is not able to detect the attenuation of the intra-cellular perpendicular signal components at the commonly applied b-values in clinical practice: $\lambda_{\perp}^{i} = 0$.

where $\lambda_{\perp}^{e}$ and $\lambda_{\parallel}^{e}$ are the radial and axial diffusivities of the extracellular component respectively, $\lambda_{\perp}^{i}$ and $\lambda_{\parallel}^{i}$ are the radial and axial diffusivities of the intracellular component respectively, and f is the water volume fraction of the intracellular component. As the T_2 difference between the two non-exchanging water pools is not taken into consideration, axonal water fraction (*AWF*), defined as the ratio between the intra-axonal water and the sum of both intra-axonal and extra-axonal water, is a better terminology than volume fraction.

Given these constraints, the mean spherical signal for two gaussian compartments can be given by

$$\bar{E}_{SMT2} = f\,\frac{\sqrt{\pi}}{2}\frac{\operatorname{erf}\left(\sqrt{b\,\lambda_{\parallel}}\right)}{\sqrt{b\,\lambda_{\parallel}}} + \\ + (1-f)e^{-b(1-f)\lambda_{\parallel}}\frac{\operatorname{erf}\left(\sqrt{b\,f\lambda_{\parallel}}\right)}{\sqrt{b\,f\lambda_{\parallel}}} \tag{5.3}$$

Due to the constraints imposed, the microscopic fractional anisotropy obtained through the spherical mean technique for two compartments was shown to only rely on the estimated volume fraction (Henriques et al., 2019):

$$\mu FA_{SMT2} = \frac{\sqrt{3 \times (1 - 2fe^2 + fe^3}}{\sqrt{3 \times (2 + 2fe^3 + 4fe^4}} \quad (5.4)$$

where $fe = (1 - f)$ is the volume fraction of the extracellular compartment.

In this chapter, five groups of experiments based on numerical simulations are performed to test the robustness of SMT1 and SMT2 implementations and to assess the relationship between their estimates' precision and number of acquisition parameters. In addition, open-source data implementations of an *in vivo* human brain were tested for both spherical mean technique models.

5.2 Methods

5.2.1 Simulations

The first group of experiments is based on the use of single voxel simulations to create synthetic diffusion weighted signal to: 1) ensure that SMT models are properly implemented (experiment 1); 2) test the precision of SMT model estimates from data acquired with different dMRI acquisition protocols (experiments 2, 3 and 4); and 3) test the accuracy of the different SMT estimates when the ground truth parameters of simulations don't follow the same premises than SMT's model assumptions and constraints (experiment 5). For all experiments simulated signals were performed independently of SMT equation using multi-

tensors simulation. A multi-tensor simulation assumes that the tissue can be described by a sum of signal contributions from N different synthetic fiber populations each characterized by its own effective diffusion tensor $\boldsymbol{D}_i$, i.e.:

$$S(b,n) = S_0 \sum_{i=1}^{N} \frac{\exp(-bnD_i n^T)}{N} \tag{5.5}$$

where n is the diffusion gradient direction of a given experiment and S_0 is corresponds to the signal for b-value = 0.

Note that, for SMT1 model testing, multi tensor simulations are performed for N diffusion tensors D_i aligned to different directions of N fiber population, each defined by equal ground truth axial and radial diffusivities $\lambda_{\parallel}$ and $\lambda_{\perp}$. For SMT2 model testing, multi tensor simulations are performed for a sum of 2N diffusion tensors corresponding to two types of diffusion tensors aligned to N fiber populations: the intra and extra-cellular diffusion tensors D_i^{int} and D_i^{ext}. Specifying these tensors on the multi-tensor simulations, equation 5.5 can be rewritten as:

$$S(b,n) = S_0 f \sum_{i=1}^{N} \frac{\exp\left(-bnD_i^{int} n^T\right)}{N} + S_0(1-f) \sum_{i=1}^{N} \frac{\exp(-bnD_i^{ext} n^T)}{N} \tag{5.6}$$

where f is the axonal volume fraction. Note that while the D_i^{int} and D_i^{ext} are generated for N tensor main directions their diffusivities are defined by constant intra- and extra-cellular diffusivities $\lambda_{\parallel}^{i}$ and $\lambda_{\perp}^{i}$ (for tensors D_i^{int}) and $\lambda_{\parallel}^{e}$ and $\lambda_{\perp}^{e}$ (for tensors D_i^{ext}).

After the synthetic signals are produced for different b-values and gradient directions $S(b,n)$, spherical mean signals are computed by averaging the T_2-normalised diffusion signals acquired with N_{dir} uniformly sampled gradient directions for each b-value separately:

$$\bar{E}_{MTensor}(b) = \sum_{a=1}^{N_{dir}} \frac{S(b,n)}{S_0\, N_{dir}} \tag{5.7}$$

Experiment 1 - To test if the SMT model is properly implemented, the mean signal decays produced from the SMT1 and SMT2 models are compared to the reference mean signal decays independently produced using the multi-tensor simulations. To test the SMT models independently of the limited number of acquisition parameters, signals for the SMT models and multi-tensor simulations are produced for large number of 20 b-values. For each b-value, synthetic signals are produced from $N_{dir} = 60$ different random diffusion-weighted directions. In addition, signals are also produced for two b-value = 0 measurements in order to capture the signal without the diffusion sensitization. The parameters for the reference signals produced from equations 5.5 and 5.6 are set to be the same ground truth values used for the SMT1 and SMT2 models respectively. For the SMT1 reference signals, multi tensor simulations are produced for N=2 fiber populations crossing at 60º and using the following ground truth parameters: ground truth $\lambda_{\parallel}$ = 1.7 μm^2/ms and $\lambda_{\perp}$ = 0.3 μm^2/ms. For the reference signal decays for the SMT2 model, multi-tensor simulations are produced with the following ground truth parameters: $f = 0.5$ $\lambda_{\parallel}^{i} = \lambda_{\parallel}^{e} =$ 2 μm^2/ms, $\lambda_{\perp}^{i} = 0$ μm^2/ms and $\lambda_{\perp}^{e} = (1-f)\lambda_{\parallel}^{e}$ = 1 μm^2/ms. As a reference for the following experiments, testing the robustness of SMT model fits with different acquisition parameters, the reference mean signals are also computed for simulations with added Rician synthetic noise with a nominal signal-to-noise ratio (SNR) of 38 (note: nominal SNR is defined as the SNR measured at a signal measured at b-value = 0). This SNR level was set according to the typical SNR values of real *in vivo* dMRI acquisitions. Particularly, the exact SNR value of 38 was computed from the *in vivo* dataset described below.

Experiment 2: to test the robustness of SMT1 and SMT2 parameter estimates and microscopic fractional anisotropy estimates, the two models are first fitted to the noise reference signals generated from experiment 1 using the project developed fitting routines for both SMT1 and SMT2 models which were implemented using two non-linear least-squares procedures. To test the fitting robustness to different ground truth parameters, SMT1 simulations and parameter estimates are repeated for different ground truth microscopic fractional anisotropy (from 0 to 1), while SMT2 simulations and parameter estimates are repeated for

different axonal water fraction f ground truth, while keeping the ground truth axial diffusivity set to 2.0 $\mu m^2/ms$ (for the sake of sanity). Note that for the generation of different microscopic anisotropy levels for SMT1 testing, the ground truth axial and radial diffusivities are estimated using the following expressions:

$$\lambda_{\parallel} = MD_i \left(1 + \frac{2\mu FA_{gt}}{\sqrt{3 - 2\mu FA_{gt}{}^2}}\right) \tag{5.8}$$

$$\lambda_{\perp} = \frac{3MD_i - \lambda_{\parallel}}{2} \tag{5.9}$$

where MD_i is the mean diffusivity of each individual compartment with was assumed to have a constant value of 0.8 $\mu m^2/ms$, and μFA_{gt} is the ground truth microscopic fractional anisotropy. Relative to SMT2 μFA ground truth values, these are computed from the ground truth f values using equation 5.4. All simulations of experiment 2 were also repeated for a diffusion acquisition protocol with a smaller number of b-values (b-value= 100, 1000, 2000 s/mm^2). Note that to compute the median and interquartile ranges of the different parameters at different ground truth values, the signals of each diffusion protocols are simulated 20 times.

Experiment 3: to further test the relationship between SMT μFA estimates and the number of acquired b-values, simulations are repeated for diffusion acquisition protocols with increasing number of b-values (from 2 non-zero b-values to 20 non-zero b-values). For each b-value, signals are generated for 60 directions with a nominal SNR=38. For the sake of simplicity these simulations are performed for a ground truth μFA of 0.80 $\mu m^2/ms$ for SMT1 evaluation (corresponding to ground truth parameters $\lambda_{\parallel}$ = 1.7 $\mu m^2/ms$,and $\lambda_{\perp}$ = 0.3 $\mu m^2/ms$) and for a ground truth μFA of 0.73 $\mu m^2/ms$ for SMT2 evaluation (corresponding to ground truth parameters $\lambda_{\parallel}$=2.0 $\mu m^2/ms$, $\lambda_{\perp}^{i} = 0$ $\mu m^2/ms$, $\lambda_{\perp}^{e}$ = 1.0 $\mu m^2/ms$ and $f = 0.5$). For a better comparison with the results of experiment 4, μFA median

and interquartile ranges are plotted as function of the total number of directions for all b-value of each simulated protocol. To quantify the improvement of μFA estimation precision, the standard deviation of μFA estimates for each diffusion protocol are plotted as a function of the protocols' total number of directions. Note that to compute the median, interquartile ranges and standard deviations the signals of each diffusion protocols are simulated 20 times.

Experiment 4: to test the relationship between SMT μFA estimates and the number of gradient directions for each acquired b-value, the simulations of experiment 3 are repeated for diffusion protocols with a constant number of non-zero b-value acquisitions (b-value = 1000, 2000 s/mm^2) but increasing number of gradient directions per shell.

Experiment 5: to test the model when the assumptions for each SMT model are not met, different and fixed values from the two SMT model assumptions are used in the simulations. For the SMT1, an extracellular component with a different diffusivity is added, with $\lambda_{\parallel}$ = 2.25 μm^2/ms , $\lambda_{\perp}^{e}$ = 1.1 μm^2/ms and f = 0.49. For the SMT2, the radial diffusivity parameter from the extracellular compartment was fixed to 0.45 μm^2/ms independently to the tortuosity relationship ($\lambda_{\perp}^{e} = (1 - f)\,\lambda_{\parallel}^{e}$) while the axonal volume fraction was changed from 0 to 1 and the axial diffusivities from both intracellular and extracellular compartments were fixed to 2.25 μm^2/ms.

5.2.2 *In vivo* data

Implemented SMT models were applied to open source dMRI data which was previously acquired at the Center of Functionally Integrative Neuroscience (CFIN), Aarhus, Denmark. This dataset was acquired in one healthy human volunteer using a Siemens Trio 3 T equipped with a 32-channel head coil and a double spin echo DW EPI sequence. DWI data was recorded at b=0 ms/μm^2, and

along 33 directions at b-values from 0.2–3 ms/μm^2 in steps of 0.2 ms/μm^2. Imaging parameters were TR=7200 ms, TE=116 ms, TI=2100 ms, 19 consecutive slices were acquired at isotropic resolution of 2.5 mm with matrix size 96×96 (Hansen et. al, 2016).

To corroborate the results observed from different SMT1 and SMT2 parametric brain maps (axial diffusivity, radial diffusivity, and microscopic fractional anisotropy for SMT1, and intrinsic axial diffusivity, water volume fraction, and microscopic fractional anisotropy for SMT2), histograms are plotted for an axial slice, presenting the distribution of values all throughout the brain slice.

5.3 Results

5.3.1 Simulations

Experiment 1: Figure 12 shows the spherical mean signals for the SMT1 model (in blue) and its respective reference signal (red lines) computed from Dipy's multi-tensor simulations. The upper and lower panels show the results of the signals and logarithmic signals as a function of the b-value, respectively. In the left panels reference signals are generated noise free, while in the right panels reference signals are corrupted by Rician noise. Figure 13 shows the analogous Figure for the SMT2 model.

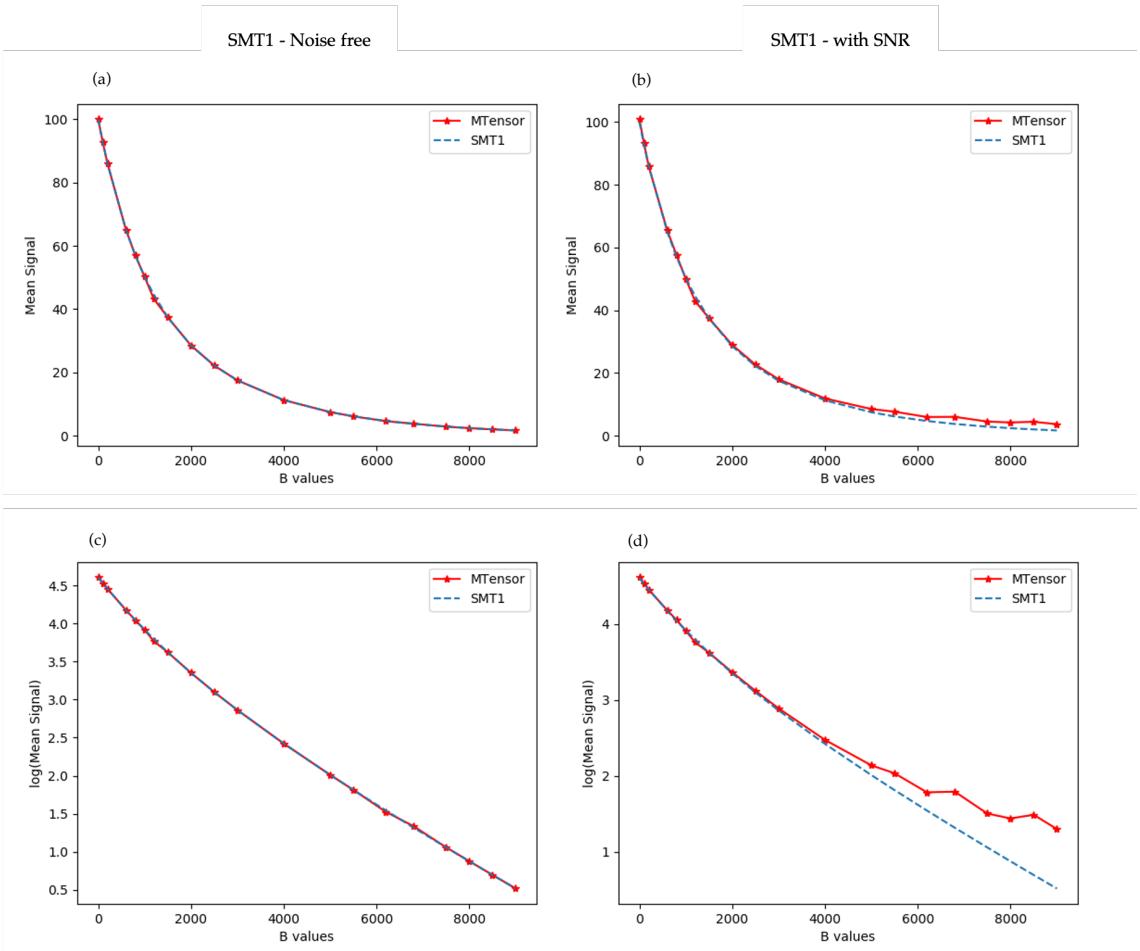

Figure 12 – Spherical means of the signal computed through the SMT1 model against increasing b value. The reference line is the Dipy's function responsible for a mean signal creation. The first column (panels (a) and (c)) corresponds to the noise free mean signal simulations while the second column (panels (b) and (d)) corresponds to the mean signal simulations with an SNR value of 38, nominal SNR the noise free mean signal simulations.

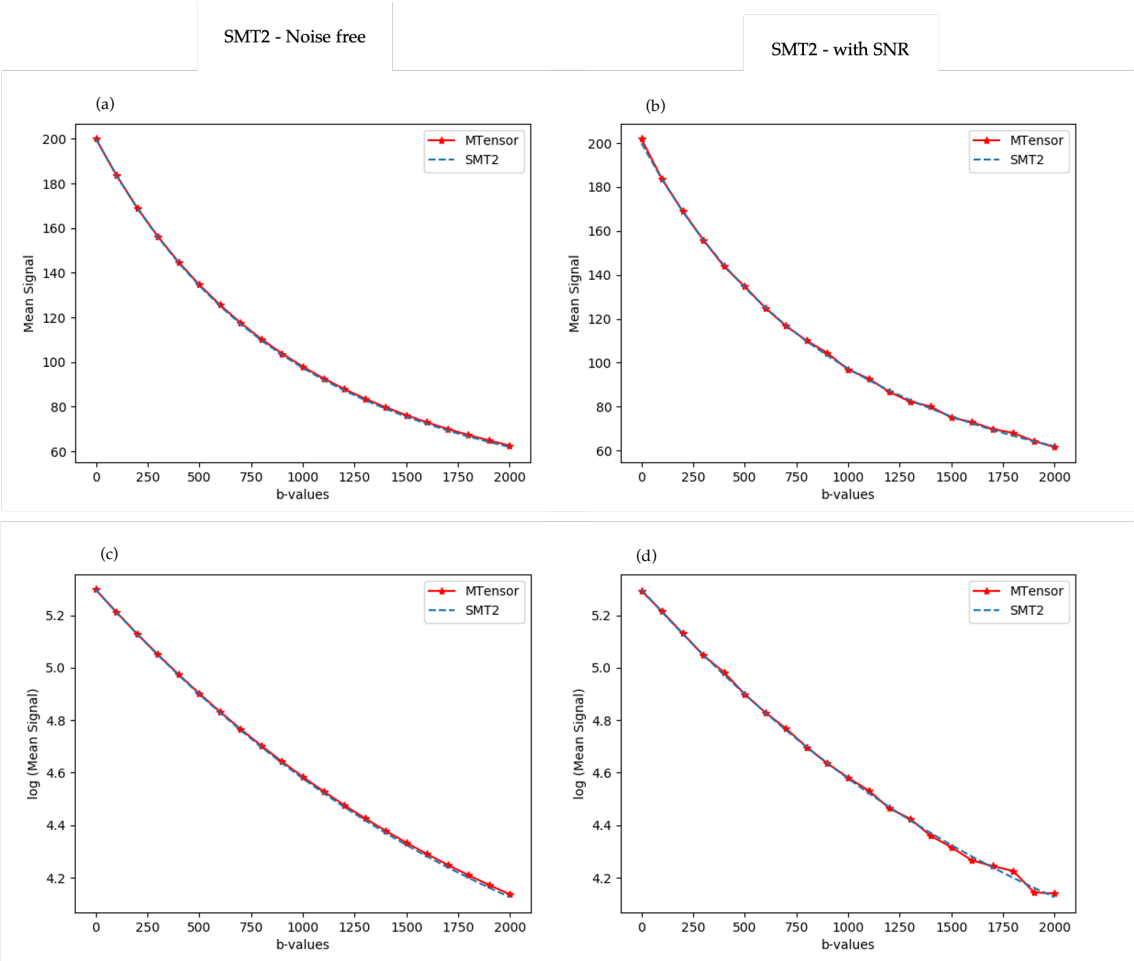

Figure 13 - Spherical means of the signal computed through the SMT2 model against increasing b value. The reference line is the Dipy's function responsible for a mean signal creation. The first column (panels (a) and (c)) corresponds to the mean signal simulations with an SNR value of 38, nominal SNR while the second column (panels (b) and (d)) corresponds to the noise free mean signal simulations.

As both Figures above show, the signals predicted by the SMT models match their reference lines when these are computed without the influence of noise.

Experiment 2: SMT parameter estimates using the least square fitting routines are shown in Figures 14 and 15.

Figure 14 shows the axial and radial diffusivities for the SMT1 model as a function of the different ground truth microscopic fractional anisotropy values.

Ground truth axial and radial diffusivities are plotted by the blue lines. For a first assessment of the relationship of the model fit robustness and the number of simulated signals, these results are plotted for signals generated for the lower and

the higher number of b-values (left and right panels of Figure 14). The axial and radial diffusivities estimations computed for a signal generated with lower number of b-values give rise to a larger interquartile rage but similar median values when compared to the results obtained for the signals generated with higher number of b-values. Note that the mean signals are close to their ground truth values, particularly for high ground truth microscopic anisotropy values.

As expected from equations 5.8, axial diffusivity estimates increase as the ground truth microscopic fractional anisotropy values rise. On the contrary, radial diffusivity estimates decrease as the ground truth values get closer to its maximum value (as expected from equation 5.9).

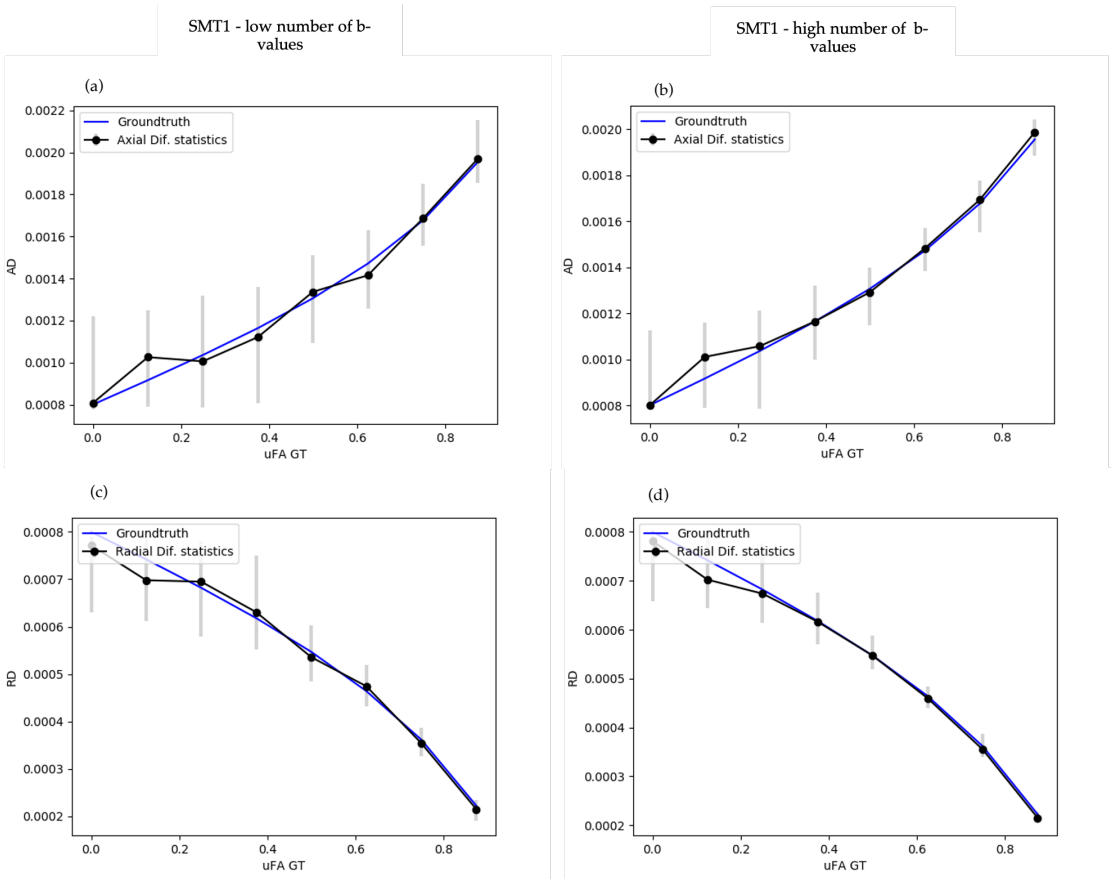

Figure 14 - The median and interquartile ranges for the SMT1 axial and radial diffusivities estimates plotted for varying μFA ground truth values. Axial diffusivity is plotted in panels (a) and (b) while radial diffusivity is plotted in panels (c) and (d). The first column, panels (a) and (c), represent the SMT1 parameter for a signal simulated with low number of b values whereas the second column, panels (b) and (d), represent the same SMT1 parameters but for a signal simulated with a high number of b values.

The median and inter-quartile ranges for SMT2 parameter estimates are represented in the panels of Figure 15. As for Figure 14, the intrinsic axial diffusivity and volume water fraction were plotted against the ground truth microscopic fractional anisotropy values (ranging from 0 to 1), panels (b) and (d), and computed for a signal with lower number of b-values, panels (a) and (c).

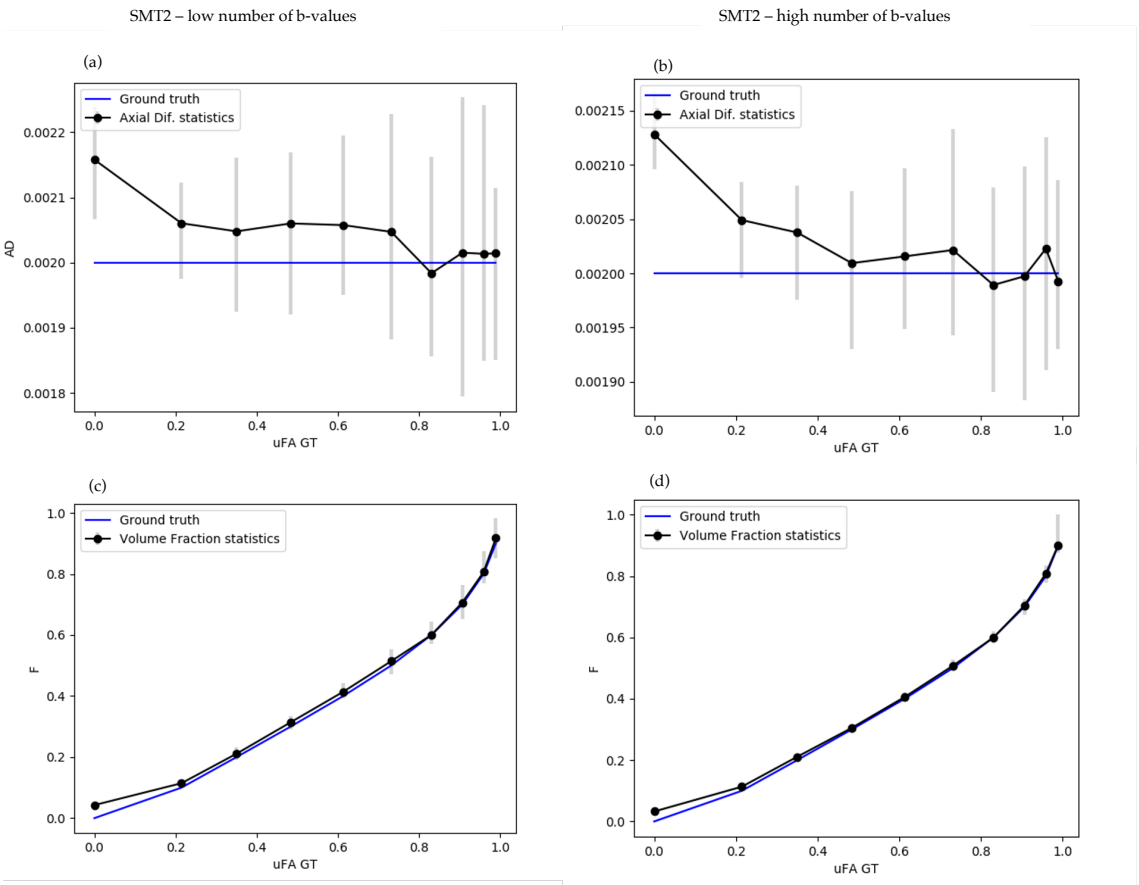

Figure 15 - The intrinsic axial diffusivity and axonal water fraction, estimates from the SMT2 model, are plotted for varying μFA ground truth values. Intrinsic axial diffusivity is plotted in panels (a) and (b) while axonal water fraction is plotted in panels (c) and (d). The first column, panels (a) and (c), represent the SMT2 diffusion factors for a signal simulated with low number of b values whereas the second column, panels (b) and (d), represent the same diffusion factors but for a signal simulated with a high number of b values.

Note that, since the simulations for Figure 15 were generated for a fixed intrinsic axial diffusivity of 2 $\mu m^2/ms$ and since the μFA estimates from SMT2 only directly hinges on the axonal water fraction, only the axonal water volume fraction estimates show largely increase as a function of the ground truth microscopic fractional anisotropy.

From the SMT1 and SMT2 parameter estimates, microscopic fractional anisotropy estimates can be estimated using equations 5.2 and 5.4, respectively. Panel (a) and (c) of Figure 16 represent the microscopic fractional anisotropy estimates for the SMT1 model and panels (b) and (d) represent the microscopic fractional anisotropy estimates for the SMT2 model. As for the different SMT1 and SMT2 parameter plots, both μFA estimations were made also using the synthetic signals generated with lower and higher number of b values.

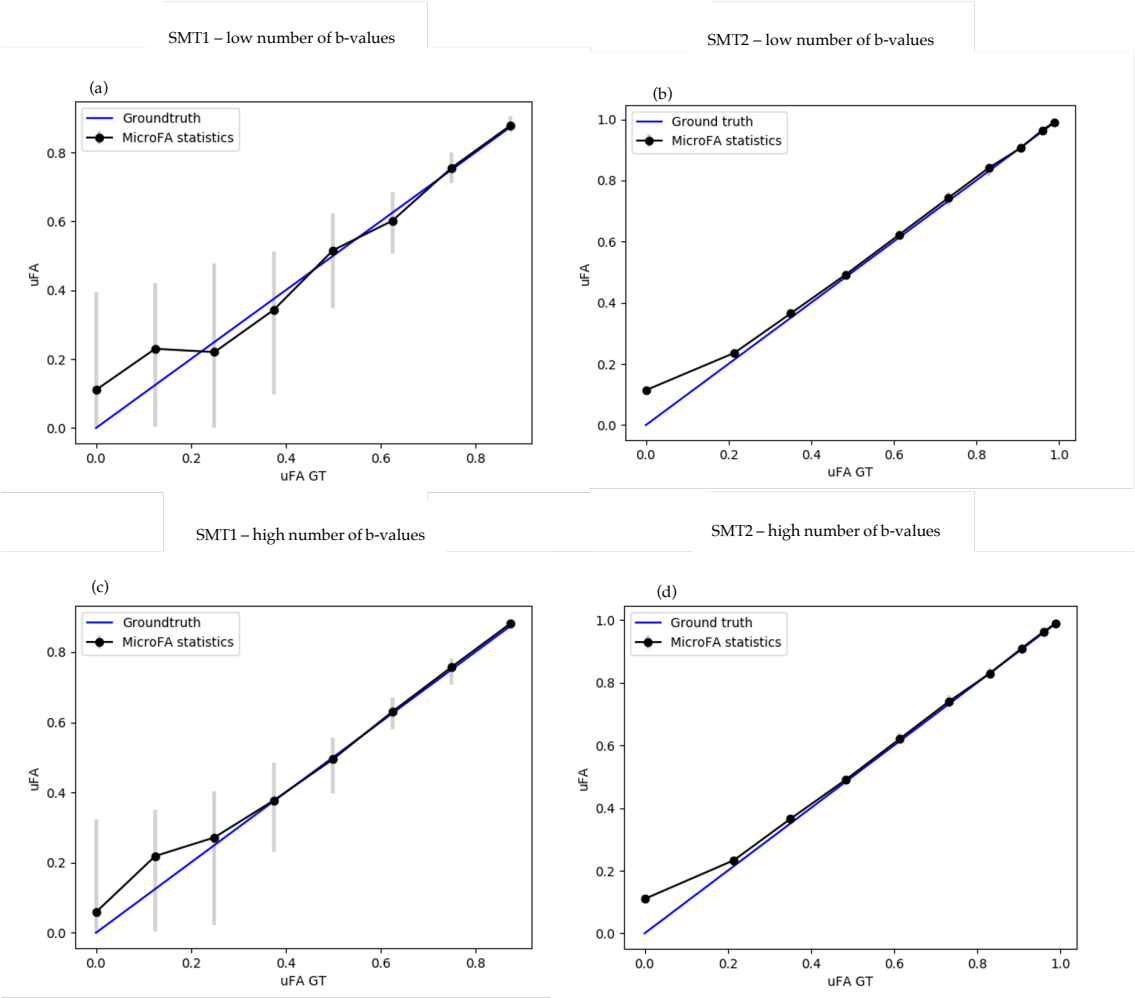

Figure 16 - The micro fractional anisotropy estimates from both SMT models are plotted for varying μFA ground truth values. Panels (a) and (c) represent the μFA estimates through the SMT1 model while uFA from SMT2 is represented in panels (b) and (d). The μFA estimates for a signal simulated with low number of b values can be found in the upper panels while the lower panels represent the same diffusion measurement but for a signal simulated with a high number of b values.

On all panels of Figure 16, μFA estimates are shown to be overestimated for the lower ground truth microscopic fractional anisotropy values. μFA estimates are also noisier for the signals generated for a lower number of b-values.

Experiment 3 and 4: In these experiments, the benefits of increasing the number of acquired b-values (experiment 3) or number of directions (experiment 4) are explored.

The effect of increasing the number of b-values for a fixed number of 60 gradient directions is shown in Figure 17, while the effect of increasing the number of directions for fixed number of two non-zero b-values are shown in Figure 18. Both experiments show that increasing the number of simulated signals does not do significant changes to the median values of the model parameter estimates but improves their precision.

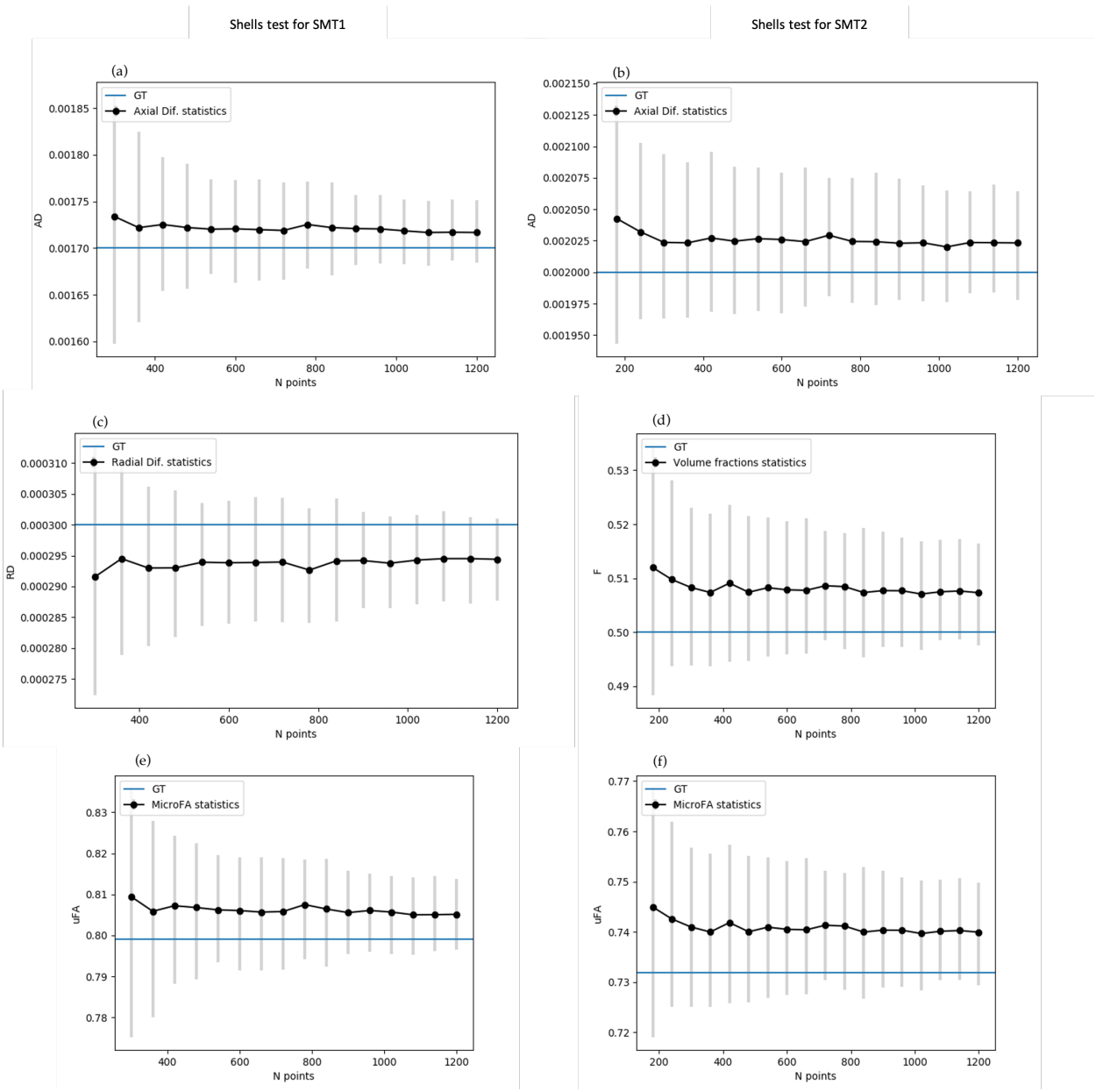

Figure 17– Testing the robustness increase of the parameters of both SMT1 and SMT2 models as a function of the increase number fitted signals by increasing the number of b-values

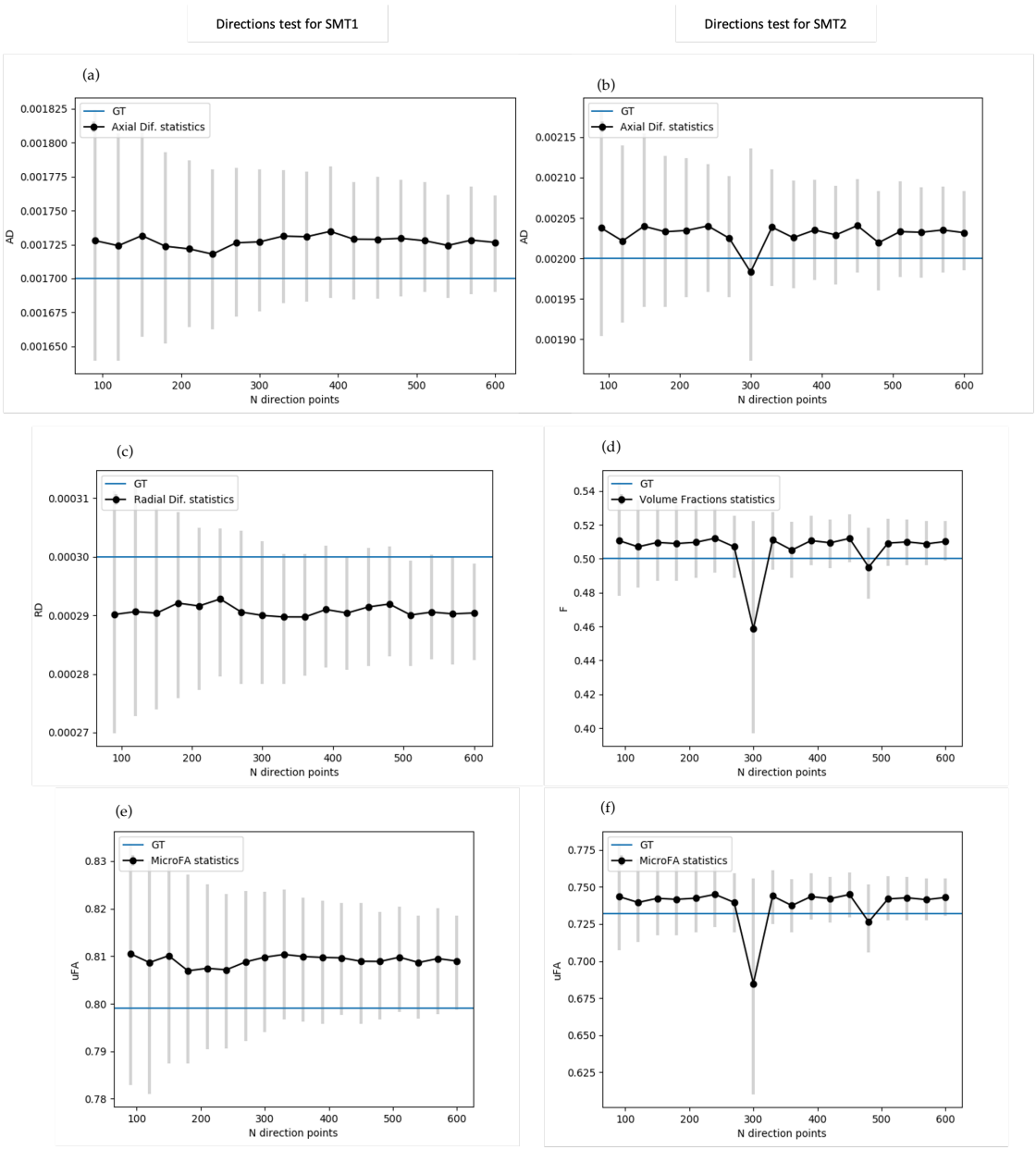

Figure 18 - Testing the robustness increase of the parameters of both SMT1 and SMT2 models as a function of the increase number fitted signals by increasing the number gradient directions for a fixed number of b-values.

Figures 19 and 20 show the standard deviation of the measures as a function of the $1 / \sqrt{(number\ of\ points)}$ for both experiments. These Figures show similar linear relationships as indicated by the linear regression.

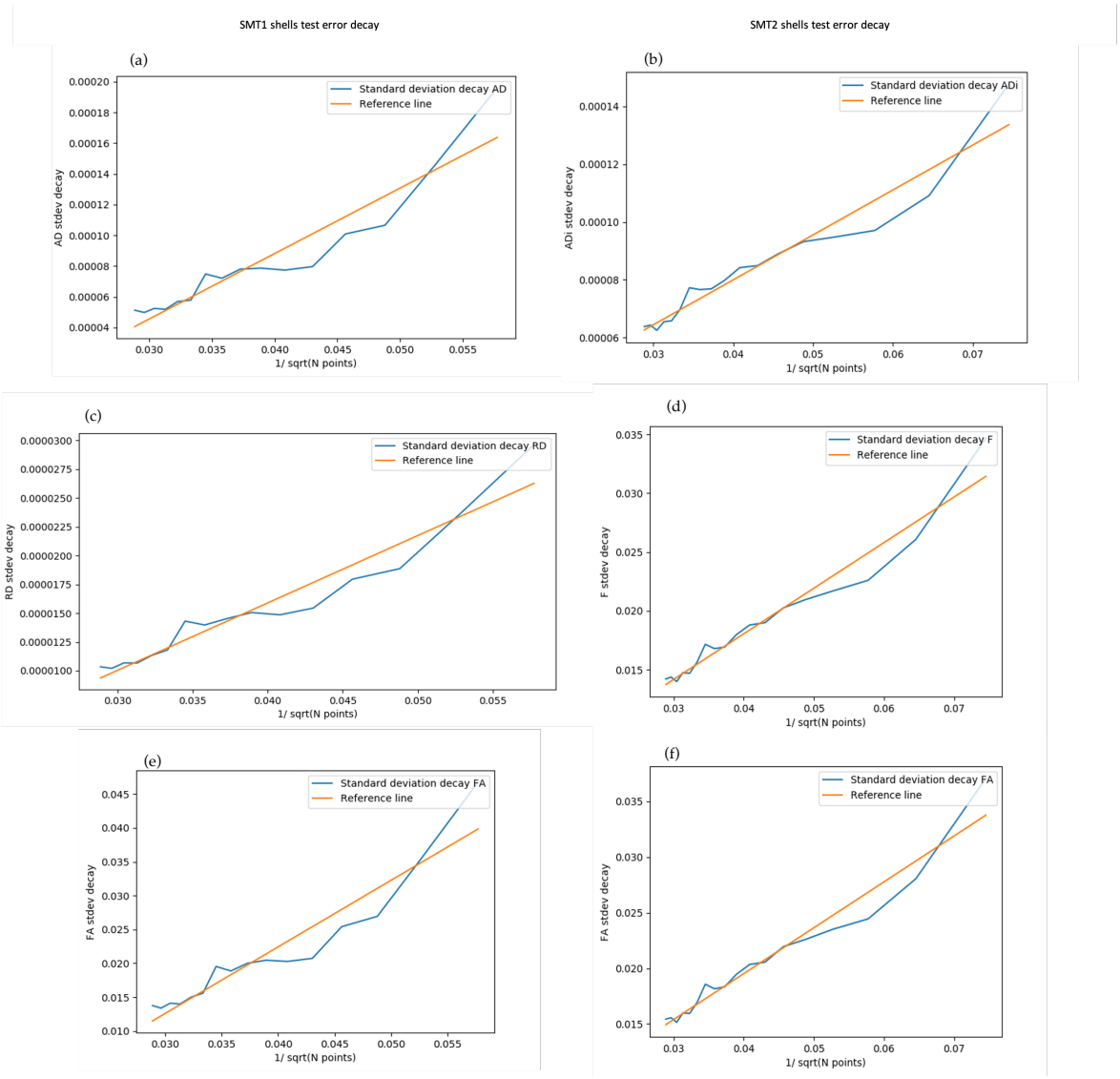

Figure 19 - Standard deviation decays of diffusion parameters and microscopic fractional anisotropy estimated from both SMT1 and SMT2 models for a signal protocol with increasing b-values. The standard deviation decay is plotted against the $^{1}/_{\sqrt{N}}$, where N is the total number of points in the signals generated for all gradient directions and b-values.

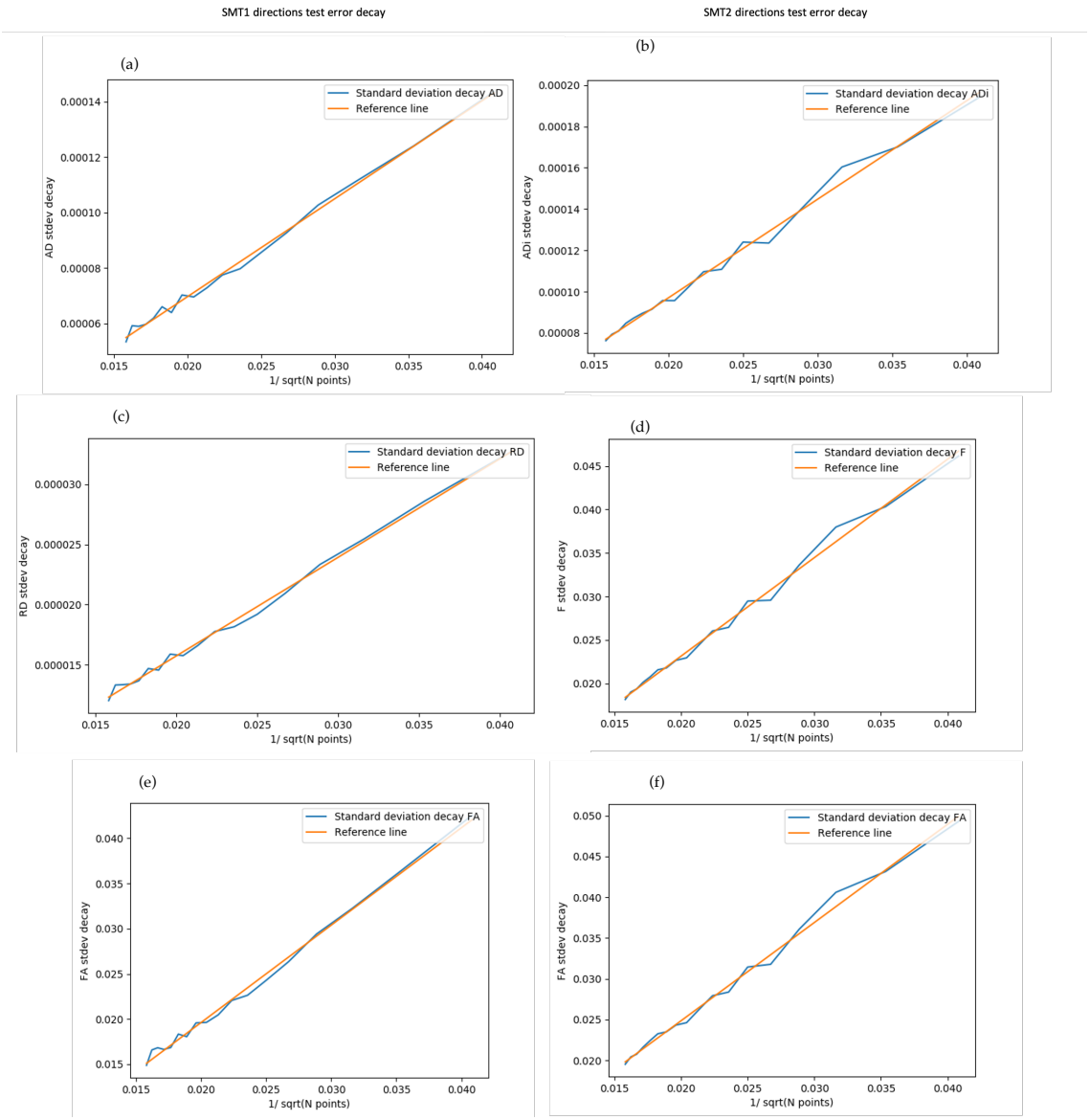

Figure 20 - Standard deviation decays of diffusion parameters and microscopic fractional anisotropy estimated from both SMT1 and SMT2 models for a signal protocol with increasing gradient directions but fixed number of non-zero b-values. The standard deviation decay is plotted against the $^{1}/_{\sqrt{N}}$, where N is the total number of points in the signals generated for all gradient directions and b-values.

For all panels from Figures 19 and 20 the smaller the inverse of the square root of the number of points in a signal, the smaller the deviations from the true value estimated. Panels (a), (c), and (e) correspond to the SMT1 model parameters axial diffusivity, radial diffusivity and microscopic fractional anisotropy while panels (b), (d) and (f) of both Figures 19 and 20 correspond to the SMT2

model parameters intrinsic axial diffusivity, water volume fraction and microscopic fractional anisotropy respectively. As seen, the standard deviation alterations with the inverse of the square root of the number of points for experiment 3 are similar to those in experiment 4.

Experiment 5: So far, the models were tested for assumptions in which the models hold. However, the diffusion in biological systems may not be in accordance with the model assumptions. Therefore, experiment 5 was performed to test the robustness of SMT model estimates in cases that their assumptions are not met.

For the SMT1 model testing, an extracellular component was added. As soon as this extracellular component is introduced with different diffusivities than the intra-cellular compartment, the axial and radial diffusivities of SMT1 become unreliable making the microscopic fractional anisotropy estimate inaccurate, as shown in the first column of Figure 21.

For the SMT2 model testing, synthetic signals were produced with parameters that do not follow the tortuosity assumption. With simulations performed for these ground truth values, the SMT2 model misestimates the microscopic fractional anisotropy. This effect is shown in the second column of Figure 21.

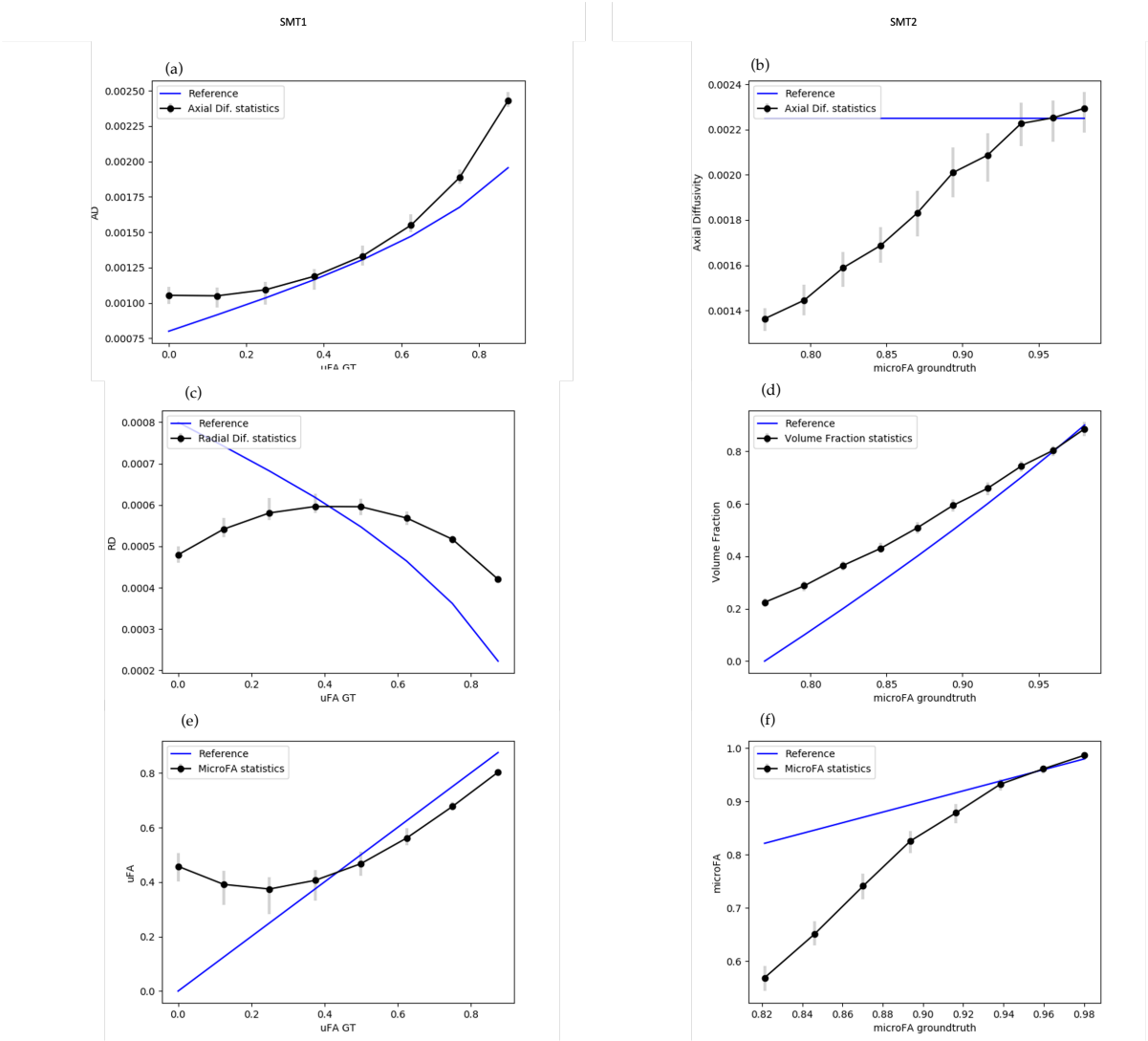

Figure 21 - Out of assumptions test for the spherical mean technique models, SMT1 and SMT2.

5.3.2 *In vivo* data

All diffusion parameters of SMT1 and SMT2 were plotted for three axial brain slices (slice 6 in the first panel lines, slice 12 in the middle panel lines and slice 18 in the final panel lines of Figure 22 and Figure 23).

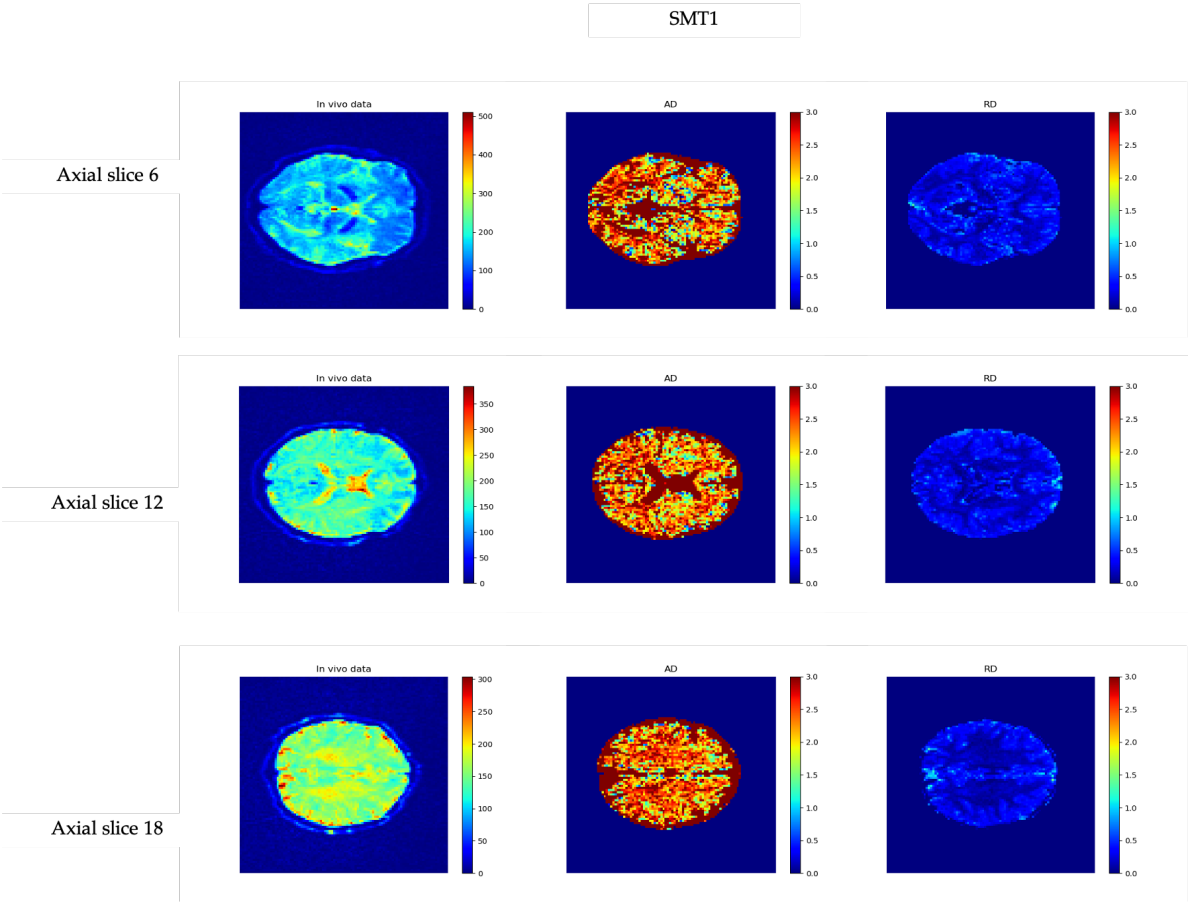

Figure 22 - Diffusion parameters from the SMT1 model, axial and radial diffusivities, are plotted as brain maps for three axial slices, the 6th, the 12th and the 18th brain slices. The *in vivo* data is also plotted for the same three axial slices as a reference of non-weighted diffusion imaging (first column of panels).

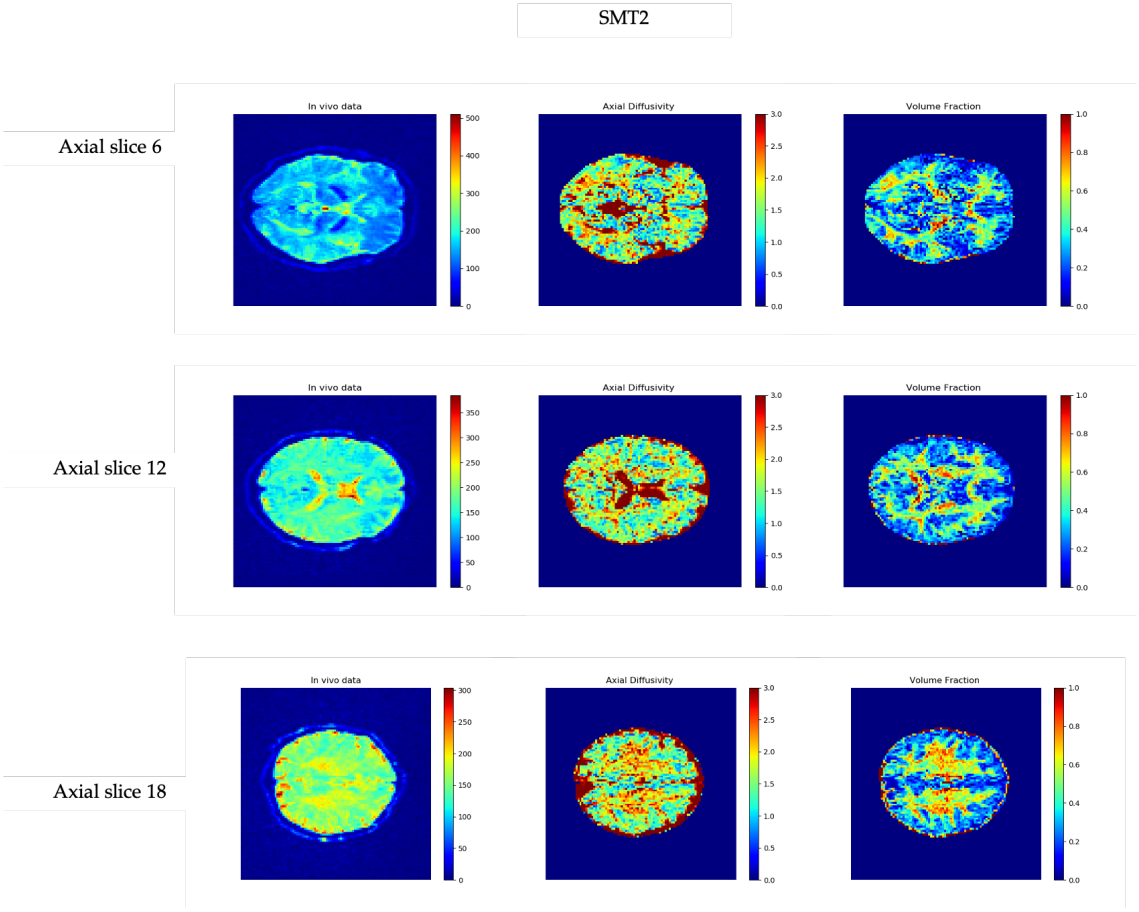

Figure 23 - Diffusion parameters from the SMT2 model, intrinsic axial diffusivity and axonal water fraction, are plotted as brain maps for three axial slices, the 6th, the 12th and the 18th brain slices. The *in vivo* data is also plotted for the same three axial slices as a reference of non-weighted diffusion imaging (first column of panels).

Both spherical mean technique models show that the axial diffusivity estimates (second column from both Figure 22 and Figure 23) are higher in brain white matter than in grey matter. The contrast between white and grey matter is more noticeable for the axial diffusivities of the 2-compartment spherical technique mean model. On the contrary, the radial diffusivity parameter of the SMT1 model (third column of Figure 22) has low estimates and poor contrast between the white matter and grey matter of the brain. Volume fraction estimates measured from the SMT2 model are higher in the corpus callosum and internal capsule compared to the other white matter regions and close to 0 in grey matter regions (third column of Figure 23).

Microscopic fractional anisotropy estimated using the SMT1 model (Figure 24 shows high values in both white and grey matter). The SMT2's *μFA* maps show a similar contrast to the volume fraction maps. If the axial diffusivity estimates are larger or smaller than predicted the microscopic fractional anisotropy estimates can be either overestimated or underestimated (Henriques et. al, 2018).

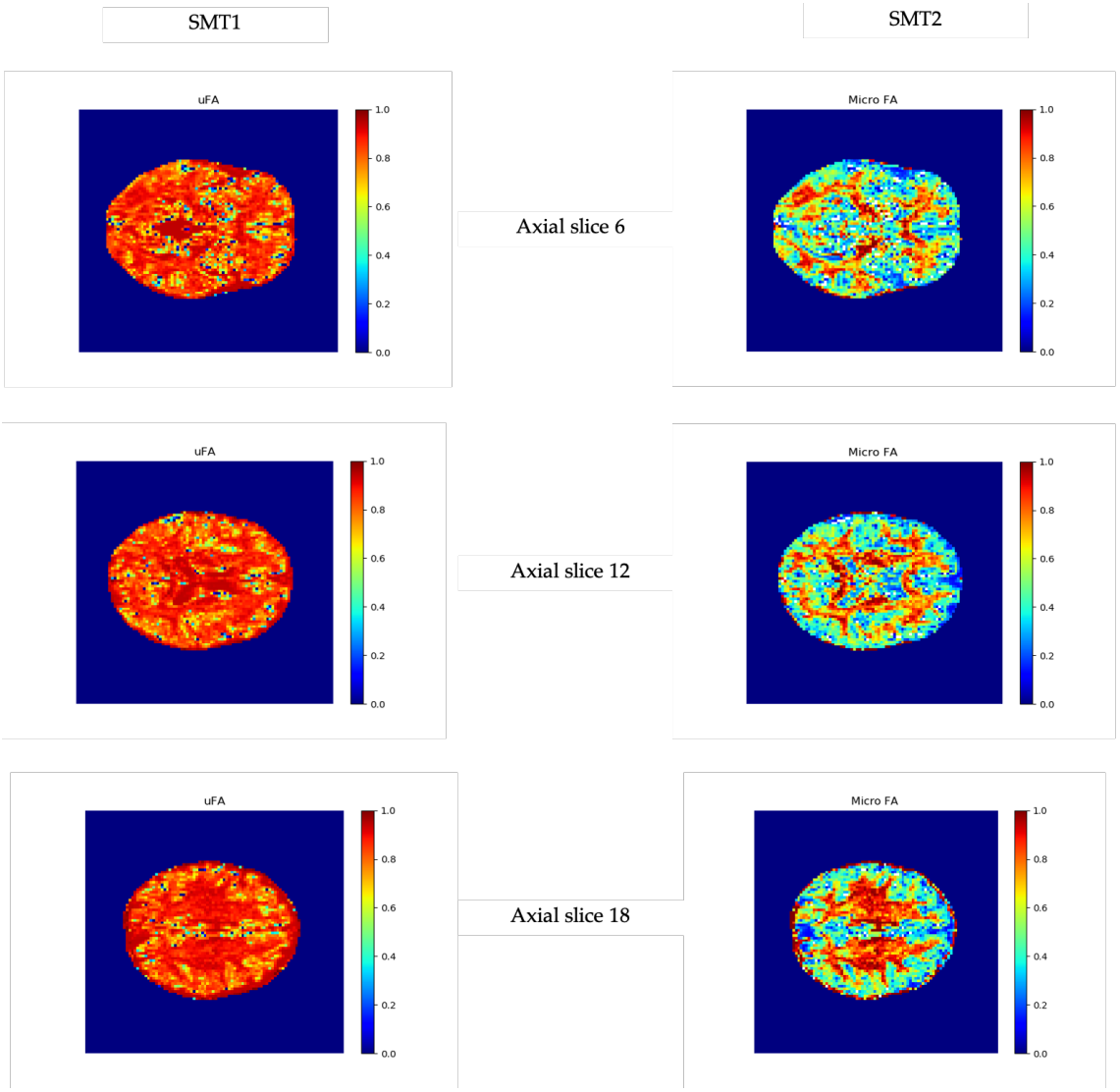

Figure 24 - Microscopic fractional anisotropy estimated through both Spherical Mean Technique models is plotted as brain maps for three axial slices, the same ones used for the other SMT1 and SMT2 parameter estimates (Figure 22 and 23).

For a better understanding of the parameters' estimates, Figure 25 shows the histograms of the SMT1 and SMT2 estimates for one brain axial slices - the 12th axial slice (corresponding to the slice represented in the middle panel of Figures 22, 23 and 24). According to the parameters' brain maps referenced before:

- the axial diffusivity estimates for both models are high throughout the brain (panels (a), (d), (g), (j), (m) and (p) of Figure 25) - note that, for a reference, the value of the diffusion of free water is 3 $\mu m^2/ms$;
- a considerable number of radial diffusivity estimates are low, between 0 and 0.5 $\mu m^2/ms$ (panels (b), (h) and (n) of Figure 25);
- the volume fraction estimates have a reasonable number of estimates close to one (panel (e), (k) and (q) of Figure 25);
- as for the microscopic fractional anisotropy, for a SMT1 model its estimates are closer to one which are consistent with the color scheme of the brain maps (panels (c), (i) and (o) and for the SMT2 model we can see that its estimates depend heavily on the volume fraction estimates (panels (f), (l) and (r) of Figure 25).

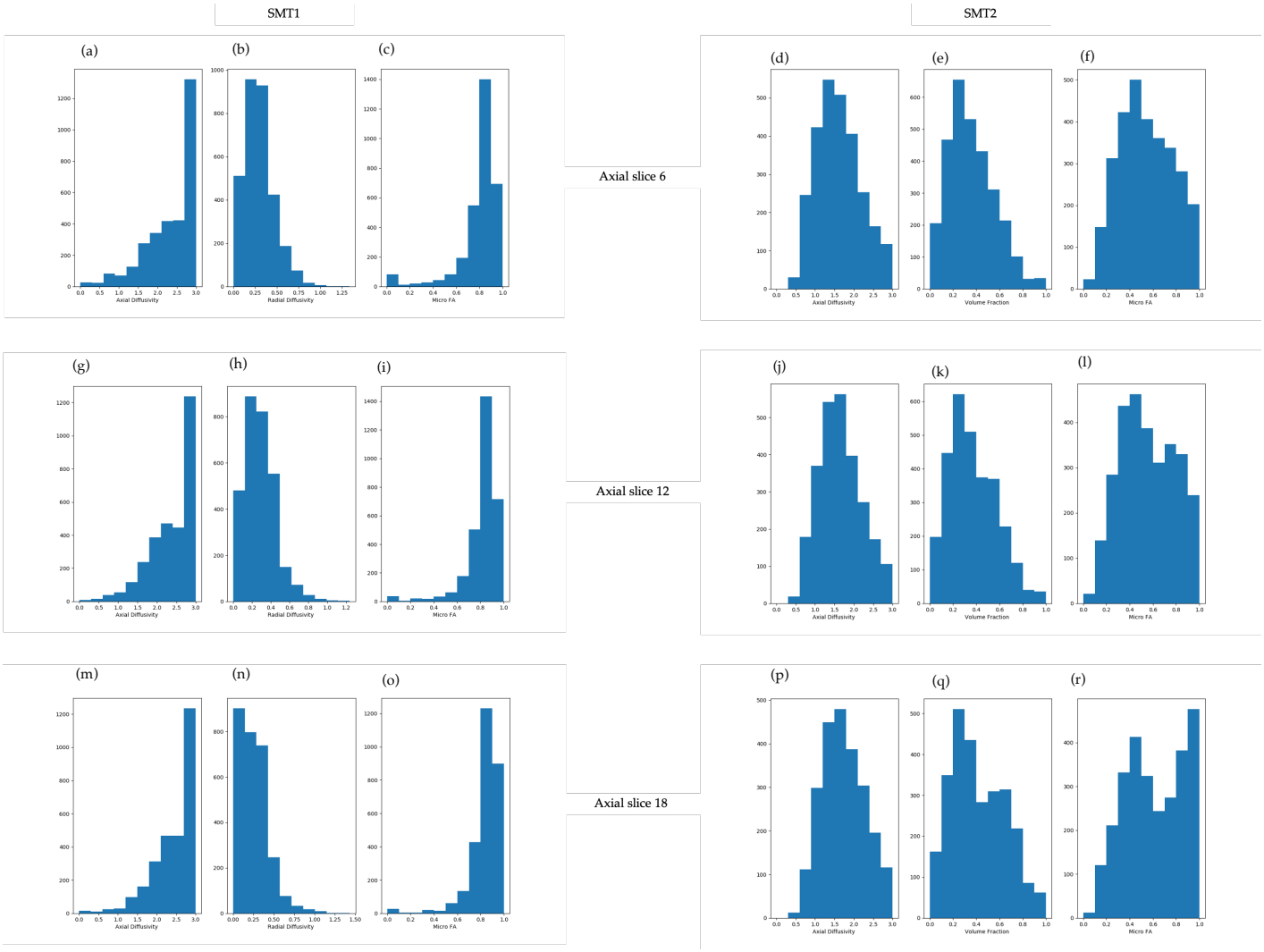

Figure 25 - Histogram plots of all diffusion parameters needed for each model to compute the micro fractional anisotropy measurement, with this latter diffusion factor represented as well. The same three brain slices are used to corroborate the brain maps obtained.

5.4 Discussion

The results of the implementation of the SMT models performed on this these are presented on this chapter. The T_2- normalised diffusion signals acquired with uniformly sampled gradient directions for each b-value separately are averaged to compute the spherical mean signal used to fit the diffusion parameters and acquire the micro fractional anisotropy estimates. Synthetic noise was also incorporated in all SMT simulations with a typical nominal signal-to-noise ratio (SNR) of 38.

5.4.1 SMT1

Single voxel simulations were first made to test the models' implementation. To ensure that the SMT1 model is implemented correctly, its mean signal predictions were compared to mean signals independently computed from the Dipy multi-tensor simulations which are reconstructed based on a single compartmental type (equation 5.5). Plotting these mean signals and its logarithmic representations compared to the noise-free and noise corrupted reference signals, it is possible to determine the resemblance between them (Figure 12). The SMT1 expected signal decays present only some deviations for the noisy reference signals as expected, particularly for the higher b-values.

The SMT1 parameters fitted to the noisy signals and plotted, against increasing microscopic fractional anisotropy ground truth values (Figure 14). The axial and radial diffusivities of the SMT1 model demonstrate opposite trends, as expected for the equations 5.8 and 5.9 - while axial diffusivity presents higher values with the increasing ground truth values, radial diffusivity decreases. In order to evaluate the robustness of SMT1 estimates on different acquisition, the SMT1 model was fitted to signals generated with different number of b-values.

Although fitting the SMT1 with smaller number of b-values seems to produce estimates with lower precision, their accuracy is shown to be less effected. An exception from this, happens for low ground truth μFA estimates, in which noise seems to overestimate μFA. This overestimation of μFA for low μFA ground truth values is analogous to the well documented repulsion effect on the diffusion anisotropy estimation in which noise in almost isotropic systems introduces artificial degrees of anisotropy (Pierpaoli & Basser, 1996).

More detailed exploration of the relationship between parameter estimation and the number of used gradient directions and b-values were performed on experiments 3 and 4. Increasing both the number of b-values and gradient directions shows to narrow the μFA error bars. To further assess the dependency between the parameters' estimation robustness and the number of signals generated for SMT1 parameters' estimations, the standard deviation of SMT1 estimates were plotted against the inverse of the square root of the number of signals generated. Results show that the smaller the inverse of the square root of the number of points in a signal, the smaller the deviations from the true values estimated. These profiles for an increasing number of b-values seem to be identical to the profiles for increasing the number of directions. Therefore, the actual factor for the improvement of the robustness of SMT1 parameter estimates was shown to be just an increase of the number of points in the signals used on the fit, independently if this increase is done on the number of b-values or gradient directions used. The higher the number of points in a signal the better is the precision of the parameter estimations.

To test the SMT1 model when the assumptions are not met, an extracellular component with different diffusivity was added. As this technique is used for one type of tissue compartment, axial and radial diffusivity estimates become untrustworthy and μFA estimates inaccurate. The SMT1 model was then tested on a brain dataset acquired *in vivo*. SMT1 axial diffusivity estimates extracted from these dataset present higher contrasted values in white matter than in grey matter, while radial diffusivity estimates are low throughout the brain. As predicted from the simulations, SMT1 estimates high μFA values through the brain due to the SMT1 high axial diffusivity estimates and the low radial diffusivity

estimates. These observations were confirmed from the histograms made from the parametric maps of one brain slice with slow high axial diffusivity and μFA estimates and low radial diffusivity estimates.

5.4.2 SMT2

To take into account microstructural differences between intracellular and extracellular mediums, the spherical mean technique was expanded to a two-compartments model assuming that diffusion coefficients from extracellular and intracellular mediums are correlated (Kaden et al., 2016b).

Simulations of a signal with these two different mediums were performed. Averaging these signals, the reference spherical mean signals are computed and compared with the mean signal expected from the SMT2 model. Since this reference spherical mean signal was produced according to the assumption of the SMT2 model, these are expected to match the mean signals predicted by the SMT2 model. Here we verified that there were no differences between the SMT2 signal prediction and reference signals, confirming that the SMT2 model was correctly implemented (Figure 13).

The next step was to assess the robustness of SMT2 parameter estimation using signals generated for a low and high number of b-values and corrupted with synthetic noise (SNR=38). Since intracellular and extracellular mediums are assumed to be related through its diffusion coefficients, the estimated parameters of the SMT2 model are the intrinsic axial diffusivity and the water volume fraction. Again, these parameters were estimated for varying ground truth microscopic fractional anisotropy values, while the ground truth axial diffusivity estimates were set to a constant (for the sake of simplicity). The SMT2 correctly predicted higher volume fraction estimates for higher ground truth μFA values, due to direct dependance of these two diffusion factors given by equation 5.4. With the use of this equation, μFA estimates can be estimated from the SMT2 axonal

volume fraction estimation. These estimations hover their ground truth values, showing that μFA estimates can be precisely and accurately estimated when signals are generated in accordance with the models' assumptions. A minor miscalculation was shown for the ground truth value of 0, due to μFA estimates being noisier for signals generated for a lower number of b-values.

As for the SMT1 model, SMT2 parameters estimates presents a higher accuracy when signals are generated for a higher number of b-values.

By assessing the influence of the increase of the number of b-values and the increase in number of gradient directions, separately, results show that both equally lower the estimation errors, making the parameter estimates more reliable. Although, in general, increasing the number of signals (either by increasing the number of b-values or increasing the number of gradient directions) shows to decrease the error standard deviation as a function of the square root of the number of points, some deviations from this relationship were observed for some set of increased number of gradient directions. This could be explained by imprecisions on the generation of evenly oriented directions, particularly, for large number of directions the algorithm for direction sampling struggled to properly converge to a stable solution. The SMT2 parameter estimates were shown to be more sensitive to this direction sampling imprecisions than the SMT1 model.

To test the SMT2 model when its assumptions are not met, synthetic signals were produced for parameters that did not follow the tortuosity model. In this case, results show that the two-compartment spherical technique model fails in characterizing both diffusion parameters and microscopic fractional anisotropy.

Applying the two compartments SMT model to the *in vivo* datasets, its parameter estimates were shown to provide higher contrast between white and grey matter brain regions than the SMT1 model. Therefore, SMT2 may provide a better characterization of white matter regional differences than the SMT1 model. Regarding SMT2 microscopic anisotropy estimates, these may not provide different information from the axonal water fraction estimates, since SMT2 microscopic anisotropy estimates only depend on these estimates.

6

Implementing the Fiber Ball Imaging technique

6.1 Introduction

Fiber Ball Imaging (FBI) is a model designed to estimate the tissue axonal water fraction from spherical mean signals and assuming a two non-exchanging compartment model (Jensen et. al, 2016, McKinnon et al., 2018). Compared to the two compartmental spherical mean technique (SMT2), the Fiber Ball Imaging does not assume any correlation between the diffusion coefficients of the extra-cellular and intracellular mediums. Instead, it assumes that the extracellular medium has higher diffusivities than intra-cellular spaces and thus it can be eliminated by applying high intensity diffusion gradients.

Assuming that the extra-axonal water contribution is suppressed when the diffusion weighting b-value is sufficiently large, the FBI model estimates the axonal water fraction (AWF) from the spherical mean signal normalized by the b-value signal $\bar{E}$, the b-value and a fixed value for the intra-axonal diffusivity $\lambda_{||}^{i}$:

$$AWF = 2\sqrt{\frac{b\lambda_{||}^{i}}{\pi}}\,\bar{E} \tag{6.1}$$

For the derivation of the equation above, the intrinsic radial diffusivity is assumed to be zero ($\lambda_{\perp}^{i} = 0$). In this work, we fixed the intra axial diffusivity $\lambda_{||}^{i}$ to a value of $2.25\mu m^2/ms$ according to McKinnon et al. (2018). Note that for higher b-values this equation allows the estimation of the volume fraction even though there is an error due to the residual extra-cellular signal contribution in the axonal water fraction estimation in high b-values, this error is expected to decrease as the maximum b-value increases. Note that, unlike the SMT model parameters previously explored, the estimation of *AWF* can be obtained from a single mean signal value for a single high b-value.

In this study, an adaption of the FBI model to estimate the extra-cellular diffusivity was also tested. After having estimated the *AWF* from the high b-value signals and the fixed $\lambda_{||}^{i}$ value, $\lambda_{||}^{e}$ and $\lambda_{\perp}^{e}$ can be estimated by fitting diffusion-weighted signals (including for low b-values) using the following expression:

$$\bar{E}_{SM}(b) = f\frac{\sqrt{\pi}\,erf\left(\sqrt{b\lambda_{\parallel}^{i}}\right)}{2\sqrt{b\lambda_{\parallel}^{i}}} + (1-f)e^{-b\lambda_{\perp}^{e}}\frac{\sqrt{\pi}\,erf\left(\sqrt{b\left(\lambda_{\parallel}^{e}-\lambda_{\perp}^{e}\right)}\right)}{2\sqrt{b\left(\lambda_{\parallel}^{e}-\lambda_{\perp}^{e}\right)}} \tag{6.2}$$

After estimating *AWF* and the extra-cellular diffusivities, the microscopic fractional anisotropy can also be estimated, using the general equation for the microscopic fractional anisotropy of for any two compartmental model:

$$\mu FA = \sqrt{\frac{3f\left(\lambda_{\parallel}^{i}-\lambda_{\perp}^{i}\right)^2 + 3(1-f)\left(\lambda_{\parallel}^{e}-\lambda_{\perp}^{e}\right)^2}{2f\left(\lambda_{\parallel}^{i}-\lambda_{\perp}^{i}\right)^2 + 2(1-f)\left(\lambda_{\parallel}^{e}-\lambda_{\perp}^{e}\right)^2 + \left[f\left(\lambda_{\parallel}^{i}+\lambda_{\perp}^{i}\right)^2 + (1-f)\left(\lambda_{\parallel}^{e}+2\lambda_{\perp}^{e}\right)\right]^2}} \tag{6.3}$$

Note that since the estimation of axial and radial diffusivities and microscopic fractional anisotropy depends on the previous *AWF* estimates, a possible pitfall of the adapted version of FBI is that it might be compromised by the biases propagating from *AWF* misestimations. The objective of this chapter is, thus, to implement the FBI *AWF* estimates and assess the robustness of the adaption of FBI to measure the microscopic fractional anisotropy.

6.2 Methods

6.2.1 Simulations

The data used for the FBI model implementation was simulated for evenly sample directions for 50 b-values. Here a higher number of b values is explored for a better assessment of the dependency between *AWF* estimation robustness and extra-cellular signal suppression. The 50 spaced consisted on evenly sampled b-values from 0, included, to 5000 s/mm^2. For each b-values, synthetic signals are produced from 60 different random diffusion-weighted directions. As for the Spherical Mean Technique the signal is simulated through multi tensors reflecting the architectural features of the brain. For these implementations, synthetic noise was also incorporated with a nominal signal-to-noise ratio (SNR) of 38.

Experiment 1 - Testing the validity of the FBI model approximation: firstly, and as for the SMT models, the spherical mean signals from the FBI model are compared to the reference spherical mean signals computed by averaging the signals generated from the multi tensor diffusion signals using the uniformly sampled gradient directions for each of the b-values. The mean signals for both FBI model and multi tensor models were generated for the following ground truth parameters: $\lambda_{\parallel}^{i} = \lambda_{\parallel}^{e} = 2.25$ μm^2/ms, $\lambda_{\perp}^{i} = 0$ μm^2/ms and $\lambda_{\perp}^{e} = 0.9$ μm^2/ms.

To assess the validity of the FBI model main assumption that the extra-cellular space can be suppressed, its predicted spherical mean signals are plotted as a function of increasing b-values. Since the extra-cellular space is only suppressed at high b-values, FBI mean signal prediction is expected to only match the reference signals for high b values, since it ignores the influence of the extra-cellular diffusivities. To assess at what b-value FBI produces accurate axonal water fraction estimates, the FBI model is fitted to the reference mean signals at each b-value and the axonal water fraction estimates are also plotted against increasing b values.

Experiment 2 - Testing the robustness of the parameter estimates from the expanded FBI model: all diffusion parameters of the expanded FBI model (i.e., the extra-cellular axial diffusivity, the extra-cellular radial diffusivity and microscopic fractional anisotropy) are computed for synthetic simulations generated for the b-values sampled in a range between 200 and 5000 s/mm^2. For this, the axonal water fractions are estimated from the higher b-value. Since axonal water fraction is the main parameter estimated from FBI, all diffusion parameters of the FBI model are estimated and plotted against increasing *AWF* ground truth values. These ground truth values range from the *AWF* minimum and maximum values possible, i.e., between 0 and 1. For the sake of simplicity, the extra-cellular axial diffusivity ground truth value was fixed to $\lambda_{\parallel}^{e}$ =2.25 $\mu m^2/ms$, while the extra-cellular radial diffusivity was calculated according to the tortuosity model $\lambda_{\perp}^{e} = (1 - f)\lambda_{\parallel}^{e}$.

6.2.2 *In vivo* data

The adapted version of the FBI model is tested on the same multi b-value dataset described in Chapter 5. It is important to mention that the maximum b value from this data surpasses 2000 s/mm^2, which is necessary for the accurate estimation of the axonal water fraction, and also includes the lower b-value measures required for the estimation of all extra-cellular diffusivities. Based on this data, the following two analysis are performed:

1) Parametric brain maps for all the metrics of the expanded FBI model were plotted for representative data axial slices. These included the extra-cellular axial diffusivity, the extra-cellular radial diffusivity, the axonal water fraction (which was computed for the dataset's higher b-value) and the microscopic fractional anisotropy. *In vivo* data for b-value = 0 s/mm^2 is plotted for the same axial slices as a reference of non-weighted diffusion data.

2) Using all the data b-values, the axonal water fraction (*AWF*) parameter of the FBI model is deeper analyzed. Since its accuracy depends on the b-value used, independent *AWF* measures are computed for each of the b-values. To corroborate this analysis, histogram plots for the individual *AWF* are made for the same increasing b-values.

6.3 Results

6.3.1 Simulations

Experiment 1 - Considering that for this technique water inside tissue is divided into two non-exchanging pools, the signal from extra axonal water pool decreases exponentially as the b-values increase, to the point that it gets neglected, allowing the signal from the intra axonal water pool to become the main source of signal for large b values (Jensen et. al, 2016). For this reason, and due to its diffusion being strongly restricted by membranes, properties from the intra axonal compartment are efficiently calculated. One of these diffusion properties is the axonal water fraction (*AWF*). FBI's *AWF* estimates extracted from the multi-tensor simulations as a function of the increasing b-value are plotted in panel (b) of Figure 26. *AWF* estimates only match its ground truth values at high b-values. Panel a of Figure 26 shows the FBI predicted and reference mean signal decays. This panel shows that, FBI's mean signal decay matches only its reference for a relatively high b-value.

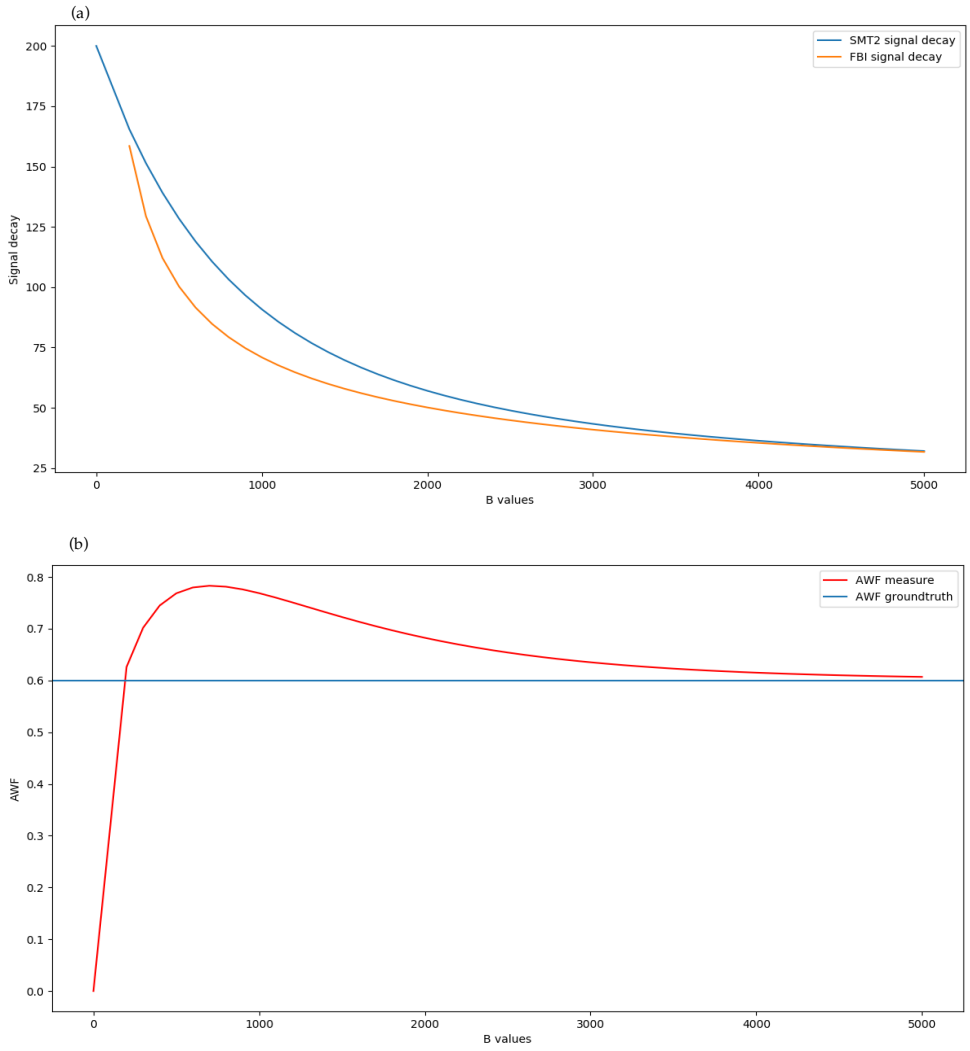

Figure 26 – In panel (a) the FBI signal decay is plotted against increasing b values. The mean signal decay used as reference is computed through the SMT2 model, previously implemented, due to its similarity on compartment assumptions. Panel (b) represents the axonal water fraction estimated through FBI, main parameter of this model, against increasing b values. As ground truth values for these estimates, a fixed value of $AWF = 0.6$ was used.

Experiment 2 - As said previously, AWF, $\lambda_{\perp}^{e}$ and $\lambda_{||}^{e}$ can be estimated using the expanded FBI model using the high and low b-values signals. While the data for the higher b-value of the data is used to estimate the axonal water fraction, the data for the lower b-values allows the estimation of the extra-cellular diffusivity parameters. Plotted against increasing AWF ground truth values are the

diffusivity parameters: extra-cellular axial diffusivity in panel (a), extra-cellular radial diffusivity in panel (b); the axonal water fraction in panel (c) of Figure 27.

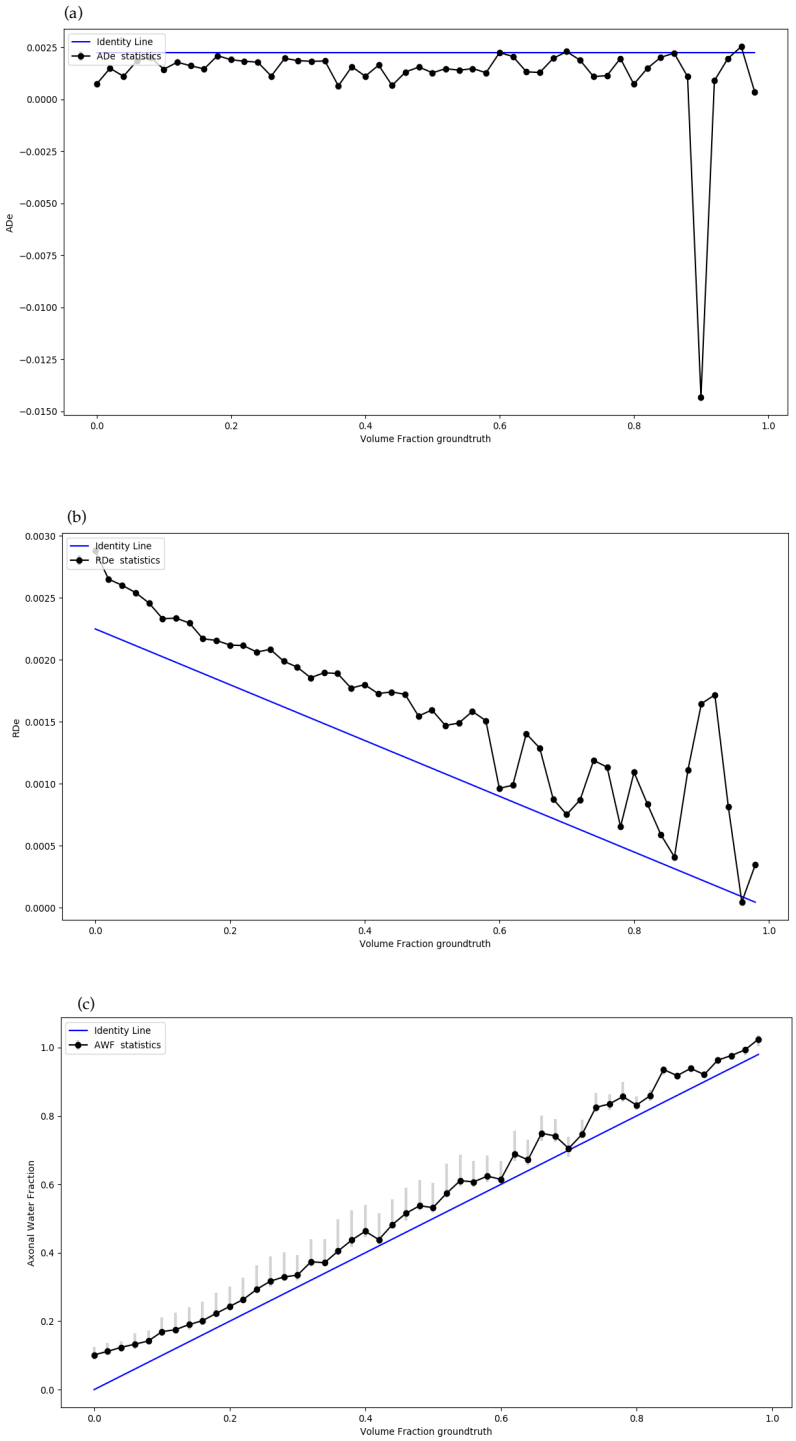

Figure 27 – Axial and extrinsic radial diffusivities estimated through the FBI model are plotted in panels (a) and (b), respectively, against varying volume fraction ground truth values. In panel (c) the axonal water fraction estimates are plotted, again against increasing volume fraction ground truth values.

This Figure shows that the axial diffusivity hovers the ground truth extra-cellular axial diffusivity value of 2.25 $\mu m^2/ms$ with low precision, while the extra-cellular radial diffusivity estimates decreases as a function of the axonal water fraction according to the tortuosity model used to reconstruct the ground truth $\lambda_{\perp}^{e}$ values of the multi-tensor simulations.

Having all the FBI's diffusion parameters estimated, equation 6.2 can be used to estimate the microscopic fractional anisotropy. The FBI microscopic fractional anisotropy estimated from the simulations of experiment 2 are plotted in Figure 28, which was shown to increase as the water volume fraction ground truth values.

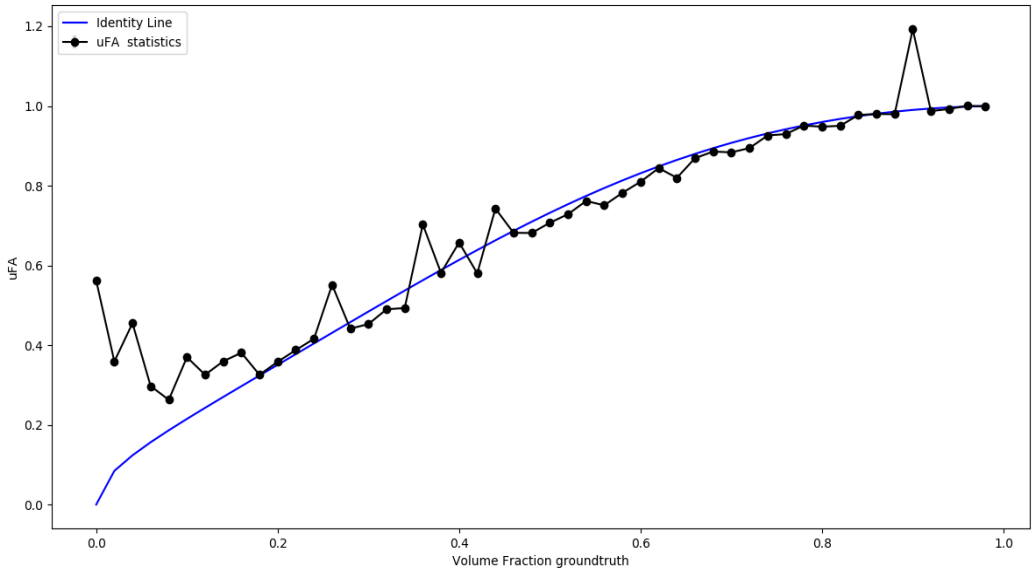

Figure 28 – Micro fractional anisotropy estimated using the FBI model, against increasing volume fraction ground truth values.

6.3.2 *In vivo* data

In vivo data analysis 1 - The fiber ball imaging parameters were plotted in brain maps for two representative axial brain slices in Figure 29. The upper panels correspond to the 5th axial brain slice, while the lower panels correspond to the 10th axial brain slice. The b-value = 0 s/mm^2 data is presented in panels (a) and (e) as a reference image, the extra-cellular axial diffusivity, the extra-cellular radial diffusivity, and the axonal water fraction are plotted in panels (c) and (g), panels (d) and (h) and finally panels (b) and (f), respectively.

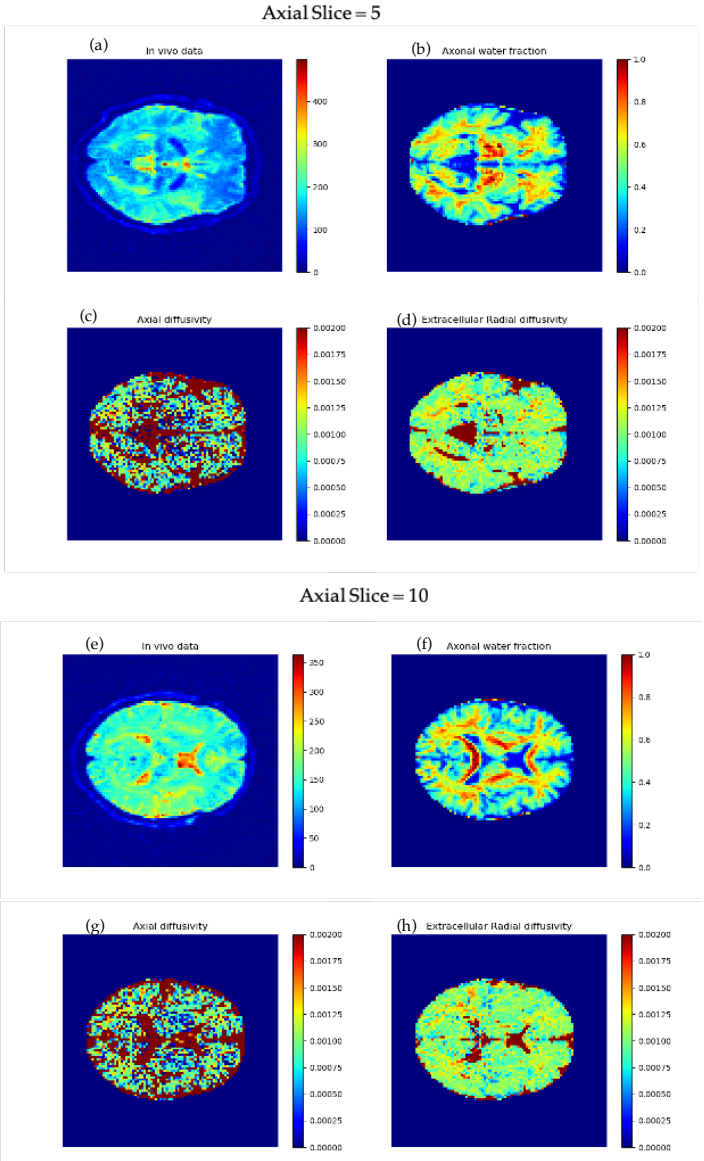

Figure 29 – The diffusion parameters from the FBI model. The extra-cellular axial, extra-cellular radial diffusivities, and axonal water fraction estimates are plotted for two axial brain slices, the 5th and the 10th axial slices. *In vivo* b-value=0 data for both axial brain slices are plotted as a reference for non-weighted diffusion brain maps.

The microscopic fractional anisotropy maps are represented in Figure 30 (panels (a) and (b)), which were computed through all the FBI's parameters mentioned before.

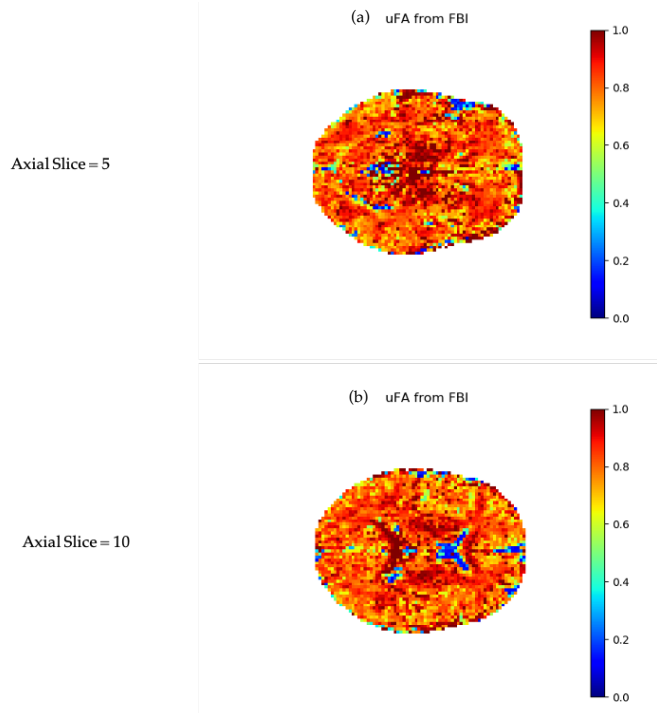

Figure 30 – Microscopic fractional anisotropy estimated with the FBI model plotted for the 5th and 10th axial brain slices.

From the above Figures, one can note that the contrast between white matter and grey matter from the axonal water fraction brain maps is similar to the contrast between white matter and grey matter from microscopic fractional anisotropy brain maps in both slices. Even though these estimates' maps are close in contrast, the *AWF* brain map displays a lot more details than any other diffusion parameter brain map. The axial diffusivity estimates are clearly higher in brain white matter than in grey matter. However, due to the apparent low precision of this latter map, it's hard to accurately identify areas of the brain. For brain regions where the axonal water fraction estimates are of high intensity, extracellular axial and radial diffusivity estimates seem to present low and imprecise estimates.

In vivo data analysis 2 - Since the accurate estimation of axonal water fraction is highly dependent on the used b-value, individual *AWF* estimates are computed from the spherical mean data acquired at different b-values. The panels in Figure 32 correspond to the axonal water fraction maps for increasing b-values, between 0 and 3000 s/mm^2. For higher b values, from panel (k) to (p), and keeping in mind the FBI model extra-cellular suppression assumption, the *AWF* maps begin to appear more in agreement with what was expected, presenting axonal water fraction values closer to one in white matter and lower in grey matter. For a b-value of zero, the *AWF* estimates are null since the signal acquired does not have information on diffusion-weighting (panel (a) of Figure 31).

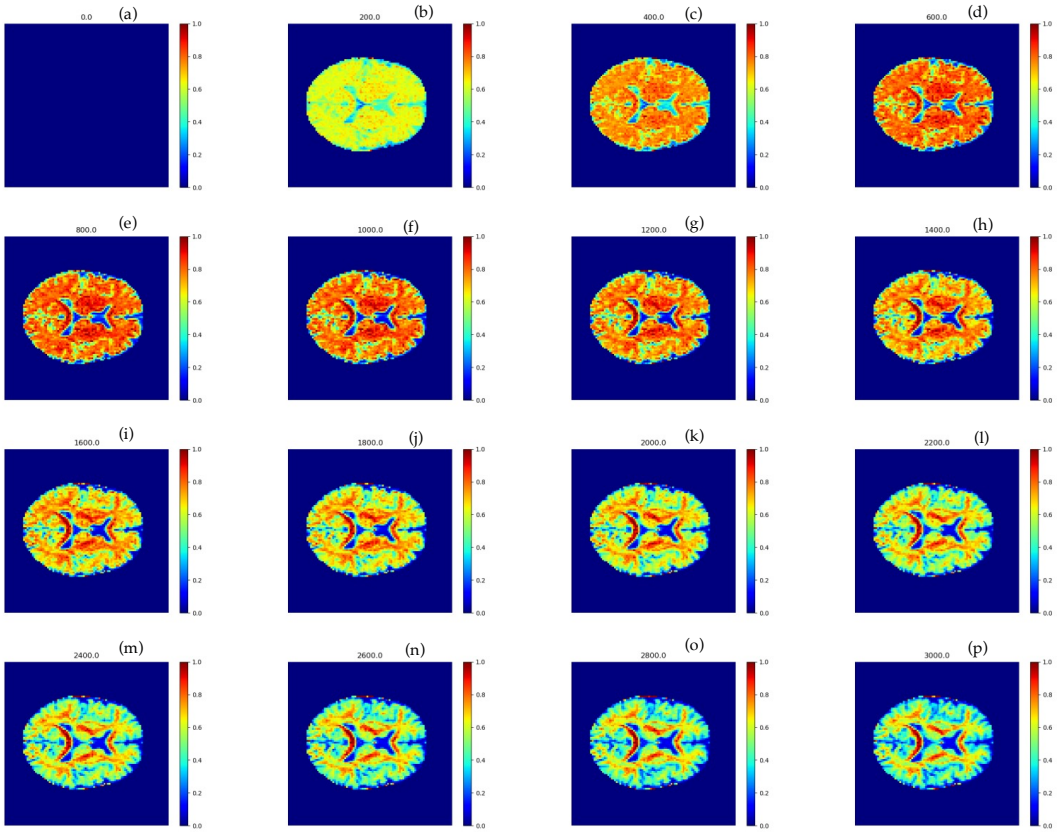

Figure 31 – Axonal water fraction estimates from the FBI model plotted as brain maps. The axial brain slice used for these estimations was the 10th axial slice available in the data. *AWF* estimates are plotted for increasing b value.

To corroborate the axonal water fraction maps, histograms were also computed giving accurate details on the *AWF* values all throughout the brain. From

panel (a) to (p) of Figure 33 histograms are represented for an increasing b value of 0 to 3000 s/mm^2.

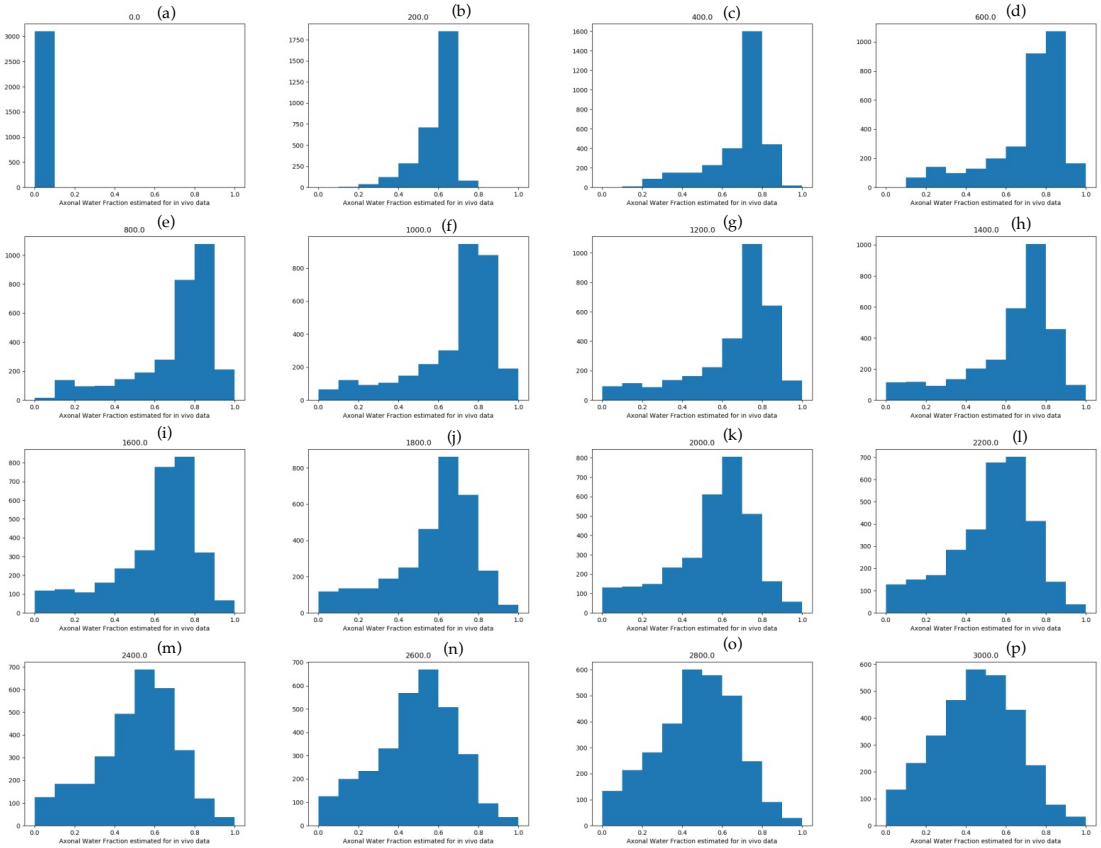

Figure 32 – Histogram plots of the *AWF* estimates for the 10th axial brain slice from the FBI model for increasing b values.

6.4 Discussion

This chapter is dedicated to the Fiber Ball imaging technique implementation and exploration of the adapted FBI model for the estimation of the extra-cellular diffusivities and more general microscopic fractional anisotropy estimates. As in the SMT models implementation, the FBI models is fitted to the spherical mean signals. However, the FBI model does not use constrained values for the extra-cellular diffusivities.

Firstly, single voxel simulations were made to better understand and test the model. Considering that white matter water is divided into two non-exchanging pools, the main constraint imposed in this model is the necessity of higher b-values to suppress the contribution of the extra-cellular signals and allowing the main source of signal to be from the intra axonal water pool. This effect was illustrated from the first simulation experiment which shows that the mean signal predicted by the FBI model (that only considers the intra-cellular signal contribution) matches a reference mean signal decays produced from simulations considering both intra- and extra-cellular compartments at high b-values. The higher the b-value the more alike the signal decays get (Figure 26, panel a). Consequently, the axonal water fraction estimations approach its reference value as the b-value increases (Figure 26, panel b).

For the estimation of the extra-cellular diffusivities using the expanded FBI model signals for lower b-values have to be considered. For the second simulation experiment, all diffusion parameters estimated using the expanded FBI model were plotted against an interval of ground truth volume fraction values widening the parameter analysis. The extracellular radial diffusivity and axonal water fraction parameters hover their reference values. However, these were shown to have low precision specially for high ground truth *AWF* values. Consequently, the microscopic fractional anisotropy estimated from these parameters show to have low precision.

In this chapter, the expanded FBI was also testes in brain data acquired for a healthy human subject. While axonal water fraction maps present plausible

contrasts with higher values for the white matter than for the grey matter, the maps of the axial and radial extra-cellular diffusivities seem to present low precision, particularly for white matter regions that presented *AWF* estimates close to 1. These latter results are consistent with the predictions made for our simulations. The microscopic fractional anisotropy estimated from the expanded FBI model visually seems to suffer from low precision. This may be expected since these are computed from the low precise extra-cellular diffusivities. Despite this, μFA maps show higher values for voxels with higher axonal water fraction estimates. This may suggest that the axonal water fraction parameter is indeed a determinate factor of tissues ground truth microscopic diffusion anisotropy.

The dMRI data was then used to further explore the *AWF* estimation at different b-values. This analysis confirmed the axonal water fraction estimation dependency for different b-value signal, becoming closer to its supposed values of around 1 in white matter and lower in grey matter brain regions as the b-values increase, and confirmed their inaccurate estimation at lower b-values. These results were corroborated with the histograms of the *AWF* estimates computed at increasing b-values.

7

Validation of models in pre-clinical settings

7.1 Introduction

Validation of a model is a process in which the accuracy of the model parameter estimates are compared to ground truth quantities to assess how closely these estimates properly capture a quantity of interest. It is important to remember that all models are just a simplified representation of a system, and thus the validity of their assumptions must be assessed.

Model validations in Magnetic Resonance Imaging are typically performed by comparing the different biophysical estimates with histology. Alternatively, one can also assess the validity of different microstructural estimates by comparing them with other gold standard reference estimations based on strategies that do not rely on strong approximations. For the case of the estimation of microscopic anisotropy, a gold standard reference can be obtained from the information captured using advanced diffusion encodings (DDE, Shemesh et al., 2015). Particularly, double diffusion encoding (DDE) provides direct information

of tissue microscopic diffusion anisotropy through the signals' angular dependence without assuming any model on the microstructure of the tissue (Henriques et al., 2019) (e.g., as describing signals by a finite number of compartments, or assuming fixed diffusivity values for different types of tissue compartments. In this chapter, the microscopic fractional anisotropy from DDE signals acquired at pre-clinical MRI scanners are used as gold references values to assess the validity of the different microstructural models implemented in the previous chapters.

It is important to note that datasets acquired from pre-clinical scanners may provide more adequate information for model validations since they can be acquired will less constraints than clinical scanners (e.g., acquisition time constraints, hardware constraints as on system limited magnetic fields and lower maximum diffusion gradients allowed). Moreover, the use of animal models allows the posterior comparison of estimated model parameters to histological tissue.

7.2 Methods

For this chapter, pre-clinical double diffusion encoding data of a single *ex vivo* mouse brain sample acquired from Henriques et al. (2020) is reused. This data was acquired on a 16.4T vertical bore Aeon Bruker scanner (Karlsruhe, Germany) equipped with a Micro5 probe with gradient coils capable of producing diffusion gradients up to 3000 mT/m (note that most of clinical scanners have magnetic fields ≤ 3 T and have probes capable of producing diffusion gradients up to < 80 mT/m). From the full dataset, DDE acquisitions for parallel double diffusion gradient directions were selected, since these are expected to be equivalent to the single diffusion encoding (SDE) acquisitions under the assumption of tissue compartments with Gaussian diffusion. The selected data contains SDE equivalent data for 72 different gradient directions of 12 b-values (1000, 1250, 1500, 1760, 2000, 2250, 2500, 3000, 3500, 3990, 4500, 5000 s/mm^2) and 420 b-value

= 0 s/mm^2 acquisitions. Other acquisition parameters are: diffusion time = 12ms, diffusion gradient pulse duration = 1.5 ms, TR/ TE = 2200/52 ms, Field of View = 10.4 x 10.4 mm^2, matrix size = 80 x 80, leading to an in-plane voxel resolution of 130 x 130 μm^2, slice thickness = 0.9 mm, slice gap = 0.6 mm, number of averages = 8. A more detailed description of the acquisition parameters is reported in Henriques et al. (2020).

The reference microscopic anisotropy is computed from double diffusion encoding using Correlation Tensor magnetic resonance imaging (Henriques et al., 2020). Since this technique estimates μFA in a model avoiding microstructural model assumptions and parameter constraints, its μFA estimates are considered as gold reference estimates for the evaluation of μFA estimates from SMT1, SMT2, and FBI microstructural models. Important to mention that white matter and gray matter can be roughly segmented by a DDE μFA value of 0.5 μm^2/ms, as μFA values for white matter are usually higher than 0.5 μm^2/ms and the contrary for gray matter (Henriques et al., 2019), useful information for the models' assessment in the brain.

Analysis 1 - to validate the SMT models, dMRI data is used to estimate the diffusion parameters through each of the SMT models (for the SMT1 model the diffusion parameters estimated are the axial and radial diffusivities, while for the SMT2 model the parameters are the intrinsic axial diffusivity and the water volume fraction). After the estimation of SMT model parameters at each image voxel, these are used to compute the different microscopic anisotropy estimates which are compared to the reference microscopic diffusion anisotropy estimates that were previously computed from Henriques et al. (2020).

Analysis 2 - since the selected pre-clinical data contains data for a wide range of b-values, these data conditions are ideal to also analyze the axonal water fraction estimated from the standard fiber ball imaging model and the extra-cellular axial diffusivity, extra-cellular radial diffusivity and FBI's microscopic fractional anisotropy.

Analysis 3 - for a better understanding and further validation of all three models, SMT1, SMT2 and FBI, the microscopic fractional anisotropy measurements estimated with all models previously mentioned, are represented as scatter plots against the μFA computed through double diffusion encoding, used as a gold reference. These plots acquire information about the over and under estimation of this anisotropy measurement of the brain, validating and demonstrating the limitations of the models in question.

Analysis 4 - Under the hypothesis that the axonal water fraction may be a determinant factor of tissue microscopic fractional anisotropy, the correlation between the water volume fraction estimates from the FBI model and the DDE ground truth microscopic fractional anisotropy measurement is also studied.

7.3 Results

Analysis were made for all the parameters the SMT models that are essential for computing the μFA. These parameters, represented as brain maps in Figure 33, are the axial and radial diffusivities for SMT1 model, panels (a) and (b), and the intrinsic axial diffusivity and water volume fraction for the SMT2 model, panels (c) and (d).

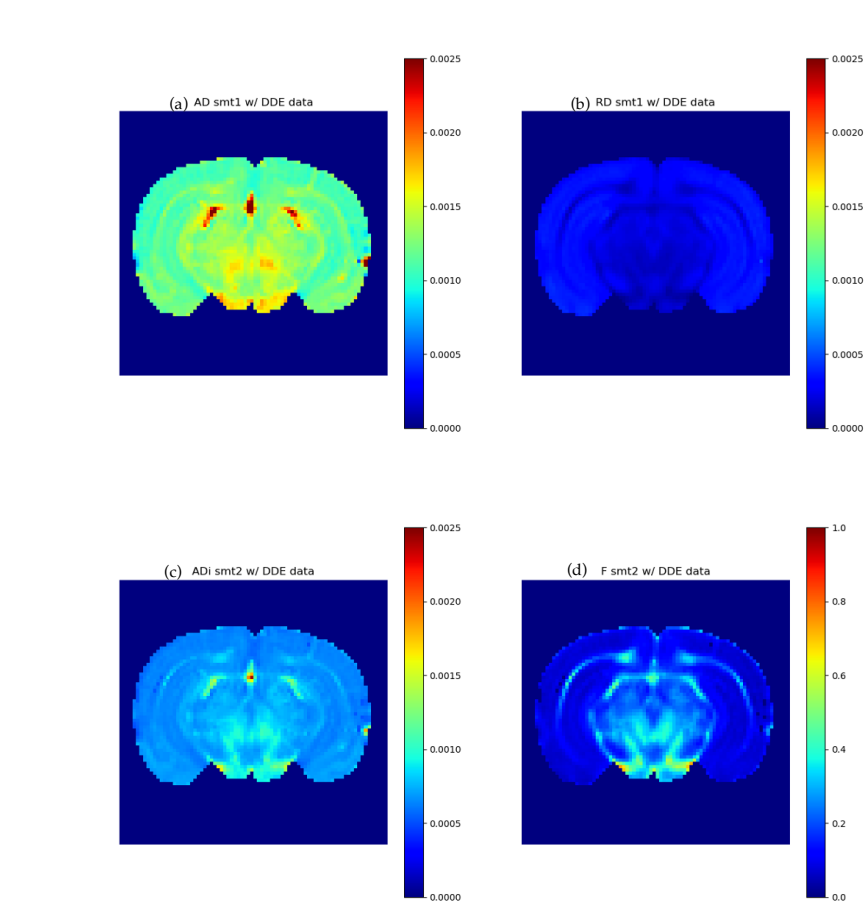

Figure 33 – SMT models parameters plots using *ex vivo* mouse dMRI data. For the SMT1 model, the axial and radial diffusivities are plotted while for the SMT2 model the intrinsic axial diffusivity and water volume fraction estimates are plotted.

The SMT parametric maps from the *ex vivo* mouse dMRI data present similar characteristics to those from the *in vivo* human dMRI data presented in Chapter 5. While axial diffusivity maps (panel (a)) present high intensities, radial diffusivity estimates (panel (b)) are low, particularly in the white matter brain regions of interest. As for the human data, SMT2 parametric maps show white matter microenvironments with a greater spatial heterogeneity of values than the SMT1 parametric maps. Particularly, the axonal volume fraction maps (panel (d)) presents higher intensities in the corpus callosum. These values are not higher than 0.5 as for the *in vivo* human data.

FBI axonal water fraction estimates showed to only present plausible values when computed from the higher b-value data (according to the theory presented on previous chapter this is expected since it is only at high b-values that the intra axonal water pools' signal becomes the main source of tissue signal). The *AWF* estimates for the higher b-value data are represented in panel (a) of Figure 34, together with the extra-cellular radial diffusivity (in panel (b)) and the extra-cellular axial diffusivity (in panel (c)) extracted from the expanded FBI technique.

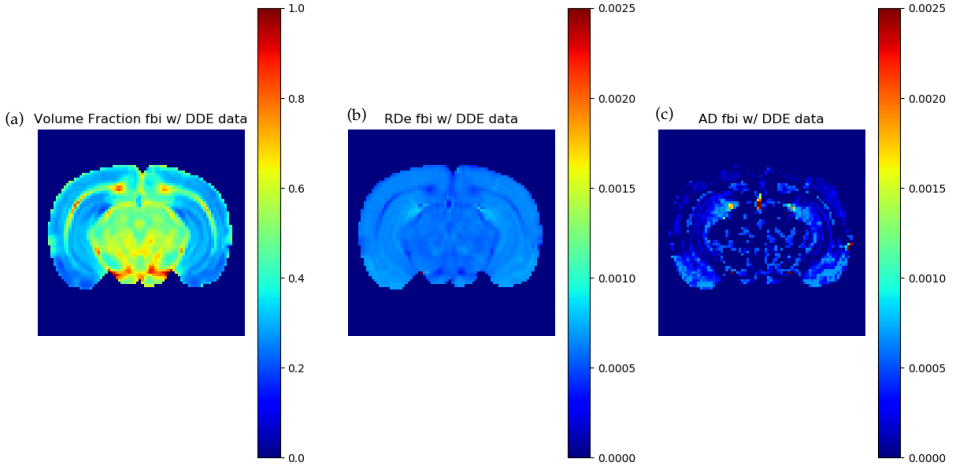

Figure 34 - FBI model parametric maps using *ex vivo* mouse dMRI data. These diffusion parameters are the water volume fraction, the extracellular radial diffusivity and the extracellular axial diffusivity.

The above Figure shows that the parametric maps obtained from the expanded FBI model present low precision, particularly the intra-cellular axial diffusivity.

To validate the micro fractional anisotropy estimates from the three microstructural models implemented, brain maps were plotted for the μFA estimates from the spherical mean technique for 1 and 2 compartments (SMT1 and SMT2), the fiber ball imaging technique and from the DDE acquisition as a reference measure. This diffusion parameter was plotted for all the 5 axial brain slices for all three models in Figure 35, in which the first panel column corresponds to the reference μFA^{DDE} from DDE acquisition, the second and third panel columns

represent μFA^{SMT} from the spherical mean technique, for one (μFA^{SMT1}) and two compartments (μFA^{SMT2}) respectively, and the latter panel column depicts μFA^{FBI} from the fiber ball imaging technique.

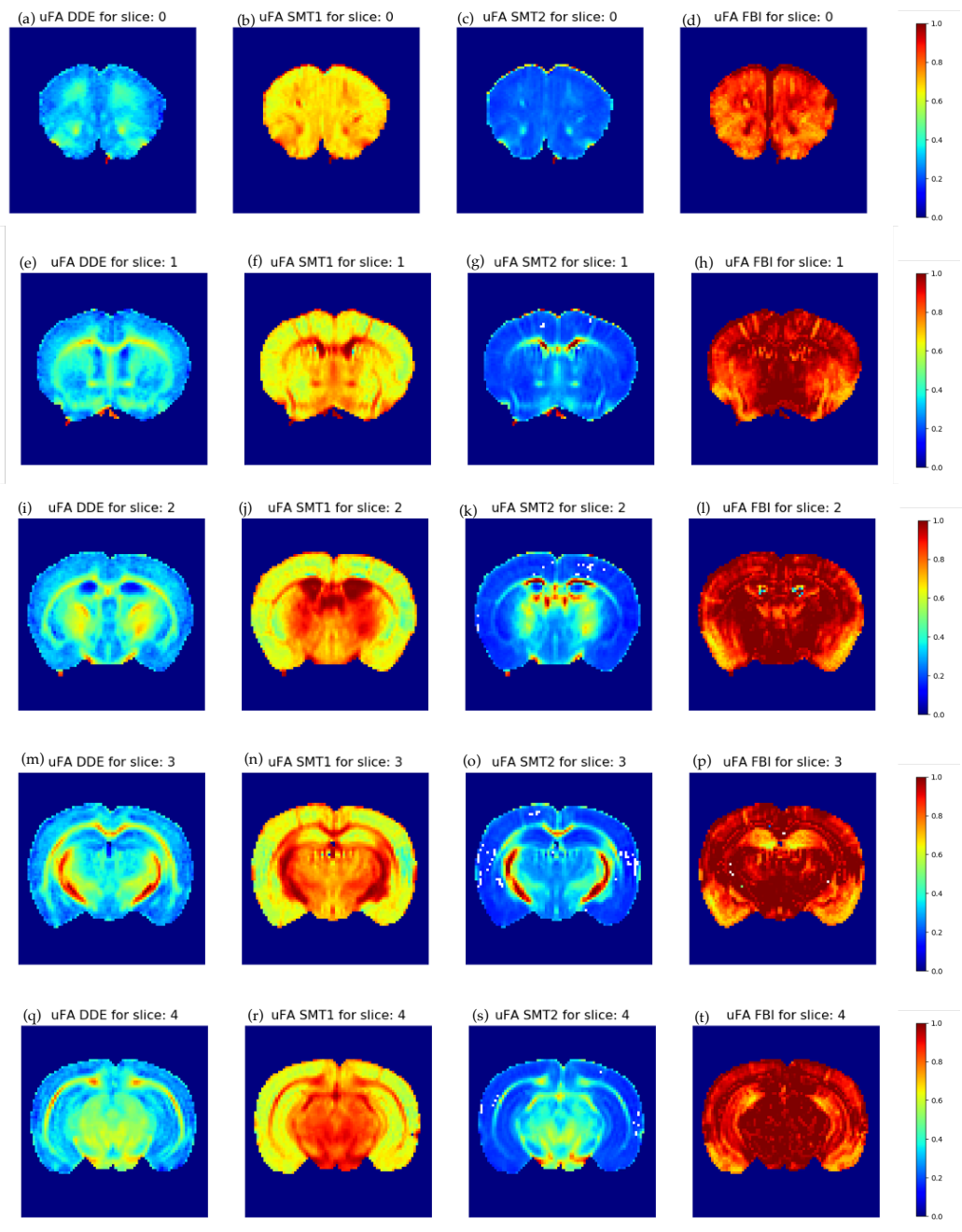

Figure 35 – Micro fractional anisotropy estimates from all implemented models, the FBI and the SMT models are here plotted. As a reference measure, the micro fractional anisotropy computed using *ex vivo* mouse dMRI data is also plotted. All μFA estimates are plotted for five different brain axial slices.

When compared to the reference values, microscopic fractional anisotropy measurements estimated through the SMT2 are underestimated in gray matter and overestimated in white matter. Note that SMT2's μFA estimates are computed only from its axonal water fraction estimates, unlike in the model free μFA from DDE, which are expected to depend on the diffusivities of all compartments of tissue. On the contrary microscopic fractional anisotropy estimates computed through the SMT1 model appear to be highly overestimated when compared with the reference μFA^{DDE}.

In the FBI model, μFA estimates are overly estimated and their maps appear to be noisy. These comparisons can be corroborated using scatter plots of μFA estimates from the 3 models implemented against the μFA^{DDE} reference values from all voxels (Figure 36).

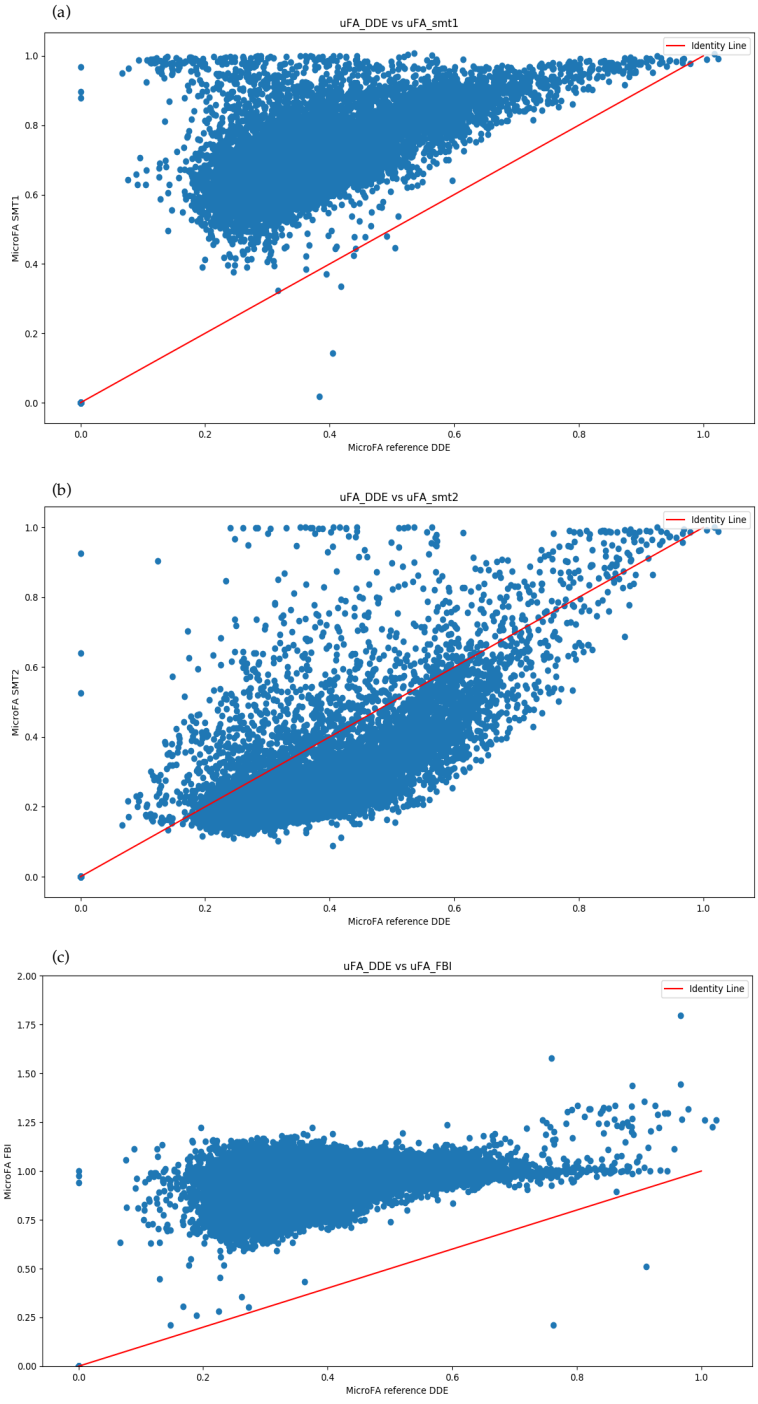

Figure 36 - Scatter plots of all micro fractional anisotropy estimates from the SMT and FBI models, against ground truth values computed using *ex vivo* mouse dMRI data.

The scatter plots confirm that μFA^{SMT1} appears to be overestimated all throughout the voxels (panel (a)), μFA^{SMT2} appears to be mainly underestimated, particularly for the gray matter regions (panel (b)). μFA^{SMT2} is also overestimated for higher μFA regions such as in WM. μFA^{FBI} is overly estimated when in comparison to μFA^{DDE} (panel (c)).

For a better understanding of the correlation between axonal water fraction estimates and the microscopic fractional anisotropy, scatter plots between FBI's *AWF* measures and the reference μFA estimated were produced in Figure 37. Note that for this analysis, axonal water fraction was computed for the data acquired with the data's higher b-value. This scatter plot shows how strong the linear relationship between these two diffusion parameters is. Particularly, higher axonal water fraction estimates are related to larger microscopic fractional anisotropy values. This scatter plot supports that axonal water fraction is a determinant factor for tissue microscopic diffusion anisotropy.

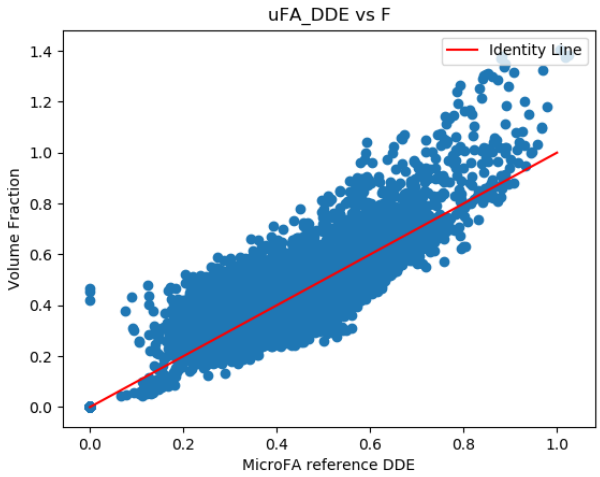

Figure 37 – Scatter plots of the volume fraction measurement estimated with the FBI model against microscopic fractional anisotropy reference values computed with DDE data. The identity line is a linear regression of these estimates.

7.4 Discussion

In this chapter, the validation of both spherical mean technique for one and two gaussian compartments and fiber ball imaging technique was made using pre-clinical data. Data from a single *ex vivo* mouse brain sample and characterized by a high number of b-values containing unique information about microscopic diffusion anisotropy of DDE signal and equivalent to single diffusion encoding (SDE) data, is ideal for model validation.

For the model's validation, diffusion parameters for each microscopic model were computed from the equivalent SDE data. For the spherical mean technique model, the SMT1 parametric maps (Figure 33) show similar properties to the ones previously computed from the in vivo maps (Chapter 5), presenting higher axial diffusivity values for white matter and lower radial diffusivity values for both white and grey matter. Expanding the SMT1 model to two compartments, the SMT2 model presents greater spatial heterogeneity in white matter. Particularly, water volume fraction estimates show the higher values in the corpus callosum. In comparison with SMT2, the SMT2 model also reveals microscopic diffusion anisotropy estimates that are in better agreement with its reference values.

The pre-clinical data is characterized by high b-values, proper for the FBI model validation. Even though increasing the b-values provides deeper diffusion weighted information of the brain, the microscopic fractional anisotropy estimated from the expanded FBI model visually seems to suffer from low precision. This is expected since these are also computed from the low unprecise extra-cellular diffusivities.

DDE diffusivity estimates for the FBI model were underestimated when compared to the results obtained on chapter 6, which means that the axonal water fraction estimates errors on the extra-cellular diffusivities estimation are greater than for the *in vivo* human data. However, not all FBI model parameters seem to be miscalculated. For instance, the water volume fraction estimates computed from the highest b-value data still presents the high contrast across different

brain regions as expected by the prior *in vivo* human brain results. It was also shown, by the use of scatter plots, that this latter parameter has a linear dependency with the object of study of this dissertation, the microscopic fractional anisotropy. This supports that axonal water fraction estimates are a determining factor of microscopic diffusion anisotropy of biological tissues.

All models tested on this project focus on estimating the parameters capable of estimating tissue's microscopic fractional anisotropy, reason why the validation study performed on this chapter is of major importance for this project. Microscopic fractional anisotropy analysis was made for different brain slices for all three models (SMT1, SMT2 and FBI) and compared with the gold standard μFA reference computed through DDE data. Consistently to previous studies (Henriques et al., 2019), this study points that the SMT models misestimate microscopic fractional anisotropy estimates which can be a consequence of effects not considered by these models such as the ones arising from heterogeneities of the kurtosis signal and a consequence of the strong constraints imposed by the models. On the other hand, the expanded FBI microscopic fractional anisotropy estimates were here compared to ground truth μFA values for the first time. Although FBI μFA estimates show the expected higher values in white matter, these showed a poor correlation with the ground truth parameters due to the error propagation from noisy extra-cellular diffusivity estimates.

8

Conclusions & Future work

In this thesis, microstructural models were implemented to explore the microscopic diffusion anisotropy - a property of diffusion in biological tissue that is independent to tissue orientation dispersion, providing a more direct access to the microscopic structure of the brain. Withdrawing the orientations' influence on the diffusion magnetic resonance imaging data, these state-of-the-art microstructural models surpass previous models' limitations, providing estimates of diffusion parameters for individual tissue compartments even for white matter regions of crossing fiber populations. In particular, the models explored on this dissertation are two spherical mean techniques which differ on the number of cellular compartments used to represent the tissue (Kaden et al., 2016a; 2016b), and the fiber ball imaging technique (Jensen et. al, 2016). Moreover, to validate these microstructural models, a technique based in advanced sequences, double diffusion encoding, was also used to provide a model free microscopic fractional anisotropy (Henriques et al., 2019).

Chapter 5 is dedicated to the spherical mean techniques' implementation and testing. Assuming that a tissue can be represented by one type of compartment and since the spherical mean of the signal is independent to the axons' orientation, simulations were made to test the models' implementations on data. The SMT1 model requires a signal constrained to one gaussian component, so to

differentiate between the intracellular and extracellular mediums, it was later expanded into a two compartmental model, the SMT2 (Kaden et al., 2016b). Computing the spherical mean signal decays, it was shown that its independency on orientation dispersion enables the estimation of the diffusion parameters of interest for the SMT1 and SMT2 models. These are the axial and radial diffusivities for the SMT1 model, and the intrinsic axial diffusivity and water volume fraction for the SMT2 model. For single voxel simulations, the implementations provided on this project show that all diffusion parameters of both models can be accurately estimated when simulations are produced according to the model assumptions. SMT models also show to present close estimations to their ground truth values even when noise was introduced in the simulations. It is important to note that both these models assume axons as sticks, ignoring axon size distributions in white matter (Henriques et. al, 2018) and that the SMT models do not impose any assumptions or constraints on the orientation dispersion function of tissues, and thus diffusion parameters can be computed generally independently to the degree of tissue alignment coherence. Particularly, one of SMT's parameter of interest is the micro fractional anisotropy estimation which can only be estimated if the effects of tissue dispersion are removed. For SMT1, and according to literature, this latter parameter is estimated from the axial and radial diffusivities. On the other hand, for the SMT2 model, the microscopic fractional anisotropy is fully estimated from the axonal volume fraction estimation, with increasing estimates for increasing volume fraction values, as anticipated. Microscopic fractional anisotropy estimates based only on the AWF values are a consequence of the models' approximations. Furthermore, this simplistic relationship indirectly reveals the limitation of SMT2 in the μFA estimate. Theoretically, it is expected that μFA depends on differences between the diffusivities of different compartments and these effects are not being captured by the SMT2 model.

Single voxel simulations came to reassure the results found in the SMT parametric maps obtained from dMRI data. Since radial diffusivity estimates were mainly low all throughout the brain and axial diffusivities were highly contrasted on white matter, μFA estimates presented higher values in white matter, as expected in the SMT1 model. Since the SMT2 models' μFA estimates rest on

water volume fraction only, these parameters provided similar brain mapping results, even though intrinsic axial diffusivity misestimations induce over or under estimations of this anisotropy measure.

For further evaluation of the dependencies between SMT estimation and the dMRI acquisition parameters, a cluster of tests were performed to the signal simulation protocol, particularly the number of used b-values and gradient directions were independently validated. The results of this dissertation showed that the precision of SMT model estimates improves with the number of points in a signal generated, independently if these are sampled for a larger number of b-values or gradient directions. Finally, simulations were performed to test the robustness of SMT parameter estimate for when their model assumptions are not met. These showed that adding a different diffusivity extra-cellular compartment in simulations, the SMT1 model provides inaccurate estimates since this can only portray diffusion of a single comportment. On the other hand, SMT2 model misestimates μFA when simulations are performed for ground truth values that do not follow the first order tortuosity approximation.

The Fiber ball imaging technique implementation was reported on Chapter 6. On the contrary to the SMT models, it does not assume any correlation between diffusivities of the intra- and extra-cellular compartments. Instead, it assumed that the extracellular compartment can be eliminated using high diffusion gradient intensities (McKinnon et al., 2018), allowing the intra axonal signal to become the main source of signal for this model (Jensen et. al, 2016). Indeed, through a comparison with the reference spherical mean signal decay from multi-tensor simulations that consider both intra- and extra-cellular compartments, it was shown that the FBI model only presents accurate estimations of the axonal water fraction for signals with high intensity diffusion gradients, allowing the extracellular medium to not be considered. However, the low intensity diffusion gradients are required to provide the information of the extra-cellular diffusivities which in turn are needed to estimate microscopic fractional anisotropy. Therefore, in this project, an expanded version of the FBI model was tested which uses the information of both high and low b-values to also estimate the axial and radial extra-cellular diffusivities and posteriorly a more general estimate of μFA

than the SMT models. Although the parameters of expanded the FBI were shown to follow in general their ground truth trends, simulations showed that FBI extracellular diffusivities and consequently the μFA present low precision. The expanded FBI model was also applied to *in vivo* human brain dMRI data. These maps show that the axonal water fraction estimates presented similar characteristics to the microscopic fractional anisotropy. This result suggests that the axonal water fraction may be a determinant factor for tissues' microscopic fractional anisotropy. To better understand the FBI model, additional testing was performed corroborating these latter parameters dependence.

The implemented models' validation based on pre-clinical dMRI data of *ex vivo* mouse brain was shown in chapter 7. The advanced sequences technique that best fits these models' validations was Double Diffusion Encoding (DDE), since their parallel acquisitions provide data which is equivalent to single diffusion encoding data. Therefore, all SMT and FBI parameters necessary for the model-based microscopic fractional anisotropy estimation were applied to the portion of DDE data which was equivalent to SDE experiments. Parametric maps obtained from the *ex vivo* mouse brain data presented similar characteristics to the results obtained from simulations and *in vivo* datasets. Moreover, in general, results show that the microscopic fractional anisotropy estimates from the two compartment models (i.e., the SMT2 and the FBI models) reveal more similar results to DDE's reference values. However, a clear mismatch between the microscopic fractional anisotropy from all microstructural models and the DDE's reference values was observed. For the spherical mean technique model, these estimates were over and underestimated, for SMT1 and SMT2 respectively. These over and underestimations were previously shown to be a consequence of non-Gaussian (kurtosis) diffusion effects not considered by these models (Henriques et al., 2019). On the other hand, FBI model's estimates showed over-estimated microscopic fractional diffusion estimates all throughout the brain. These are likely to be a consequence of the error biases propagation through the different steps of FBI parameter estimations. Interestingly, the results of chapter 7 confirmed the high correlations between the FBI's estimated axonal water fraction

and the reference microscopic fractional diffusion estimates, supporting that axonal fraction estimates may indeed be the major factor that underpins tissue microscopic anisotropy.

In summary, even though these models assume the type of compartments that characterize a biological tissue and infer correlations between diffusion parameters that in reality are uncorrelated and don't take into consideration the exchange of water between them, these microstructural models are accurately able to compute the main measure of diffusion anisotropy, the micro fractional anisotropy, although presenting limitations to its use. Every model, SMT1, SMT2 and FBI was successfully implemented and validated, giving rise to results in conformity with the ground truth and reference values proposed for each of them. Some under and over-estimations were found when compared to the gold DDE μFA reference measure, result of introducing models on the microstructure whilst for the DDE acquisition no models on microstructure are taken into account.

Future Work

Since this thesis confirmed that SMT misestimates tissue microstructural diffusion anisotropy, future studies should revise the assumptions considered by the SMT1 and SMT2 models. Expansions of the SMT models could for example include more tissue compartments which could represent tissue components not considered by current SMT models, just as the presence of free water diffusion or the soma of neurites. This could be fundamental for a more realistic representation of the biological tissues, and their robustness should be tested and validated the same way the SMT1 and SMT2 models were tested and validated in this project.

Likewise, for further improvement of the FBI model, different approaches to more robustly estimate the extra-cellular diffusivities by directly fitting the signal model to the microstructural framework should be explored. This may include strategies that simultaneous fit the FBI parameters with the orientation distribution ODF by representing it by spherical harmonics to represent orientation distribution functions ODF, instead of powder average signals. Although this involves the estimation of a larger number of parameters, the information captured by spherical harmonics could help regularize the extra-cellular diffusivity parameters as proposed by McKinnon et. al (2018).

9

Bibliographic References

Assaf, Y., & Basser, P. J. (2005). Composite hindered and restricted model of diffusion (CHARMED) MR imaging of the human brain. *NeuroImage*, *27*(1), 48–58. https://doi.org/10.1016/j.neuroimage.2005.03.042

Assaf, Y., Freidlin, R. Z., Rohde, G. K., & Basser, P. J. (2004). New modeling and experimental framework to characterize hindered and restricted water diffusion in brain white matter. *Magnetic Resonance in Medicine*. https://doi.org/10.1002/mrm.20274

Basser, P. J., Mattiello, J., & LeBihan, D. (1994). MR diffusion tensor spectroscopy and imaging. *Biophysical Journal*, *66*(1), 259–267. https://doi.org/10.1016/S0006-3495(94)80775-1

Basser, P.J., Pajevic, S., Pierpaoli, C., Duda, J., Aldroubi, A., 2000. In Vivo Fiber Tractography Using DT-MRI Data. Magn. Reson. Med. 44, 625-632.

Basser, P.J., Pierpaoli, C., 1996. Microstructural and Physiological Features of Tissues Elucidated by Quantitative-Diffusion-Tensor MRI. J. Magn. Reson. B 111, 209–219.

Beaulieu, C. (2002). The basis of anisotropic water diffusion in the nervous system - a technical review. *NMR in Biomedicine*, *15*(7–8), 435–455. https://doi.org/10.1002/nbm.782

Boltzmann distribution of spin energies - Questions and Answers in MRI. (n.d.). Retrieved January 16, 2020, from http://mri-q.com/fall-to-lowest-state.html

Bottomley, P. A., Foster, T. H., Argersinger, R. E., & Pfeifer, L. M. (1984). A review of normal tissue hydrogen NMR relaxation times and relaxation mechanisms from 1-100 MHz: dependence on tissue type, NMR frequency, temperature, species, excision, and age. *Medical Physics*, *11*(4), 425–448. https://doi.org/10.1118/1.595535

Brown, M. A., & Semelka, R. C. (2005). *MRI: Basic Principles and Applications. Third Edition* DOI: 10.1002/0471467936.index

Brown, R. (1827), Brownian motion, *PhyS Educ,* Volume 13 Printed in Great Britain (1978)

Budde, M. D., & Frank, J. A. (2010). Neurite beading is sufficient to decrease the apparent diffusion coefficient after ischemic stroke. *Proceedings of the National Academy of Sciences of the United States of America*. https://doi.org/10.1073/pnas.1004841107

De Santis, S., Drakesmith, M., Bells, S., Assaf, Y., Jones, D.K., (2014). Why diffusion tensor MRI does well only some of the time: variance and covariance of white matter tissue microstructure attributes in the living human brain. Neuroimage 89, 35-44. doi: 10.1016/j.neuroimage.2013.12.00

Einstein, A. (1956), Investigations on the Theory of Brownian Motion, Reprint of the 1st English edition (1926), *Dover*, New-York

Freedman, D. (1983). Brownian Motion and Diffusion. In *Brownian Motion and Diffusion*. https://doi.org/10.1007/978-1-4615-6574-1

Garyfallidis, E., Brett, M., Amirbekian, B., Rokem, A., van der Walt, S., Descoteaux, M., & Nimmo-Smith, I. (2014). Dipy, a library for the analysis of diffusion MRI data. *Frontiers in Neuroinformatics*, *8*. https://doi.org/10.3389/fninf.2014.00008

Hahn, E. L. (1950). Spin echoes. Physical Review. https://doi.org/10.1103/PhysRev.80.580

Hansen, B., & Jespersen, S. N. (2016). Data for evaluation of fast kurtosis strategies, b-value optimization and exploration of diffusion MRI contrast. *Scientific Data*, *3*(1), 160072. https://doi.org/10.1038/sdata.2016.72

Harris, R. K. (1983), Nuclear Magnetic Resonance Spectroscopy: A Physicochemical view, *Pitman*

Heisenberg, W. (1927), The descriptive content about the quantum theoretical kinematics and mechanics, *Zeitschrift für Physik* (in German), 43 (3–4): 172–198, doi:10.1007/BF01397280

Heitjans, P., & Kärger, J. (2005). Diffusion in Condensed Matter. In P. Heitjans & J. Kärger (Eds.), *Diffusion in Condensed Matter: Methods, Materials, Models*. https://doi.org/10.1007/3-540-30970-5

Henriques, R. N. (2018). Advanced Methods for Diffusion MRI Data Analysis and their Application to the Healthy Ageing Brain (Doctoral thesis). https://doi.org/10.17863/CAM.29356

Henriques, R. N., Correia, M. M., Nunes, R. G., & Ferreira, H. A. (2015). Exploring the 3D geometry of the diffusion kurtosis tensor—Impact on the development of robust tractography procedures and novel biomarkers. *NeuroImage*, *111*, 85–99. https://doi.org/10.1016/j.neuroimage.2015.02.004

Henriques, R. N., Jespersen, S. N., & Shemesh, N. (2019). Microscopic anisotropy misestimation in spherical-mean single diffusion encoding MRI. *Magnetic Resonance in Medicine*, *81*(5), 3245–3261. https://doi.org/10.1002/mrm.27606

Henriques, R. N., Jespersen, S. N., & Shemesh, N. (2020). Correlation tensor magnetic resonance imaging. *NeuroImage*, *211*, 116605. https://doi.org/10.1016/j.neuroimage.2020.116605

https://www.nature.com/articles/sdata201672

Huber, E., Henriques, R. N., Owen, J. P., Rokem, A., & Yeatman, J. D. (2019). Applying microstructural models to understand the role of white matter in cognitive development. *Developmental Cognitive Neuroscience*, *36*, 100624. https://doi.org/10.1016/j.dcn.2019.100624

Ianuş, A., Jespersen, S. N., Serradas Duarte, T., Alexander, D. C., Drobnjak, I., & Shemesh, N. (2018). Accurate estimation of microscopic diffusion anisotropy and its time dependence in the mouse brain. *NeuroImage*. https://doi.org/10.1016/j.neuroimage.2018.08.034

Jensen, J. H., Helpern, J. A., Ramani, A., Lu, H., & Kaczynski, K. (2005). Diffusional kurtosis imaging: The quantification of non-gaussian water diffusion by means of magnetic resonance imaging. *Magnetic Resonance in Medicine*, *53*(6), 1432–1440. https://doi.org/10.1002/mrm.20508

Jensen, J. H., Russell Glenn, G., & Helpern, J. A. (2016). Fiber ball imaging. *NeuroImage*. https://doi.org/10.1016/j.neuroimage.2015.09.049

Jespersen, S. N., Kroenke, C. D., Østergaard, L., Ackerman, J. J. H., & Yablonskiy, D. A. (2007). Modeling dendrite density from magnetic resonance diffusion measurements. *NeuroImage*. https://doi.org/10.1016/j.neuroimage.2006.10.037

Johansen-Berg, H., & Behrens, T. E. J. (2014). Diffusion MRI : from quantitative measurement to in-vivo neuroanatomy. Elsevier Science.

Kaden, E., Kelm, N. D., Carson, R. P., Does, M. D., & Alexander, D. C. (2016). Multi-compartment microscopic diffusion imaging. *NeuroImage*, *139*, 346–359. https://doi.org/10.1016/j.neuroimage.2016.06.002

Kaden, E., Kruggel, F., & Alexander, D. C. (2016a). Quantitative mapping of the per-axon diffusion coefficients in brain white matter. *Magnetic Resonance in Medicine*, *75*(4), 1752–1763. https://doi.org/10.1002/mrm.25734

Le Bihan, D., & Iima, M. (2015). Diffusion Magnetic Resonance Imaging: What Water Tells Us about Biological Tissues. *PLOS Biology*, *13*(7), e1002203. https://doi.org/10.1371/journal.pbio.1002203

Le Bihan, D., & Johansen-Berg, H. (2012). Diffusion MRI at 25: exploring brain tissue structure and function. *NeuroImage*, *61*(2), 324–341. https://doi.org/10.1016/j.neuroimage.2011.11.006

Le Bihan, D., Breton, E., Lallemand, D., Grenier, P., Cabanis, E., & Laval-Jeantet, M. (1986). MR imaging of intravoxel incoherent motions: application to

diffusion and perfusion in neurologic disorders. *Radiology*, *161*(2), 401–407. https://doi.org/10.1148/radiology.161.2.3763909

Likes, R. (1979). Moving Gradient Zeugmatography.

McKinnon, E. T., Helpern, J. A., & Jensen, J. H. (2018). Modeling white matter microstructure with fiber ball imaging. *NeuroImage*, *176*, 11–21. https://doi.org/10.1016/j.neuroimage.2018.04.025

McRobbie, D. W., Moore, E. A., Graves, M. J., & Prince, M. R. (2006). MRI from picture to proton. In *MRI from Picture to Proton*. https://doi.org/10.1017/CBO9780511545405

Moseley, M. E., Cohen, Y., Kucharczyk, J., Mintorovitch, J., Asgari, H. S., Wendland, M. F., … Norman, D. (1990). Diffusion-weighted MR imaging of anisotropic water diffusion in cat central nervous system. *Radiology*, *176*(2), 439–445. https://doi.org/10.1148/radiology.176.2.2367658

Nilsson, M., van Westen, D., Ståhlberg, F., Sundgren, P. C., & Lätt, J. (2013). The role of tissue microstructure and water exchange in biophysical modelling of diffusion in white matter. *Magnetic Resonance Materials in Physics, Biology and Medicine*, *26*(4), 345–370. https://doi.org/10.1007/s10334-013-0371-x

Novikov, D. S., Kiselev, V. G., & Jespersen, S. N. (2018). On modeling. *Magnetic Resonance in Medicine*, *79*(6), 3172–3193. https://doi.org/10.1002/mrm.27101

Pierpaoli, C., & Basser, P. J. (1996). Toward a quantitative assessment of diffusion anisotropy. *Magnetic Resonance in Medicine*, *36*(6), 893–906. https://doi.org/10.1002/mrm.1910360612

Shemesh, N., Jespersen, S. N., Alexander, D. C., Cohen, Y., Drobnjak, I., Dyrby, T. B., … Westin, C.-F. (2015). Conventions and nomenclature for double diffusion encoding NMR and MRI. *Magnetic Resonance in Medicine*, *75*(1), 82–87. https://doi.org/10.1002/mrm.25901

Shemesh, N., Jespersen, S. N., Alexander, D. C., Cohen, Y., Drobnjak, I., Dyrby, T. B., … Westin, C. F. (2016). Conventions and nomenclature for double

diffusion encoding NMR and MRI. *Magnetic Resonance in Medicine*. https://doi.org/10.1002/mrm.25901

Stejskal, E. O., & Tanner, J. E. (1965). Spin diffusion measurements: Spin echoes in the presence of a time-dependent field gradient. *The Journal of Chemical Physics*. https://doi.org/10.1063/1.1695690

Szczepankiewicz, F., Lasič, S., van Westen, D., Sundgren, P. C., Englund, E., Westin, C.-F., … Nilsson, M. (2015). Quantification of microscopic diffusion anisotropy disentangles effects of orientation dispersion from microstructure: applications in healthy volunteers and in brain tumors. *NeuroImage*, *104*, 241–252. https://doi.org/10.1016/j.neuroimage.2014.09.057

T.C. Farrar (1987), *An Introduction To Pulse NMR Spectroscopy*, Farragut Press, Chicago.

Tang, C., Brown, M. A., & Semelka, R. C. (1996). MRI: Basic Principles and Applications. *Radiation Research*. https://doi.org/10.2307/3579182

Turner, R., Le Bihan, D., Maier, J., Vavrek, R., Hedges, L. K., & Pekar, J. (1990). Echo-planar imaging of intravoxel incoherent motion. *Radiology*, *177*(2), 407–414. https://doi.org/10.1148/radiology.177.2.2217777

Weast, R. C. (ed.) (1972). *Handbook of Chemistry and Physics* ,52nd ed., E-57, Chemical Rubber Publishing Co., Cleveland, Ohio.

Wheeler-Kingshott, C.A., Cercignani, M., 2009. About "axial" and "radial" diffusivities. Magn. Reson. Med. 61 (5), 1255–1260. doi: 10.1002/mrm.21965

Zeeman, P. (1897). The effect of magnetisation on the nature of light emitted by a substance. *Nature*, *55*(1424), 347. https://doi.org/10.1038/055347a0

Zhang, H., Schneider, T., Wheeler-Kingshott, C. A., & Alexander, D. C. (2012). NODDI: Practical in vivo neurite orientation dispersion and density imaging of the human brain. *NeuroImage*, *61*(4), 1000–1016. https://doi.org/10.1016/j.neuroimage.2012.03.072